Optimization of Capillary Electrophoresis With Imaging Detection for Estimation of Diffusion Coefficients

by

Atefeh Sadat Zarabadi

A thesis
presented to the University of Waterloo
in fulfillment of the
thesis requirement for the degree of
Doctor of Philosophy
in
Chemistry

Waterloo, Ontario, Canada, 2015

Author's Declaration

I hereby declare that I am the sole author of this thesis. This is a true copy of the thesis, including any required final revisions, as accepted by my examiners.

I understand that my thesis may be made electronically available to the public.

Abstract

The diffusion coefficient, D, is an important physico-chemical property of the proteins. While it can be measured using various analytical techniques, capillary electrophoresis (CE) is widely used for this purpose. CE is particularly effective in combination with whole column imaging detection (WCID) technology has enabled the CE approach to measure the diffusion coefficient in shorter time. Thus far, however, WCID has rarely been used for monitoring diffusion processes. The purpose of this study was to optimize the application of capillary electrophoresis, coupled with imaging detection, to the problem of protein diffusion coefficient measurement. This optimization addressed both experimental and data analysis aspects of the method.

For data analysis, we explored the use of Fourier transformation (FT), which offers a non-parametric, shape-independent evaluation of the raw data. FT was compared with two other common methods, both of which operate in the time domain and, unlike FT, operate in the time domain and make assumptions about the fundamental shape of the signal.

As part of exploring FT data analysis, we performed simulations, in which parameters such as resolution and measurement time were systematically varied in order to find the optimal experimental conditions. Moreover, a new experimental approach is introduced for fast and simple measurement of diffusion coefficients, and which we refer to as imaging plug flow (iPF). This technique combines capillary electrophoresis, in which proteins are pre-concentrated under the membrane by electrokinetic injection, with a dynamic imaging detection.

The concentration gradient detection method based on Schlieren optics is a universal, inexpensive, and efficient dynamic imaging technology for high-throughput moving boundary electrophoresis. A prototype multi-channel chip has been implemented for such measurements, and the effect of channel dimensions was investigated. The simultaneous measurement of the diffusion coefficients in the channels of this microfluidic device has improved the throughput of the experiment. The proposed approach addresses the limitation of single channel detection associated with UV whole column imaging detection.

The implementation of a multi-channel CE chip, coupled with Schlieren imaging detection and an improved scheme for data analysis based on FT, provides a simple, fast, and high-throughput approach to the analysis of proteins diffusion coefficients.

Acknowledgements

First, and foremost, I thank Almighty God for His love, guidance and assurance at all times during this Ph.D. program. I also give my heartfelt thanks to all those others who have helped make this accomplishment possible.

To my beloved parents and caring family, whose unconditional love and support is my foundation and has enabled me to survive the challenges of these years.

To Professor Janusz Pawliszyn for giving me the opportunity to work in his group and the chance to work on this research. You have helped me gain a better understanding of the complexity of the issues. To my committee members and examiners, especially Dr. Palmer and Dr. Krylov, for their invaluable feedback.

To my wonderful friends and room-mates for their constant support that has encouraged me to continue forward at difficult times in my research. To SPME group members, past and present, for making my time here interesting. To the people in the electronic and machine shop for always being willing to employ their expertise and time to help me. And to Mary, in the Writing Center who has patiently helped me revise my thesis and always motivated me by her positive attitude.

I especially wish to thank Dr. Hojat Yeganeh and Ms. Hamideh Zarabadi for endless hours of computer programming assistance and for tolerating all of my questions with so much patience. Thanks to Dr. Mojtaba Hajialamdari and Dr. Roman Brejna for all the efforts in troubleshooting and helping with the Schlieren set-up improvement.

The last but not the least, Maryyeh jan, Samaneh jan, and Sayeh jan, you are not only friends but mentors. I have learned a lot from you and am really thankful that you were there for me.

Dedication

I would like to dedicate my thesis to my beloved family, those who never care about my achievements more than myself. It is hard to believe that I could have survived these years far from you!

My caring parents, Maman and Baba, your unconditional love, endless support, and continuous encouragement give me the confidence to pursue my dreams. You are always an inspiration to me, and I feel really lucky to have you and all my charming siblings in my life. Especially I feel blessed to have my wonderful sister, Hamideh joon, to whom I owe a lot. It is hard to put it in words, but I am wholeheartedly thankful to you.

To my dearest grandma, Habagha joon, who is in heaven now, I wish I could look into her kind eyes and ask her to keep praying for me.

By dedication of this thesis to all of you, I would like to show my sincere love; each and every word of it stands for the moments of being away but thinking about you. I will always do my best to see the smile of satisfaction on your sweet faces.

Table of Contents

List of Tables

List of Figures

Nomenclature

ν_{ep}	Electrophoretic Velocity
D_H	Hydraulic Diameter
μ_{eo}	Electroosmotic Mobility
μ_{ep}	Electrophoretic Mobility
CCD	Charge-Coupled Device
CE	Capillary Electrophoresis
CIEF	Capillary Isoelectric Focusing
CITP	Capillary Isotachophoresis
COC	Cyclic Olefin Copolymer
COM	Commercial Cartridge
CZE	Capillary Zone Electrophoresis
D	Diffusion Coefficient
E	Electric Field
EOF	Electro-Osmotic Flow
FVB	Full Vertical Binning
GE	Gel Electrophoresis

ID Internal Diameter

MBE Moving Boundary Electrophoresis

OD Outer Diameter

PCID Partial Column Imaging Detection

pI Isoelectric Point

PLCC Pearson Linear Correlation Coefficient

RMSE Root Mean Square Error

SRM Selected Region Monitoring

TDA Taylor's Dispersion Analysis

V Voltage

WCID Whole Column Imaging Detection

Chapter 1

Introduction

One of the most powerful methods available for analyzing charged species is capillary electrophoresis, CE, which separates analytes based on their different migration speeds within an electric field. This chapter provides an overview of the technique as a general introduction to the following chapters. The principles of CE are described along with its different operational modes. Fundamentals of detection techniques are discussed, with an emphasis on determining the diffusion coefficient, D, using these technologies. Finally, the advantages of the chip-based electrophoresis are summarized.

1.1 Capillary Electrophoresis

During the mid to late 1980s, extensive research was conducted on electrophoresis inside capillary tubes, and commercial CE instruments emerged that have led to high performance separation of exceptionally small sample volumes [1]. Narrow-bore, 20–200 μm internal diameter capillaries are commonly employed to perform high efficiency separation, facilitated by the use of high voltage. The method has been successfully applied in the analysis of a wide variety of samples, which proves its capability and versatility. As an automated approach, it contributes significantly to all fields of biomedical and biotechnological research [2].

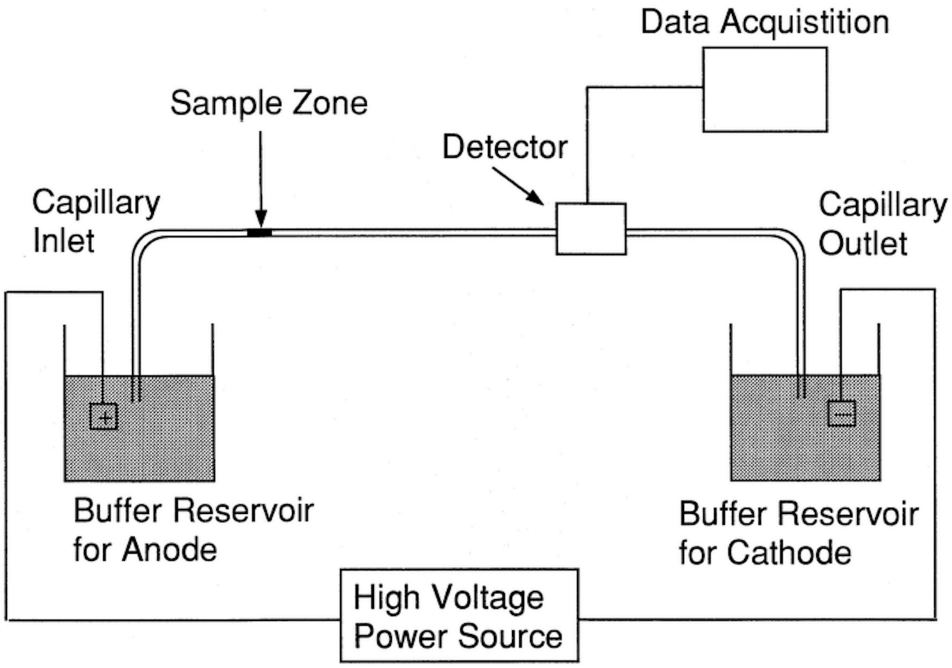

Figure 1.1: Capillary electrophoresis instrument basic configuration

1.1.1 Fundamentals

The basic instrumental configuration for CE is relatively simple, as illustrated in Figure1.1. It consists of a fused-silica capillary with a detection window at the outlet (cathodic terminal), a high voltage power supply, two electrodes, two reservoirs, a detector, and a data acquisition section. The capillary ends are immersed in the buffer reservoirs and filled with buffer solution. Then the sample is introduced by substituting the sample vial for the buffer reservoir at the inlet (anodic terminal). The analytes migrate under the influence of an electric field, and the detector records their corresponding signals upon their arrival at the detection window. The data collected by the data acquisition system are displayed as an electropherogram (e-gram), which shows detector response as a function of time.

In most common capillary electrophoresis modes, analytes separate as they migrate due to their electrophoretic mobility and are dragged toward the cathodic end by electroosmotic flow, as discussed next.

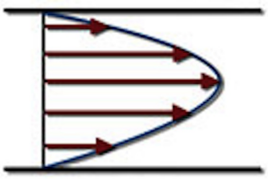

(a) Hydro-dynamic Flow Profile

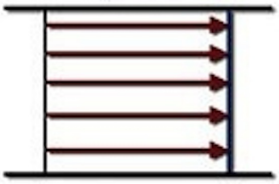

(b) Electro-osmotic Flow Profile

Figure 1.2: Flow profiles of liquid inside a capillary under hydrodynamic and electro-osmotic force, which produce plug-like vs. parabolic profiles, respectively.

Electrophoretic Mobility

The ions travel towards the opposite-charge electrode within the electric field. The velocity of the analyte, ν, in centimetres per second, primarily depends on its mass-to-charge ratio in combination with the electric field strength. The electrophoretic mobility μ_{ep} (measured in $cm^2\,V^{-1}s^{-1}$) is proportional to the ionic charge on the analyte and inversely proportional to frictional retarding factors, which are determined by the size and shape of the ions and viscosity of the medium.

$$\nu = \mu_{ep} \times E = \mu_{ep} \times \frac{V}{L} \tag{1.1}$$

An ion's migration velocity depends upon the electric field strength, E (Vcm^{-1}), which is determined by the magnitude of the applied potential (V in volts) and the length, L, over which it is applied. Thus, high applied potentials are desirable to achieve rapid ionic migration and rapid separation.

Electroosmotic Flow (EOF)

The electroosmotic flow, EOF, phenomenon happens as a result of the surface charge on the inner wall of the fused silica capillary. Glass surfaces become negatively charged due to the ionization of the exposed silanol groups, which become deprotonated above pH 3. The degree of ionization is controlled mainly by the buffer pH.

The resulting negative surface charge attracts positively charged counter-ions dispersed in the buffer solution, such that a thin diffusive layer near the channel walls is formed. When an electric field is applied, this diffusive layer moves toward the cathode, dragging the bulk of the fluid along with it. This results in the cross-sectional flow profile shown in

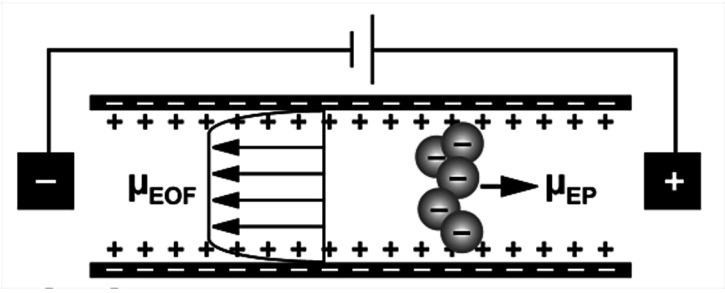

Figure 1.3: Fundamental physical processes governing CE: electrophoretic mobility and electroosmotic flow

Figure 1.3. It is plug-like and almost uniform across most of capillary cross section except very close to the wall, where the velocity slows down to zero.

EOF works as a driving force on all solutes, including neutral and negatively charged species, and pumps the bulk liquid towards the negative electrode (cathode), where the detector is located. EOF is dominant; while negatively charged species will move relative to the fluid toward the anode, this movement is slower than the bulk flow, so that they, too, will undergo a net movement toward the cathode. Thus, EOF makes the simultaneous analysis of cations, anions, and neutral species possible. On the other hand, as discussed below, electroosmotic flow must be controlled or even suppressed for certain modes of CE.

Debye-Hückel-Henry theory describes the electrophoretic mobility as follows:

$$\mu_{ep} = \frac{Q}{6\pi\eta R} \tag{1.2}$$

where Q is the net charge, R is the Stokes radius, and η is the viscosity of the medium.

Efficiency and Resolution

Capillary electrophoresis separation is typically more efficient than other separation techniques such as HPLC. In CE, there is no mass transfer between phases [1]. In addition, the flow profile in EOF-driven systems is uniform and does not significantly contribute to band broadening as it does in pressure-driven chromatography. Separation by capillary electrophoresis can have several hundred thousand theoretical plates. The efficiency of a system can be derived from fundamental principles. The migration time, t, is determined as follows:

$$t = \frac{L}{\nu_{ep}} = \frac{L^2}{\mu_{ep} V} \tag{1.3}$$

During migration through the capillary, molecular diffusion along with other dispersion phenomena lead to peak dispersion, σ^2, calculated as

$$\sigma^2 = 2Dt = \frac{2DL^2}{\mu_{ep} V} \tag{1.4}$$

where D is the solute's diffusion coefficient in $\frac{cm^2}{s}$. The number of theoretical plates is given by

$$N = \frac{L^2}{\sigma^2} \tag{1.5}$$

Substituting the dispersion equation into the plate count equation yields

$$N = \frac{\mu V}{2D} \tag{1.6}$$

where N is the number of theoretical plates, μ is the apparent mobility in the separation medium, and D is the diffusion coefficient of the analyte. According to this equation, the efficiency of separation is only limited by diffusion and is proportional to the strength of the electric field. The practical voltage limit with today's technology is about 30 kV.

The resolution improves with increasing field strength, as long as the Joule heating remains insignificant. Narrow-bore capillaries facilitate heat dissipation, which makes the use of higher field strengths possible, but decreases the detection sensitivity due to shorter transverse path length. It also makes the sample/buffer introduction more difficult. The resolution (Rs) of capillary electrophoresis separation can be written as [3]:

$$Rs = \frac{1}{4}\left(\frac{\triangle \mu_{ep}\sqrt{N}}{\mu_{ep} + \mu_{EOF}}\right) \tag{1.7}$$

As shown by equation 1.7, resolution increases with the difference in electrophoretic mobility between the two analytes. Moreover, when the analytes' electrophoretic and electroosmotic mobilities are of similar magnitude and opposite sign, this will also contribute to high resolution. In addition, lower velocity separation gives higher resolution [1].

Resolution decreases due to band broadening effects such as diffusion, Joule heating consequences, the finite widths of the injection plug and detection window, interactions

between the analyte and the capillary wall, instrumental errors such as siphoning, depletion of buffering capacity in the reservoirs, and so on. It is important to identify and minimize the effects that cause broadening in order to achieve minimal, diffusion-controlled dispersion.

1.1.2 Principal Modes of Capillary Electrophoresis

Capillary electrophoresis can be divided into four major categories; moving boundary, isotachophoresis, zone electrophoresis, and isoelectric focusing. Each mode is briefly introduced here, and separation of two substances by any of these four modes is illustrated in Figure 1.4. All modes except isotachophoresis were employed in the course of this study.

Moving Boundary Electrophoresis

Tiselius, who won the Nobel prize in chemistry for his research on electrophoresis, originally described moving boundary electrophoresis (MBE), in which a long band of sample is placed between buffer solutions in a tube [5].

Under the influence of an electric field, sample components migrate toward the anode or cathode depending on their charges, at a rate determined by each component's electrophoretic mobility. In this mode, component separation is never accomplished inside the sample zone. However, due to different velocities, the components become partially purified at either end, while the rest of the components remain overlapped. This mode lacks the required resolution for the separation; hence, it is generally employed for measurement of electrophoretic mobilities only. This technique is commonly combined with Schlieren detection, which is based on the change in refractive index that occurs at the boundaries between separated compounds.

Isotachophoresis

Isotachophoresis (ITP) was the most widely used instrumental capillary electrophoretic technique prior to 1981. By today's standards, the capillaries used in this application were rather wide (250–500 μm) [4]. The unique feature of this mode is the heterogeneous buffer system: the leading and the terminating electrolytes have a higher and lower mobility, respectively, than any of the sample components. The sample is sandwiched between these two buffers, where the separation occurs based on the individual mobilities of the analytes. As shown in Figure 1.4, individual components form stable zone boundaries [6].

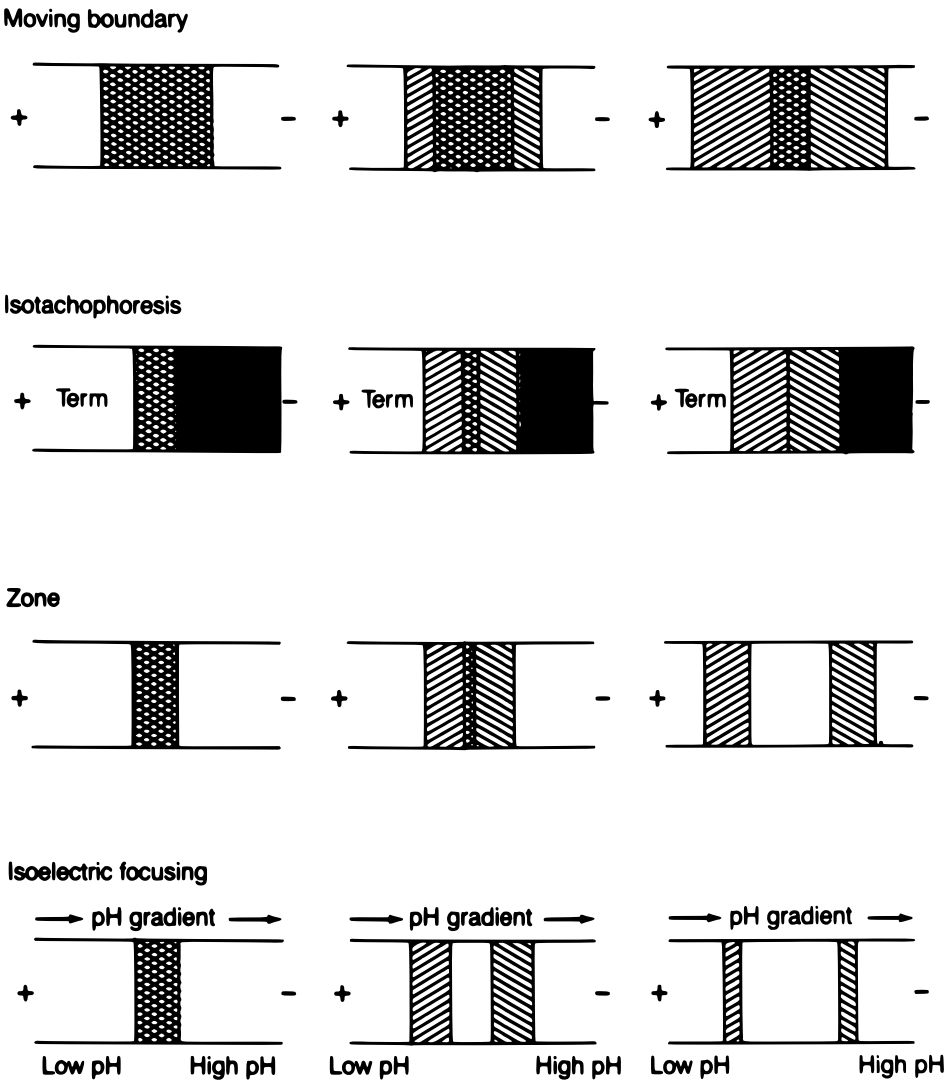

Figure 1.4: Four principal modes of electrophoresis. The cross-hatched bands represent the analytes. The black areas represent the leading buffer (Ref. [4], Copyright (1981) American Chemical Society).

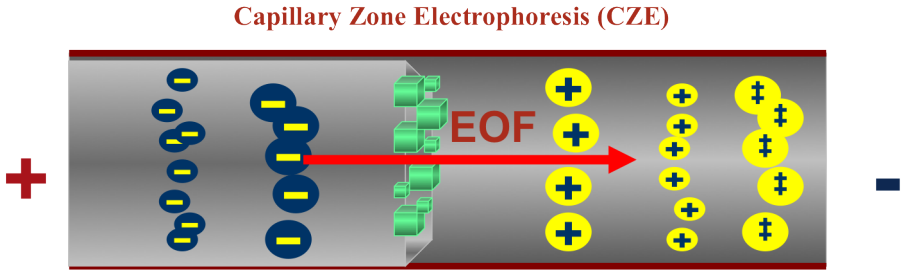

Figure 1.5: Elution order in CZE; Cations elute in order of their charge-to-size ratios, with small, highly charged cations eluting first. Neutral molecules, which move through the capillary under the influence of only the electroosmotic flow and are not separated from each other, elute after the cations. Anions elute in reverse order to their charge-to-size ratios, with small, highly charged anions eluting last (Ref. [8]).

As the name indicates, the velocity of each band is identical. Bands that contain highly mobile species have high conductivity, which means that a lower voltage drop occurs across such a band. Since the mobility is the product of the conductivity and the voltage drop, and the conductivity and voltage drop are inversely proportional, the individual band velocities are self-normalizing. Similarly, isoelectric focusing is also a consequence of velocity normalization. For example, if a given molecule diffuses away from the zone of its isoelectric point into a neighbouring zone, it will either speed up or slow down based on the field strength encountered and thus be driven back in the direction of its isoelectric point.

In applying the ITP technique inside capillary, the electroosmotic flow should be suppressed. In the case of uncharged tubes, e.g. Teflon, there is no need for any special measures. With glass capillaries, the inner surface can be coated with suitable additives such as methyl-cellulose to effectively suppress the EOF.

Capillary Zone Electrophoresis

Capillary zone electrophoresis (CZE), also known as free solution capillary electrophoresis, is the simplest form of CE. In 1981, Jorgenson ran CZE in a arrow bore capillary in contrary to tubes used previously [7] for the first time.

Zone electrophoresis has a mechanism similar to moving boundary mode, except that here a narrow sample band is introduced, using either electrokinetic or hydrodynamic injection techniques, and the components become fully separated into discrete zones, as in

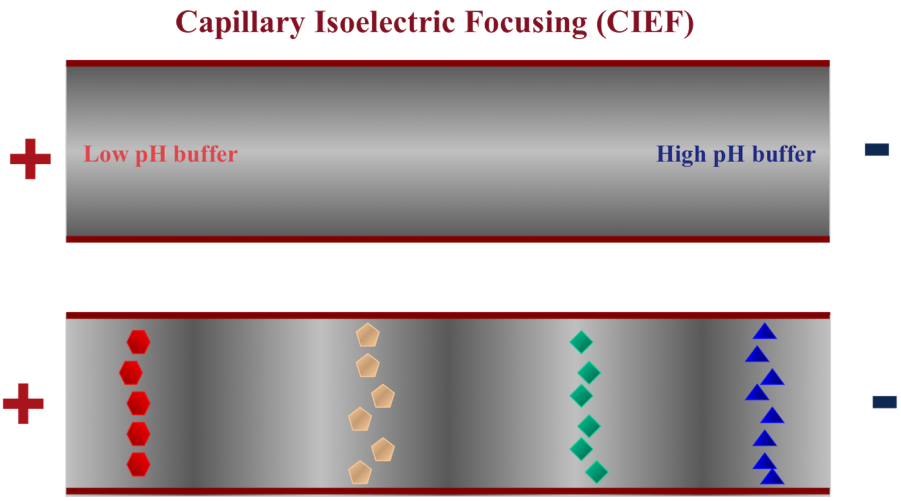

Figure 1.6: Capillary isoelectric focusing mode performs based on pH gradient (Ref. [8]).

Figure 1.4, as they migrate along the capillary. In a homogeneous buffer system and under a constant electric field, the analytes separate based on their charge-to-mass ratio differences. Zone electrophoresis in long separation capillaries is very useful for the separation of proteins and peptides. However, CZE in microfluidic chip format is arguably not efficient due to miniaturized channels, which are not appropriate for high-resolution separation.

Isoelectric Focusing

Capillary isoelectric focusing (CIEF) is a CE separation technique for proteins and peptides based on differences in their isoelectric points (pIs) and is characterized by high resolution and spontaneous stationary focusing of analytes [9].

The principle of isoelectric focusing (IEF) is that molecules migrate in pH gradient established in an electric field until they become neutral (Figure 1.6). Through a pH gradient established by carrier ampholytes in the electric field, amphoteric molecules such as proteins are separated on the basis of their individual isoelectric points. The carrier ampholytes are made up of a series of zwitterionic compounds. Within the electric field, positively charged ampholytes migrate towards the cathode, and those bearing a negative charge migrate towards the anode. When the solute encounters a pH where its net charge becomes zero, the isoelectric point (pI), migration stops. While most applications include them, CIEF without carrier ampholytes has been also been reported [10].

Resolving power. CIEF is generally used for high resolution separation of proteins and polypeptides, as well as for determining the isoelectric points of individual proteins. This requires a smooth pH gradient, which can be obtained by increasing the number of ampholytes in solution. The resolving power, ΔpI, of IEF is described by the equation

$$\Delta pI = 3\sqrt{\frac{D(dpH/dx)}{E(d\mu/dpH)}} \tag{1.8}$$

where D is the diffusion coefficient, E is the electric field strength, and μ is the electrophoretic mobility of the protein. Any convective forces and EOF must be suppressed if CIEF experiments are to be effective. The dynamic coating of the capillary walls suppresses the EOF as well as the protein adsorption.

CIEF has been employed for a wide variety of compounds of pharmaceutical interest such as antibodies, peptides and proteins [11]. It has been developed in many aspects i.e. detection techniques, multidimensional systems, miniaturization and other applications [12].

1.2 Detection Techniques

Different types of detection methods such as those based on the absorption of UV radiation, fluorescence, conductivity, amperometry, and mass spectrometry are available for CE. UV absorption and florescence are widely used in CE detectors. They are commonly applied "on-column" by removing a small portion of the capillary's protective coating and making a transparent window in the capillary tubing. Most proteins have tryptophan and tyrosine residues that absorb UV_{280} radiation and also emit fluorescence. In other cases, fluorescence detection can be applied in conjunction with fluorescent tagging of the analytes. Where possible, fluorescence provides greater sensitivity, especially when a laser source is used for excitation.

1.2.1 Concentration Gradient vs. Average Detection

The analytical signals can be proportional to the average of the analyte concentration that reflects the true concentration value (C), for example in absorbance detection. The signal amplitude can also depend on the non-uniform distribution of analytes in the detection volume as in gradient-based detectors, which results in the derivative form of concentration

($\frac{dC}{dx}$). The latter type of method ignores the drifts associated with the slow variations in the concentration by emphasizing the changes in the concentration.

Schlieren imaging detection is a powerful technique used to visualize non-uniformities in the refractive index of transparent media. It was established in the early 1800s to visualize fluctuations in optical density [13]. A universal detection method for all compounds consists in concentration gradient detection. Table 1.1 provides a list of capillary electrophoresis studies where a concentration gradient detector based on Schlieren optics was employed for detection, along with some important characteristics of the methods.

CE mode	Characteristic of the method	Ref.
CIEF	isoelectric point differences, focusing effects	[14–16]
CITP	self-concentration and focusing effects	[17, 18]
MBE	boundaries instead of sample zones, no full separation	[19, 20]
CZE	differences in their mobilities, dilution effect	[21]

Table 1.1: Studies on capillary electrophoresis modes coupled with Schlieren detection

Some references to selected papers that introduce Schlieren detection for different CE modes are listed in Table 1.1. However, there are many additional studies that report applications of this technique for analytical applications [22]. The concentration gradient detection based on Schlieren optics is discussed in detail in Chapter 4.

A previously described multi-purpose capillary electrophoresis system [21] demonstrates that all four separation modes can be coupled with concentration gradient detection using Schlieren as a universal detector. This detection method was found to be particularly sensitive with those CE modes that show self-concentration and focusing effects. The concentration gradient detection method based on Schlieren optics offers advantages such as sensitivity and enhanced resolution in addition to drift reduction [23]. Two imaging detection techniques were employed in this research; UV absorbance whole column imaging detection and concentration gradient Schlieren imaging microscope, as a selective and a universal detection method, respectively.

1.2.2 Single Point vs. Partial/Whole Column Imaging Detection

In commercial CE instruments, external coating of the capillary is removed at a fixed point at the cathodic end, which creates a transparent detection window for the attachment of

an on-line single point imaging system (Figure 1.1). Thus, all separated analyte zones have to move past this detection point. CIEF experiment with single point detection is therefore conducted as a two-step procedure that includes separation and mobilization. After separation has occurred, the sample zones are mobilized to pass through the column to the detection point by chemical, hydraulic and electro-osmotic mobilization techniques [24]. This mobilization process imposes some limitations such as longer analysis time, extra peak broadening and sample adsorption that reduce the resolution. In order to address these drawbacks, a new method, called whole column imaging detection (WCID), has been developed in our research group. This method uses a charge-coupled photodiode array for a universal concentration gradient imaging system [25, 26].

In addition to WCID, partial column imaging detection (PCID), which uses only partial illumination of the column, has also been widely used in CE experiments [27]. The dynamics conveniently obtained by PCID are more useful than those of conventional single-point detection; however, this partial approach is not capable of monitoring the separation dynamics in the whole column. Various analytical applications of the WCID in CE have shown that the CE-separation process can be directly observed, and that the analysis is greatly accelerated with this method. In conventional single-point detection and PCID, the separation columns used are up to one meter long; however, in WCID, a shorter capillary is employed (5 cm in a commercial CIEF-WCID cartridge).

The dynamic monitoring of phospholipid-protein [29], protein-DNA [30], and protein-drug [31,32] interactions is facilitated by capturing images at different times. The total time for optimization of the experimental conditions such as focusing time is greatly reduced using the real time monitoring by WCID.

As a unique separation technique and a powerful tool for the study of reactions of proteins [33], the CIEF-WCID is drawing growing interest in separation science [34, 35]. The use of WCID is not limited to CIEF, however, and its application for effective analysis is possible in different modes of CE such as capillary-zone electrophoresis in agarose gels [36].

1.2.3 High-throughput Analysis Imaging Detection

Electrophoresis can be performed in either slab gel or capillary format. Slab gel electrophoresis (GE) has the advantage of high-throughput analysis in which the samples are loaded at several wells and separation performed and detected simultaneously. Increasing the throughput of analysis in capillary electrophoresis has been attempted using different methods, such as an absorption-detection approach for multiplexed capillary electrophoresis via a linear photo-diode array [37] and concentration gradient detection using a CCD

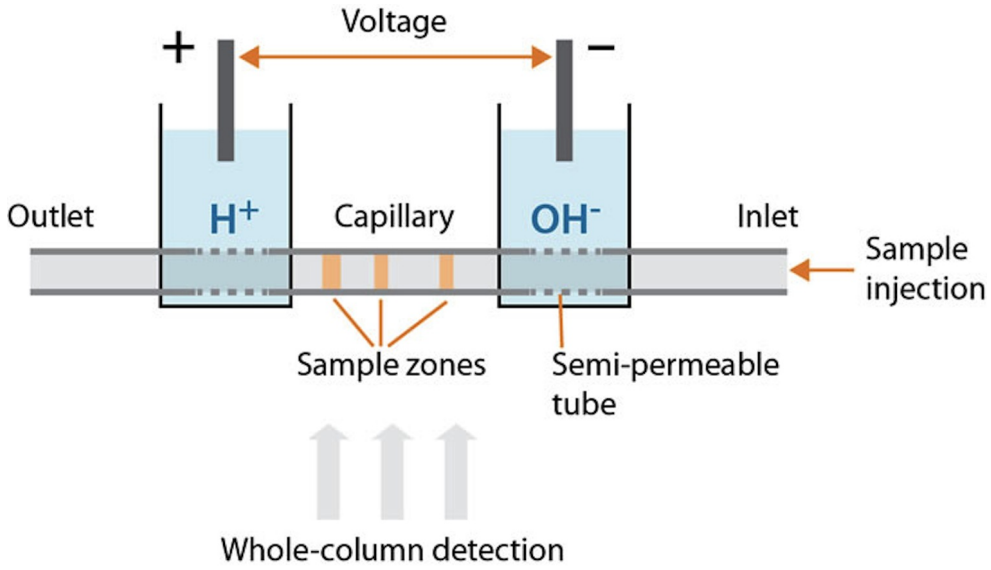

Figure 1.7: Schematic of whole column imaging detection for capillary isoelectric focusing (Ref [28]).

camera with multiple-capillary array [38, 39]. The multi-capillary imaging detection of protein samples was applied to isoelectric focusing in a capillary array using an absorption imaging detector [40]. There are 8-, 96-, and 384-capillary instruments used in DNA sequencing, utilizing single-point detection [41].

In addition to the capillary array configuration, multiple capillaries can be put together in a bundle form. The idea of a capillary bundle was inspired by photonic crystal fibres (PCFs) and successfully incorporated into commercial capillary electrophoresis equipment in conjunction with fluorescence detection [42]. These micro-structured fibres were also used in with other analytical techniques such as LC-MS as an electro-spray emitter that enhanced operational throughput and improved robustness, due to increased sample throughput, low back-pressure, large flow rate range, and good sensitivity [43].

Increasing measurement throughput was also of interest in chip-based electrophoresis. Developments in the lab-on-a-chip technology are making multi-channel microfluidic devices more common and popular. Integration of different elements on a chip makes it a comfortable choice compared to capillary based cartridges. For example, a six-channel microfluidic device with a scanning fluorescence detection system was proposed for affinity capillary electrophoresis analysis for immunoassay [44].

The simultaneous detection of multiple capillaries or channels can be performed in any

type of single-point, partial column, or whole column detection.

1.3 Determination of Diffusion Coefficients

The accurate measurement of a protein's diffusion coefficient is significant from different viewpoints; it determines an important physicochemical property that is vital in dynamic processes like chemical and biochemical reactions. Thus, protein diffusion coefficients have been extensively studied theoretically and experimentally, providing fundamental information and various practical applications such as determination of the molecular weight [45], and stability investigations in pharmaceutical and clinical fields [46]. This long-standing interest has led to progressive improvement of methods. It has been investigated both theoretically and experimentally. In the present study, modifications to both instrumental and analytical approaches are taken into consideration.

During any experimental measurement, it is important to compare the experimental results obtained with a known standard to those that have been reported in the literature, for confirmation of the method's accuracy. In the case of diffusion coefficients, however, doing so is more complicated, because different tables listing the same compound often report different values, depending on the way the measurement was made.

1.3.1 Taylor-Aris Analysis

Taylor was the pioneer in the dispersing approaches wherein a solute "plug" flows through an open tube, and $D$is calculated as a function of the solute diffusivity [47–50]. These studies laid the foundation for developing Taylor's dispersion analysis (TDA) into a robust method for rapid and accurate measurement of diffusion coefficients.

In the method proposed by Taylor, the concentration profile of solute pulses and fronts was monitored as they flowed through a uniform, cylindrical tube under laminar (Poiseuille) flow to measure the diffusion coefficient. The solutes undergo radial diffusion due to concentration gradient between the center of the capillary and the walls, which results from the fluid parabolic velocity profile (Figure 1.2). The observed overall dispersion is a combination of axial convection and radial diffusion effects. In the initial studies, solute diffusivity was determined by measuring dispersion, while neglecting the axial diffusion. Aris addressed this shortcoming by extending Taylor's analysis.

1.3.2 Current Analytical Methods

There are various experimental techniques available for measuring diffusion coefficients, each of which has its inherent strengths and weaknesses. The techniques include sedimentation [51], dynamic light scattering (DLS) [52], and pulsed NMR techniques [53], in addition to polyacrylamide gradient gel electrophoresis [54], electrophoretic light scattering (ELS) [55], and chromatographic broadening done on the basis of laminar flow analysis.

Optical methods such as classical refractive index detection and the more sensitive fluorescence detection remain useful tools. However, the refractive index of a sample is affected by all solutes contained in it, and this non-selective universal response can limit the usefulness of the measurement. Fluorescence allows for more specific detection, but it requires either intrinsic fluorophores, or else the fluorescent tagging of the analyte molecules; the fluorescent labeling may alter the diffusion behaviour relative to that of the original untagged molecule of interest.

Electrochemical methods are often applied successfully, but their application is limited to electro-active analytes. In the NMR approach, the diffusional relaxation of stimulated nuclei is measured, with mechanical and magnetic stability requirements that are rarely met consistently; it also involves complicated and expensive instrumentation. On the other hand, chromatographic analysis is capable of measuring the diffusion coefficient for a wide variety of analytes, particularly with a general detection system such as a UV detector. Several standard chromatographic techniques have been employed to measure diffusion coefficients, including gas chromatography [56], micellar electrokinetic chromatography [57], anion exchange chromatography, and supercritical fluid chromatography [58].

As discussed, there are different methods for measuring diffusion coefficients, and the coefficients determined for one and the same compound may vary significantly between these methods. The Wilke-Chang equation [59] develops a correlation of diffusion coefficients in dilute solutions to estimate the solute's D, considering the solvent association parameter. This estimate can be helpful when there is no report of the diffusion coefficient in the literature for a certain compound. However, this provides only a general estimate that may not be valid for a specific combination of compound and conditions a researcher may choose to investigate.

1.3.3 Capillary Electrophoresis Method

In GC and LC, diffusion plays a role in many band-spreading processes, which are described by complicated equations due to involvement of more than one phase [1]. However,

in capillary electrophoresis, the situation is much simpler, and the observed peak variance, σ^2, can be defined as the sum of the variances of several zone-broadening effects (Equation 1.10). The broadening due to longitudinal diffusion, σ^2_{dif}, is related to the diffusion coefficient, D, by the Einstein equation;

$$\sigma^2 = 2Dt \tag{1.9}$$

where t is the migration time of the solute. Contribution of other broadening effects are accounted for by adding the variances from the finite lengths of the injection plug and the detector cell (σ^2_{inj} and σ^2_{det}), electro-migration dispersion (σ^2_{emg}), Joule heating (σ^2_{temp}), and interactions of the solute with the capillary wall (σ^2_{wi}):

$$\sigma^2 = \sigma^2_{dif} + \sigma^2_{inj} + \sigma^2_{det} + \sigma^2_{emg} + \sigma^2_{temp} + \sigma^2_{wi} \Rightarrow \sigma^2 = 2Dt + \sigma^2_{inj} + \sigma^2_{det} \tag{1.10}$$

In ideal conditions, Joule heating is negligible, and σ^2_{emg} is minimized by a suitable choice of buffer concentration. Wall interactions can be eliminated by proper coating of the capillary inner surface. Minimizing the broadening effects arising from these three sources, the diffusion coefficient can be estimated by knowing L_{inj}, the length of the injection plug [60], and L_{det}, the length of the optical window on the capillary; from these, σ^2_{inj} and σ^2_{det} can be calculated according to Sternberg [61]. Thus, using calculated values for injection and detection variances, D can be evaluated from the measurement of a single band width and the corresponding migration time [62]. In the following section, the capillary electrophoresis approaches for determination of diffusion coefficient are discussed in depth.

1.4 Determination of Diffusion Coefficient with CE Technique

Measurements of diffusion coefficient by CE can either be conducted while the species are moving under the influence of an electric field, which is referred to as dynamic mode, or it can be performed when the voltage is off, that is, in static mode [63]. The only significant source of band broadening under ideal conditions is longitudinal (molecular) diffusion; however, these ideal conditions are not often met in the dynamic mode. Other factors that contribute to broadening, including initial analyte injection width, analyte-wall interactions, Joule heating and electro-migration dispersion, would be removed or

minimized in static mode in the absence of an electric field. The peak variance due to wall interaction σ_{wi}^2 can be neglected based on the assumption that the equilibration time for any adsorption-desorption process is much smaller than the measurement time.

1.4.1 Dynamic Mode

As mentioned above, dynamic measurements are performed when the analyte is moving under the influence of an electric field. Three dynamic methods that have been reported for measuring diffusion coefficients by capillary electrophoresis include the "stopped-flow", "on-the-fly", and "E-field" approaches [64,65]. The measurements can be performed either in a single run where all the analyte band dispersion is assumed to be from diffusion, or multiple runs under different conditions. Recording the concentration profile of the same sample plug before and after the dispersion will result in precise measurements of D. The primary methods did not fulfil this fundamental requirement, and they measured the concentration profile in separate experiments. However further developments suggest single experiment design for dynamic methods.

Stopped-flow method

This method usually requires two separate experiments. The first run is made under ordinary conditions, that is, the sample run straight through under constant voltage. During the second run, the electric field is removed for a defined period of halt time, $t_{(halt)}$, when the solute zone is midway through the capillary. The voltage is than reapplied in order to electro-migrate the sample toward the detector [64, 65]. The diffusion coefficient is evaluated from the difference in the spatial peak variances between both runs:

$$D = \frac{\sigma_2^2 - \sigma_1^2}{2t_{(halt)}} \tag{1.11}$$

where σ_1^2 and σ_2^2 refer to the variances without and with the voltage halt, respectively. The stopped-flow times are then used to calculate the diffusion coefficient using Einsteins equation (Eq. 1.9).

The stopped-migration approach has been also reported in a single run fashion [66]. This was achieved by double passage through a single point detector by reversing polarity with a no-flow period between them (Figure 1.8). Hence, in the same experiment, the concentration profile of the compound was measured twice: before dispersion and after dispersion.

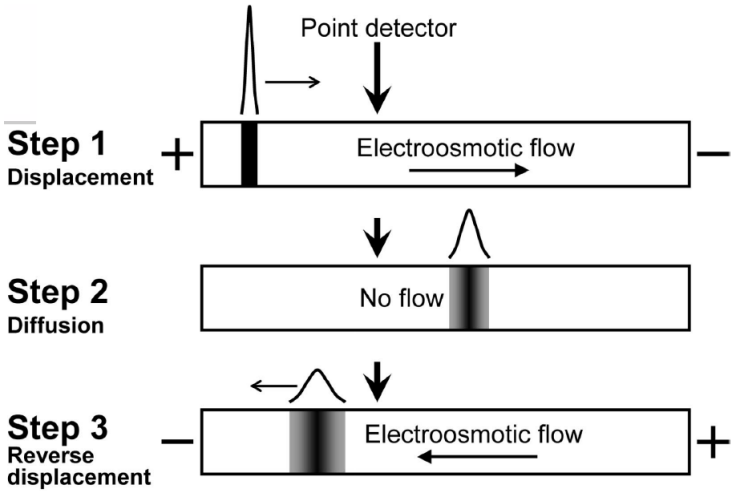

Figure 1.8: Precise determination of diffusion coefficient in a capillary, through three major steps; (1) moving a short plug of the sample by EOF to obtain the initial concentration profile (2) the electeric field is lifted to allow the protein diffusion under no-flow conditions (3) reversed EOF pulls the diffused sample plug toward the detector to record the final concentration profile [66].

The proposed approach by Krylov et al. [66] involves data processing, which addresses the disadvantages of earlier time-domain methods with the peak shape assumption issue. The initial concentration profile is used as a function that will be widening with diffusion as a function of time. Two functions, associated with the profiles before and after dispersion, are linked through a coefficient of diffusion. Mathematically, this idea is easier implemented in the case of whole-column imaging than in the case of a single-point detector. Because in the single point detection, one need to move the sample through the detector to record the profiles as a function of time, and then convert them into space domain using the velocity. WCID obviously do not need to do this conversion, in addition to the fact that more time points can be collected via a WCID system using static mode and all of them can be used in the calculations to easily assess experimental error of D.

On-the-fly or length method

In the on-the-fly approach, as the its name suggests, the measurements is performed when the sample plug is moving under the influence of an electric field. A single run is conducted and all the dispersion in the analyte band is assumed to be from diffusion [64, 65]. In this method, the peak width is measured as the temporal peak variance, which is converted

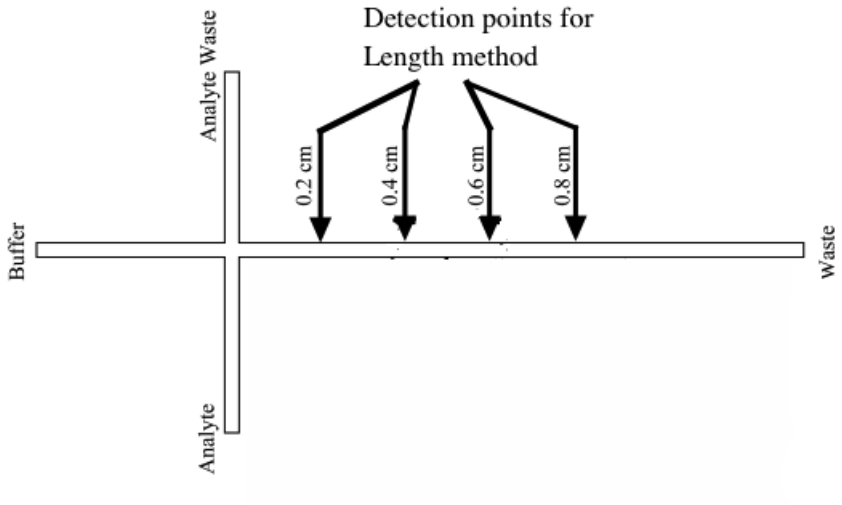

Figure 1.9: Schematic of microchip used for diffusion coefficient measurements via length method [63].

to a spatial peak variance (σ^2). Using this parameter and the run time (t), the diffusion coefficient is calculated using the Einstein equation (Eq. 1.9). In case of large peak variance due to the injection, the σ^2_{inj} can be calculated and subtracted from the total peak variance.

In systems with a single point detector, diffusion coefficient can be measured with length method that has a similar approach to the on-the-fly technique. In the length method, several consecutive runs were made with specific detection lengths [63]. An example of this approach with different detection points on a microchip is shown in the schematic (Figure 1.9). The peak variances at each point was plotted against their associated peak migration time and the diffusion coefficient was extracted from the slope of the curve.

E-field method

In this method, the field strength is varied, and associated peak variances are measured; however, for minimizing the Joule heating effect, the maximal field strength employed electric field strengths is kept low [65]. With all of the above dynamic methods, peak variance is assumed to arise exclusively from longitudinal diffusion. While this may not always be strictly true, the effect of other causes of broadening can be minimized by imaging in static mode (see below).

1.4.2 Static Mode

In static mode, the PCID or WCID detection modes are needed, and single point detection cannot be used. Uniform illumination and inclusion of a large enough section of capillary in the image are required for performing the static measurement. Channels on micro-fabricated devices are more favourable for this application due to shorter injection plug length, and smaller imaged area on the chip. In addition, simpler imaging optics are involved because of the planar surfaces on the chip compared to the capillary. A static method for diffusion coefficient measurement in a capillary by capillary zone electrophoresis and capillary isoelectric focusing has been developed previously [45, 67]. In the current study, both static and dynamic measurement of the diffusion coefficient are applied to a multi-channel chip format.

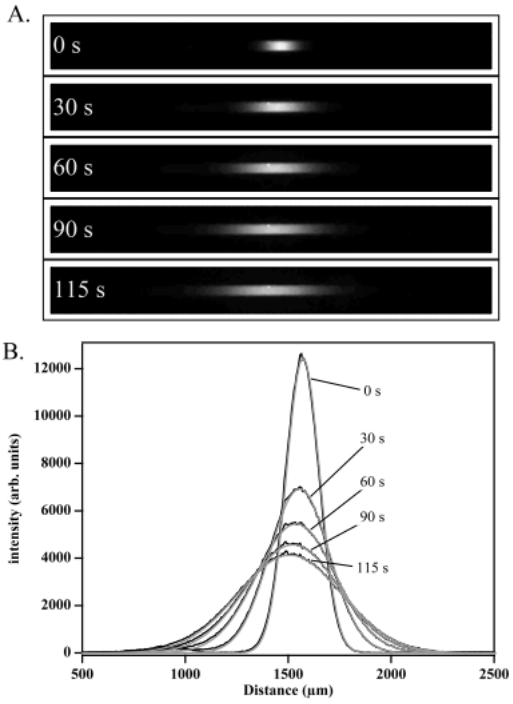

Figure 1.10: Fluorescence images of R6G diffusing over time in a microchip obtained for use with the static imaging method. (B) Profiles obtained from part A by summing across the width of the channel. Each profile was fitted by a Gaussian equation (gray dotted lines) to extract the peak variance [63].

1.5 Microfluidic Devices

Capillary electrophoresis has many advantages over gel electrophoresis, but a disadvantage is its limited sample throughput. Moreover, the use of capillaries with round cross section produces lens effects during detection. These drawbacks have inspired researchers to develop microfluidic chips as an alternative device. Lab-on-a-chip is a promising branch of technology, offering numerous advantages such as easy integration of different elements, and chaining of different separation methods [68, 69]. Due to the small fluid volume of the channels or narrow bore capillaries, small amounts are consumed, which is especially significant for expensive analytes.

CE has been successfully performed in chip format in a number of studies [70]. Most of these studies rely on single point detection; however, whole column imaging detection is also feasible with a short capillary [71]. Miniaturized CIEF-WCID has been conducted in a 1.2 cm capillary as a separation column for protein analysis, which showed good resolution. The whole-column imaging set-up was miniaturized by the use of a light-emitting diode (LED) as the light source [72]. Other promising combinations of detection techniques have been also reported for electrophoresis in capillaries and channels on chips [73].

The material of the chip is also a crucial parameter in the CE application. Plastic microfluidic devices [74] and other polymeric slides have been reported for this purpose [75]. Various materials that were employed in microchip electrophoresis need specific surface modification [76]. Chemical modification of the polymeric microchip devices is very common as well. Various strategies for wall coating for capillary electrophoresis on microchips that control the electroosmotic flow and wall interactions have been suggested in the literature [77, 78]. Different applications of electrophoresis in protein analysis are reviewed in reference [79]. Some outstanding examples of the chip-based electrophoresis include integration of CE steps and components such as pre-concentration, automated derivatization, immobilization of proteases and other proteins in micro-reactors, and so on.

The ability to measure diffusion coefficient fast is controlled by the value of diffusion coefficient with respect to ability to detect minor changes in signal. This has been used for the molecular size determination on-chip using dual-beam refractive index gradient detection in a micro-fluidic analyzer [80]. The growing interest in high-throughput screening in the pharmaceutical industry influences method development in the analytical sciences [68]. An example is micro-chip capillary zone electrophoresis (CZE), which was developed as a method for high-throughput analysis of charge heterogeneity in antibodies. This high-speed microchip electrophoresis separation was utilized for high-throughput charge profiling of antibodies during process and formulation development [81].

The use of microfluidic devices has a number of significant advantages for biomedical research and clinical technologies. The microfluidic devices are fabricated with relatively inexpensive techniques and amenable to mass production. Microfluidic technologies enable the fabrication of highly integrated devices for performing several different functions on the same substrate chip. One of the long term goals of lab-on-a-chip field is to eliminate time consuming laboratory analysis procedures by introducing integrated, portable devices.

1.6 Research Objectives and Overview

The objective of the current study is to improve the estimation of the diffusion coefficients of proteins. It was accomplished through taking advantage of whole column imaging detection combined with data processing in the frequency domain, and developing a multi-channel chip for high-throughput capillary electrophoresis. This interdisciplinary approach, which involves both instrumentation and data processing aspects, provided a fast, accurate and more generically applicable method to make accurate diffusion coefficient measurements. The thesis consists of five chapters, which are categorized into two major sections, namely, capillary electrophoresis hardware and software development.

The first section incorporates chapters 2 and 3, which develop the FT approach data processing programs, including the simulation and optimization of the experimental parameters. First, various peak shapes are simulated in order to further corroborate that this technique works well regardless of peak shape. Next, optimization of the method and investigation of its robustness in the presence of noise are discussed. Lastly, the proposed FT approach is validated by analyzing and comparing whole-column imaging detection CIEF and iPF results in the determination of diffusion coefficients.

The second section presents the improvements gained in the throughput of the method by introducing a multi-channel chip coupled with concentration gradient detection on the basis of Schlieren optics. In chapter 4, the proposed approach is validated through data analysis of experimental diffusion patterns of proteins. This chapter also describes experiments on the static and dynamic modes of diffusion coefficient measurement.

The analytical approaches are explored for determination of D from experimental and data treatment points of view. Chapter 5 presents concluding remarks and proposes potential modifications, as well as future directions for the capillary electrophoresis technique with respect to determination of diffusion coefficients.

Chapter 2

Diffusion Process Simulation; Employing Fourier Analysis to Measure Diffusion Coefficients

2.1 Introduction

Time-dependent signals can be analyzed directly, that is, in the time domain, or after transformation into a frequency spectrum using Fourier transformation (FT). Time-domain analysis is conceptually simpler, but it requires assumptions about peak shapes that may not be applicable. This constraint is removed by carrying the signal to the frequency domain. The FT approach reduces the effect of non-ideal characteristic signal shapes on the estimation of D, a typical error associated with analysis conducted in the time domain. The assumption of Gaussian peak shape for the diffusing signals restricts the calculations, while Fourier analysis offers a non-parametric measurement of diffusion coefficients, which is not dependent on peak shape.

In the literature, the Fourier transform technique has been widely used in the evaluation of overlapping signals, mostly for noise filtering of chromatograms and for deconvolution by peak sharpening [82]. It has been also applied successfully in the determination of diffusion coefficients with fluorescence recovery after photo-bleaching [83], light-scattering [84],

The results presented in this chapter have been published in: "Accurate Determination of the Diffusion Coefficient of Proteins by Fourier Analysis with Whole Column Imaging Detection" by Zarabadi, A. S.; Pawliszyn, J. Anal. Chem. 2015, 87, 21002106.

and chip-based electrophoresis [85]. The frequency domain analysis was especially adopted for biological signal processing applications. In fact, many clinical and physiological phenomena are quantified through analysis in the frequency domain as a well standardized tool. Bianchi et al. discussed different time-frequency approaches including the wavelet transform, and evaluated their performance with respect to signal characteristic improvement [86].

In the present study, three different mathematical functions have been employed to simulate the diffusion process. The simulation is also utilized to characterize the spatial and temporal parameters that affect the overall performance of the system [87].

This chapter provides an overview of the Fourier transformation approach in comparison with time domain analysis for the determination of diffusion coefficients. First, definitions of the mathematical approaches in both domains are provided. Next, various peak shapes are simulated in order to further explore the shape-independent feature of this technique. Lastly, optimization of the method and investigation of method robustness in the presence of noise are discussed.

2.2 Mathematical Model

In order to extract the diffusion coefficient, the spatial decay of signals can be either studied in the time/space domain or carried to the frequency domain. The principles of both conventional time domain calculations and of Fourier analysis are summarized in this section.

Diffusion is a time-dependent process, and it appears natural to analyze it as a function of time, that is, in the time domain. Most of the common approaches to time domain calculations are based on the Gaussian shape assumption. Peak width at half maximum (FWHM) or $W_{1/2}$ is an effective simple method that is used in conjunction with Gaussian shape signals. Curve fitting is another common method in the time domain. While it is not necessarily limited to the use of the Gaussian distribution, it nevertheless makes assumptions about the shapes of the peaks being fitted. However there are also reports [66] on measuring the diffusion coefficient without peak shape assumption. The FT method is a more general, shape-independent approach; it extracts the diffusion coefficient after carrying the temporal data into the frequency domain.

2.2.1 Time Domain Calculations

Time-domain approach has been primarily employed for determination of the diffusion coefficient from the originally time-based electrophoresis data. The dispersion of a sample plug is simulated for a single run, and the variances are calculated at different time intervals contentiously. While advanced software and electronic integrators are available to measure variances (σ^2), the full width at half maximum is a common approach to approximate the variance. This approach assumes that the peak shape is Gaussian. The curve-fitting method is a more general technique, and is suitable for both Gaussian and more-complicated models. According to the Einstein equation, the diffusion coefficient is related to the signal variance at its corresponding time:

$$\sigma^2 = 2Dt \tag{2.1}$$

The concentration profile is fitted to a Gaussian function and the variance is approximated from $W_{1/2}$. To extract the diffusion coefficient, the variance is plotted against the time. Dividing the slope of the curve by two produces the diffusion coefficient.

Full Width At Half Maximum

The full width at the half-maximum is a useful approximation for systems that do not electronically integrate peaks from a baseline. This parameter for a Gaussian function is denoted by $W_{1/2}$, and is approximated by:

$$W_{1/2} = 2\sqrt{2\ln 2}\,\sigma \approx 2.355\,\sigma. \tag{2.2}$$

The simplest method to obtain $W_{1/2}$ is to take the average of the two widths that surround the half height point. The flow chart (Figure 2.1) is self-explanatory and describes the implemented approach, which is the relationship between the variation of the signal width at peak half height and time. The FWHM approach is applied using a peak-finding algorithm that locates the peak maximum (Y_{max}), then locates the first positions on either side where the y-value falls to $\frac{1}{2}Y_{max}$, and thereby gives the $W_{1/2}$ value. The variance is then calculated from the relationship between $W_{1/2}$ and the peak variance stated in Equation 2.2. Finally, the peak variance is plotted against the diffusion time and D is simply calculated from the slope of this linear curve. In sum, FWHM is an indicator of peak broadening and variations during the diffusion process. However, the variance can be directly extracted by curve fitting, too.

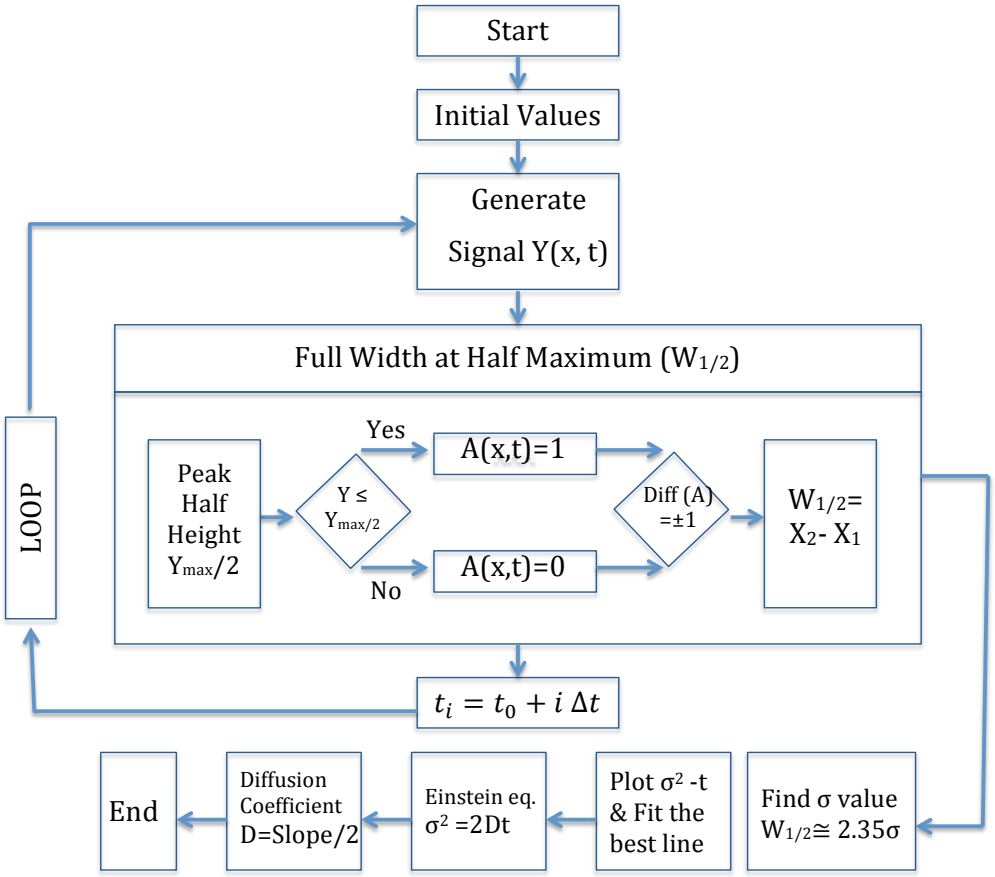

Figure 2.1: Algorithm for time domain calculation by full width at half maximum method.

Curve Fitting

Quantitative analysis by curve fitting is very popular in chromatographic methods, because it directly provides parameters such as variance, and the peak shape parameters. Beside its advantages, curve fitting intrinsically imposes an uncertainty to the results. Uncertainty sources of this approach include the baseline subtraction, the selected fitting boundaries, and the dependence of the fitted parameter values on initial ones. In this study, single and multiple term Gaussian models were fitted to the data, demonstrating the graphical results.

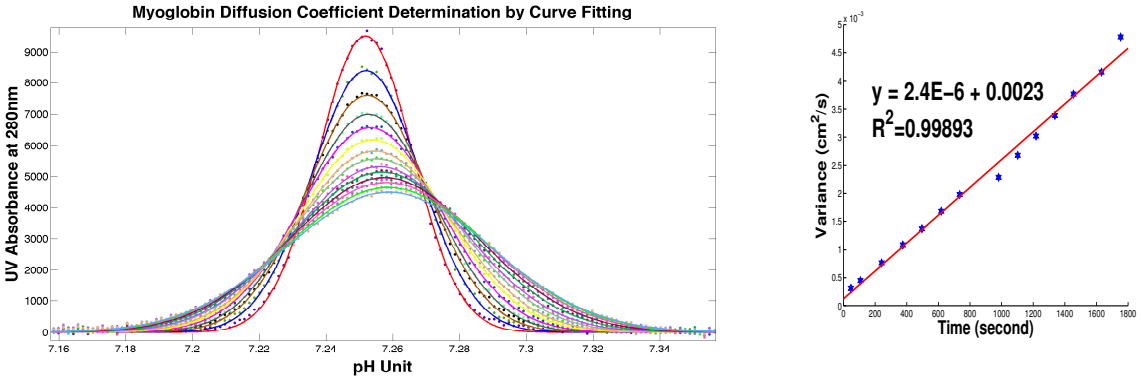

Figure 2.2: Gaussian fitted model to the diffusion pattern of myoglobin. Experimental conditions: 0.35 mg/ml sample solution containing 2% pH gradient 3-10 under voltage gradient 0.5kV for 3min and 3kV for 7min. Sample plug dispersion was scanned with 2 min/scan rate for 30 min.

Gaussian Model. In an experimental example, the concentration profile of myoglobin was measured at different times. At each time point, the concentration profile was fitted with a Gaussian function and the variances were plotted as a function of time (Figure 2.2). The estimation of myoglobin's diffusion coefficient showed a fairly similar accuracy with both FWHM and Gaussian curve-fitting approaches (Table 3.1). This agreement was expected as in both techniques the Gaussian assumption has been met, which leads to a good estimation of myoglobin diffusion coefficient in the time domain. However, the single Gaussian function does not perfectly fit with all experimental data.

Multiple-term Gaussian Model. The use of curve fitting to obtain reliable quantitative information about electrophoresis data requires an accurate representation of the band-shape by the fitted model. As will be shown in Chapter 3, electrophoresis peaks do not necessarily have a Gaussian shape. In such cases, multiple-term Gaussian (MTG) model can be employed, which takes deviations from normal distribution into account by convolving multiple Gaussian terms. The diffusion coefficient is estimated more accurately with those proteins whose peaks conform to Gaussian shapes than with proteins whose profiles deviate from Gaussian shape. Examples of non-Gaussian profiles are carbonic anhydrase (Figure 2.3) and bovine serum albumin, BSA, (Figure 2.4), and both produce large errors when fitted to a Gaussian model. These experimental data did not properly fit to a single Gaussian model; however, fitting a multiple term Gaussian function to the data

significantly reduced the error and improved in the diffusion coefficient estimation for these two proteins (Table 3.2).

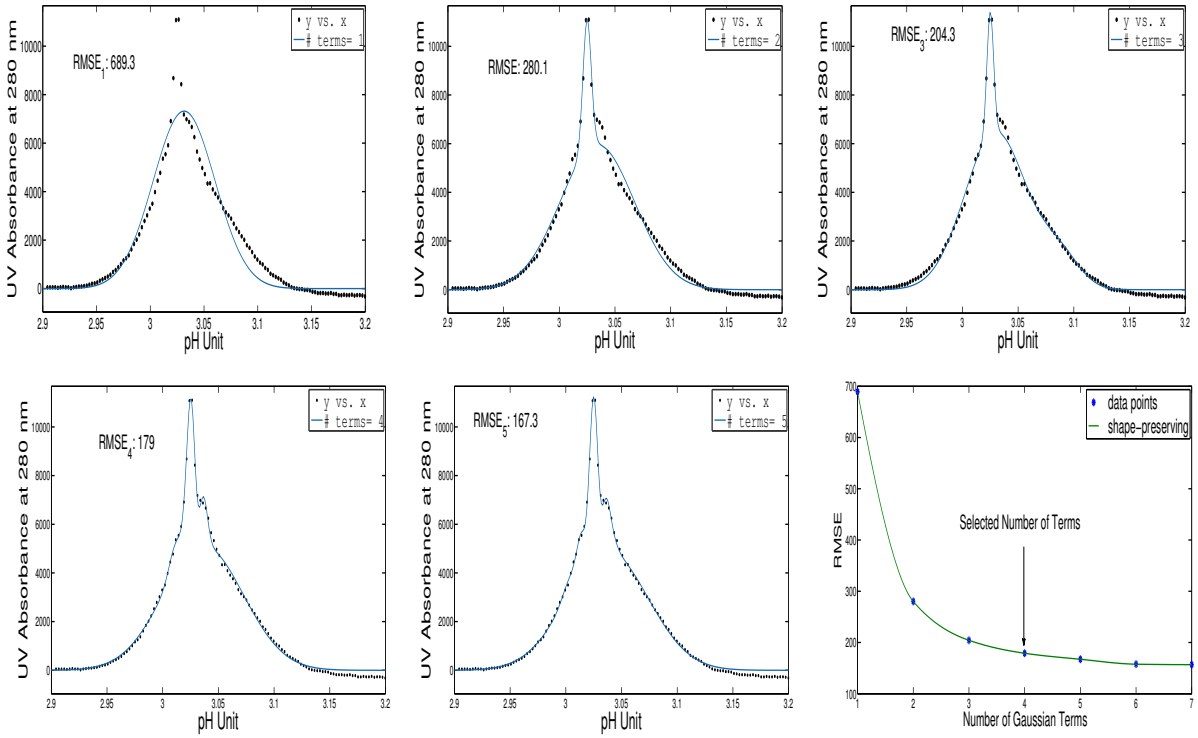

Figure 2.3: Multiple-term Gaussian model curve fitting to initial profile of carbonic anhydrase I. Goodness of fit for MTG (4-term): R-square: 0.995, RMSE: 179.

After fitting data with each model, the goodness of fit should be evaluated by visual and numerical examination; graphical display aids visual interpretation, while computing goodness-of-fit statistics yields numerical measures that allow statistical reasoning. A simple model that is easy to interpret is also important in achieving a good fit.

Root mean squared error, also known as the fit standard error, is a frequently used measure of the difference between values predicted by a model and the values actually observed from the experiment. These individual differences are also called residuals, and the RMSE comprises all residuals into a single measure of goodness of fit. It is defined as:

$$\text{RMSE} = \sqrt{\frac{\sum_{i=1}^{n}(X_{Obs.,i} - X_{Mod.,i})^2}{n}}. \tag{2.3}$$

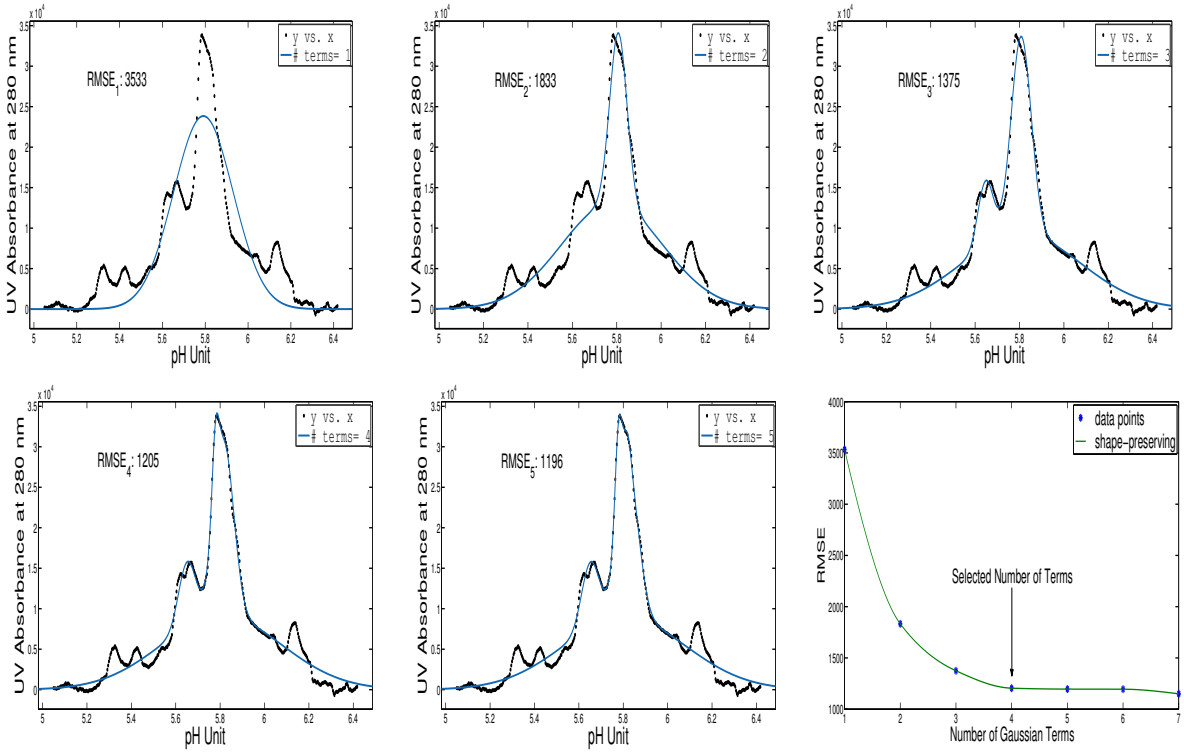

Figure 2.4: Multiple-term Gaussian model curve fitting to initial profile of bovine serum albumin (BSA). Goodness of fit for MTG (4-term): R-square: 0.986, RMSE: 1205.

where $X_{Obs.}$ is observed values and $X_{Mod.}$ is modelled values at place i.

In order to find a simple and efficient model that fits the data appropriately, one needs to compromise between simplicity of the proposed model (lower number of parameters) and improvement in the goodness-of-fit (smaller RMSE). In both examples, the RSME decreased dramatically with the introduction of a second Gaussian term, whereas addition of further terms produced rapidly diminishing improvements in RMSE. The optimum point was determined by reaching a plateau, where the changes in the RMSE was negligible by making the model more complicated.

The diffusion pattern of an analyte is recorded by plotting its concentration profiles at given intervals for a certain period of time; hence, the signal shapes become smoother at longer measurement times and can be fit to simpler MTG models. In the case of carbonic anhydrase and albumin (Figures 3.5 and 3.4), this change was not significant, therefore the same MTG model was fitted to all the curves in time series. The experimental results

of the multiple-term Gaussian model are provided in Section 3.4.3, in addition to the corresponding calculations for estimation of parameters in the time domain.

2.2.2 Frequency Domain Calculations

The Fourier transformation converts the time function into a sum of sine waves of different frequencies, each of which represents a frequency component. Each component is described by a complex number, such that the real part represents its amplitude, and the imaginary part represents its phase angle [88]. In the context of the current study, the phase angle is not meaningful and is therefore discarded.

$$C(x,t) = \frac{1}{\sqrt{2\pi}} \int_{-\infty}^{\infty} \tilde{C}(\omega,t)\ e^{-i\omega x}\, d\omega \tag{2.4}$$

Where C(x,t) is the concentration profile and $\tilde{C}(\omega,t)$ is its counterpart in the frequency domain, and ω denotes the frequency. The experimental electrophoresis signal, e-gram, is a digitized signal with a finite amount of data-points, which can be implemented in computers by numerical algorithms. The efficient fast Fourier transform (FFT) algorithms [89] was employed for these implementations. The visual abstract of the procedure is presented in a flowchart (Figure 2.5).

The diffusion coefficient value can be estimated from the spatial frequency component decay as diffusion proceeds. In the absence of any dispersive contributions, Fick's second law, Equation 2.5, predicts how diffusion causes concentration to change over time, and shows the rate at which concentrations are changing at any given point in space. The dispersion of the stationary concentration profile C(x,t) obeys the partial differential equation:

$$\frac{\partial C(x,t)}{\partial t} = D\frac{\partial^2 C(x,t)}{\partial x^2} \tag{2.5}$$

In pressure-driven flow in capillary tubing, diffusion should be considered in both radial and longitudinal directions; however, in narrow-bore capillaries and with electro-osmotic flow or under stationary conditions, in the absence of the hydrodynamic flow, there is no substantial concentration gradient in the radial direction, and it suffices to consider diffusion in the longitudinal (x) dimension only. The Fourier transform was applied to the diffusion equation, for a stationary sample plug statically diffusing in a 5-cm-long capillary, which is modeled by the following initial and boundary conditions:

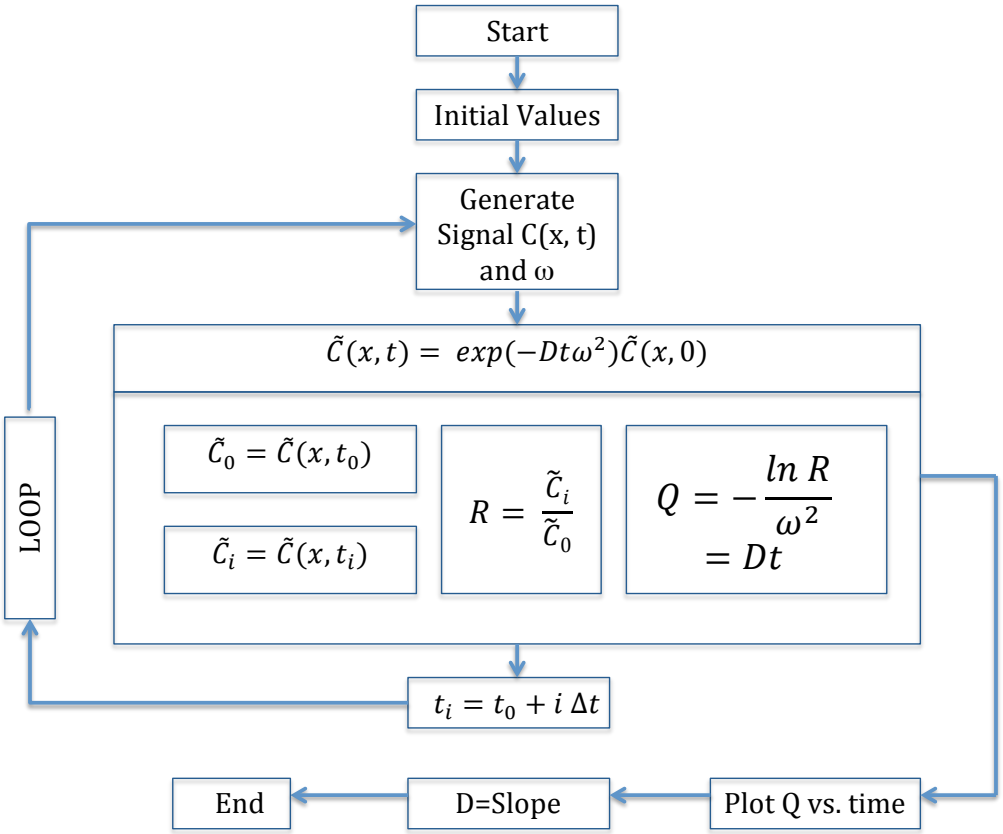

Figure 2.5: Frequency domain calculation flowchart.

$$C_0 = C(x,t_0); C_0 = \frac{1}{2\sqrt{\pi D t_0}} e^{-\frac{x^2}{4Dt_0}}, t_0 = 30s$$

$$C_{ends} = C(2.5,t) = C(-2.5,t) = 0; x = \pm(\frac{5}{2})cm$$

And the concentration profiles at given times, C_i, have a Gaussian distribution over the range $-2.5 < x < 2.5$, with a maximum at the capillary center ($x = 0$). Using assumption of signal periodicity, the time signals are converted to the Fourier domain by discrete fast Fourier transform. Equation 2.5 in the frequency domain can be stated as [90]:

$$\tilde{C}(x,t) = exp[-D\omega^2 t]\tilde{C}(x,t_0) \tag{2.6}$$

where $\tilde{C}(x,t_0)$ and $\tilde{C}(x,t)$ denote the Fourier transforms of the concentration profiles at the initial and given times respectively. According to this equation, the diffusion process can be described as the exponential term, $exp[-D\omega^2 t]$, which filters out the high-frequency components. The diffusion coefficient is extracted by rearranging Equation 2.6, which results in a new term, Q, with a linear dependence on time.

$$Q = \frac{-ln\frac{(\tilde{C}_i)}{(\tilde{C}_0)}}{\omega^2} = Dt \tag{2.7}$$

where $\tilde{C}_0$ and $\tilde{C}_i$ represent $\tilde{C}(x,t_0)$ and $\tilde{C}(x,t)$ in Equation 2.6, and ω stands for the discrete spatial frequency, corresponding to the signal size along x, in pixels. To evaluate ω in Equation 2.7, a scalar vector with same size of signal is built:

$$\omega = n(\frac{2\pi}{T_s \times n}) \tag{2.8}$$

where n is the number of data points in the signal, and the constant $\frac{2\pi}{T_s \times n}$ is used to convert the discrete Fourier transform to a real continuous Fourier transform.

In theory, vector Q is expected to be constant for all ω values. However, in practice, the working region is limited within a finite interval e.g. $\pm 2.5cm$ in this study. This causes the vector Q to vary at the end-points. However, in the mid-points it is constant. Thus, the value of Q is determined in the exact mid-point, Q_m, to have the best approximation possible. In Figure 2.6, the curve is plotted with an example of four time profiles. The value of D is equal to the slope of the linear curve.

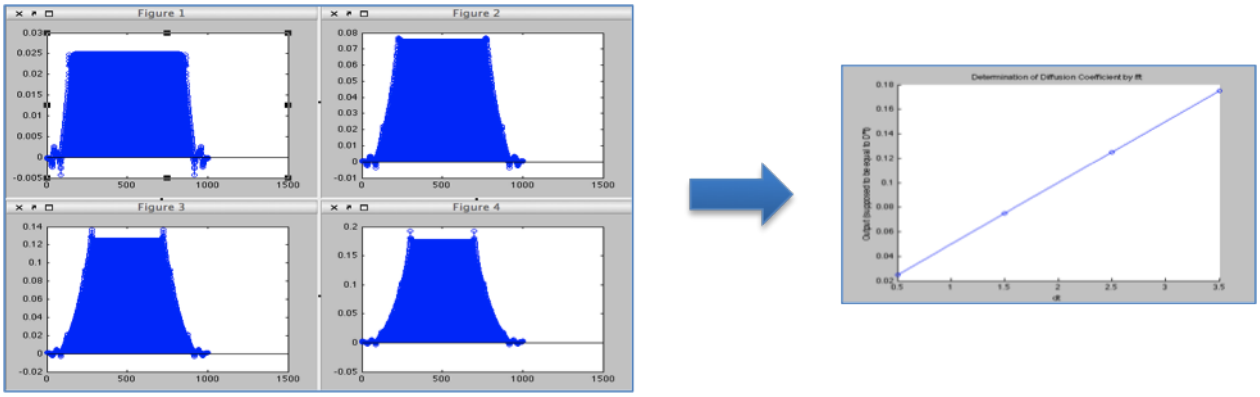

Figure 2.6: The log (frequency ratio) of the peaks are demonstrated vs. ω^2 after division by ω^2. The linear curve is the final output and its slope gives "D".

The Fourier transformed profiles of decaying signals at all given times are divided by the initial time profile. The Q-versus-time plot provides a linear curve with a slope that corresponds to the diffusion coefficient from the frequency domain.

2.3 Simulation Results and Discussion

The shape independent characteristic of the FT approach was studied through simulations in MatLab (R2013a) software. The effect of spatial and temporal parameters on determination of the diffusion coefficient and the noise tolerance of the technique were investigated.

2.3.1 Signals with Different Peak Shapes

In many analytical techniques, it is common to assume Gaussian signal shape. For instance, in chromatography the dispersion of sample bands is expected to be close to Gaussian in theory. However, in practice, as with CE, experimental conditions distort peak shapes, usually causing them to become asymmetric; hence, Gaussian (G) models must be modified to take these effects into account. Examples of such modified models are exponentially Modified Gaussian (EMG) [91], and Exponential-Gaussian Hybrid (EGH) functions [92] in which Gaussian peak models are modified. Further examples of proposed chromatographic models can be found in [93] and references cited therein. Moreover, references [94,95], have

reviewed the application of various peak shape models in signal processing techniques for capillary electrophoresis, including signal de-noising and baseline correction, both of which are common in electrophoretic separations [96].

The frequency domain approach is able to extract the diffusion coefficient from any shape of the initial concentration profiles, while their direct analysis in the time domain is difficult in the case of non-regular peak shapes. However, the FT method is not totally shape-independent, as it is affected by varying the frequency responses of different peak shapes. To investigate this characteristic of the FT model, three mathematical functions; G, EMG, and BC were subjected to analysis through Fourier transformation. Gaussian is the routine assumption of the electrophoretic and chromatographic peak shapes, while BC and EMG resemble distorted signals. In particular, EMG resembles fronting and tailing peaks, whereas BC resembles rectangular, plug-like signals.

Gaussian (G) Model

The concentration profile C is defined as a function of space and time, with the Gaussian distribution:

$$C(x,t) = \frac{1}{\sigma\sqrt{2\pi}} e^{-(x-\mu)^2/2\sigma^2} \tag{2.9}$$

The Fourier transformation of a Gaussian gives another Gaussian, with an inverse relationship of the variable σ in the two domains [97]. Figure 2.7 demonstrates the diffusion pattern of Gaussian function in the time domain and its counterpart in the frequency domain. As the width of Gaussian in the space increases, the width in the frequency domain decreases; for example, the narrow distribution (blue curve) in x space corresponds to the broad distribution in ω space.

The Gaussian function is frequently used to describe the ideal shape of chromatographic peaks, however most of the real chromatographic peaks are not symmetrical, so in the next section an asymmetry factor (skewness) is introduced to characterize the peak shape.

Exponentially Modified Gaussian (EMG) Model

Deviation from the expected symmetrical Gaussian shape in the electrophoretic peaks can be predicted and avoided by changing the experimental conditions for the electrophoresis run [98, 99]. The peak asymmetry can affect the estimation of diffusion coefficient significantly. For example, peak tailing causes underestimation of the diffusion coefficient, while

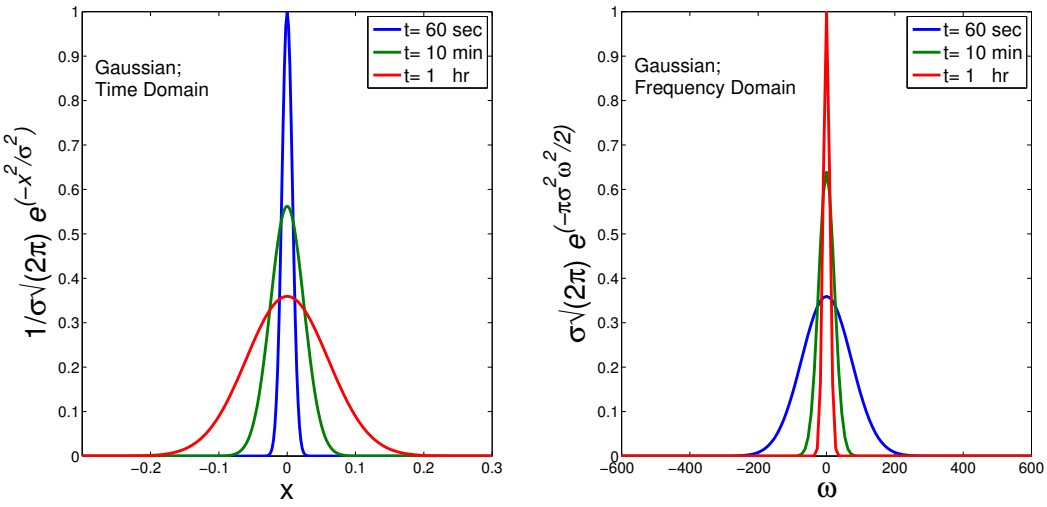

Figure 2.7: Diffusion process illustrated by Gaussian function in time and frequency domains; D=1 $\times$ 10^{-6} (cm^2/s), t=60, 600, and 3600 sec, p=0.002 (cm/pix), $x = \pm 0.35$cm (curves are normalized and scaled to appropriate display range).

sample overload and slow migration in highly concentrated samples lead to overestimation [100].

Among numerous functions that have been used for modelling asymmetric peaks in the literature, the exponentially modified Gaussian is the most popular by far. This function is derived via convolution of two functions, namely, the normal Gaussian (Equation 2.9) and an exponential probability density, which yields the following distribution:

$$C(x,t)_\lambda = \frac{\lambda}{2} e^{\frac{\lambda}{2}(2\mu+\lambda\sigma^2-2x)} \operatorname{erfc}\left(\frac{\mu+\lambda\sigma^2-x}{\sqrt{2}\sigma}\right) \tag{2.10}$$

where μ and σ^2 are the mean and variance of the unmodified Gaussian respectively. And λ is the exponential decay rate, which is equal to $\frac{1}{\tau}$. The complementary error function, $\operatorname{erfc}(x)$, is a special function of sigmoid shape that occurs in partial differential equations describing diffusion. It is defined as [101]:

$$\operatorname{erfc}(x) = 1 - \operatorname{erf}(x) = \frac{2}{\sqrt{\pi}} \int_0^x e^{-t^2}\, \mathrm{d}t \tag{2.11}$$

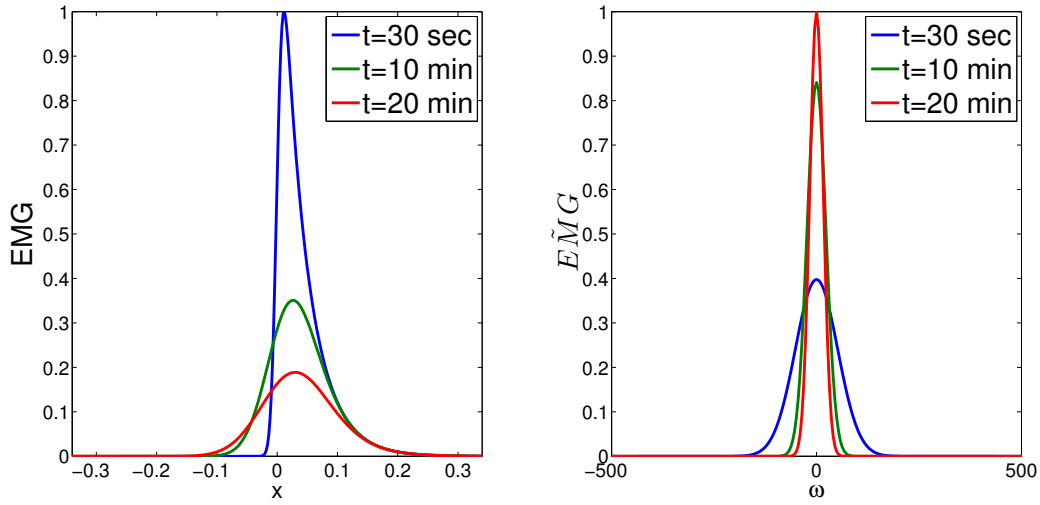

Figure 2.8: Diffusion process modeled by EMG function; D=1 $\times$ $10^{-6}(cm^2/s)$, τ=0.04, t=30, 600, and 1200 sec, p=0.002(cm/pix), $x = \pm 0.35$cm (curves are normalized and scaled to appropriate display range).

The EMG distribution parameters can be estimated by its mean $(\mu + \tau)$, variance $(\sigma^2 + \tau^2)$, and the asymmetry factor $(\frac{\tau}{\sigma})$, which is used to describe the overall shape of an EMG peak. The EMG function in the time domain and the real part of its Fourier counterpart are demonstrated in Figure 2.8; the width of a signal in the Fourier domain is inversely proportional to its width in the time domain.

Simplified approximations have generally been used, due to the complexity of the EMG function. The peak parameters can be approximated graphically or by calculation based on measuring the peak height, half-width and full-width in the time domain [102, 103]. However, Felinger et al. proved that many problems associated with the EMG model in the time domain can be addressed in the frequency domain. They generated asymmetrical peaks according to the EMG function (Equation 2.10). Then, the Fourier transforms of the signals were calculated. The peak parameters were determined by the extended Kalman filter by using both the real and the imaginary parts of the Fourier transformed signal [104].

Robustness of the Fourier transformation approach was examined in Felinger's study by choosing particularly high peak asymmetry for this calculation. The peak shape parameters were correctly determined when the long tail of an asymmetric peak was buried in high noise, which reinforced an important feature of the parameter estimation in the frequency domain. Unlike the FT technique, data processing in the time domain overestimates σ, and

underestimates τ, when estimating the peak shape parameters at high noise levels [104].

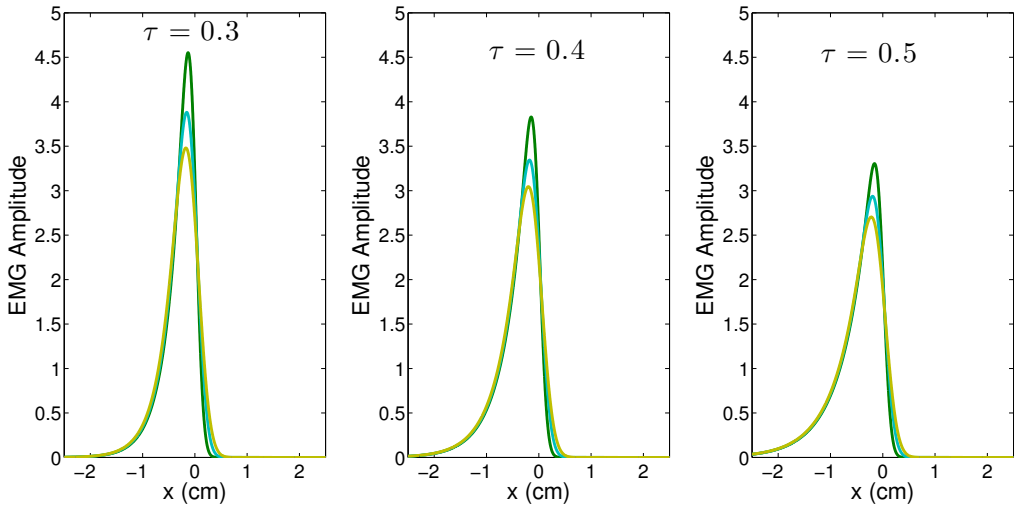

Figure 2.9: EMG signals with different levels of asymmetry and truncation; τ=0.3, 0.4, and 0.5, D=$1 \times 10^{-5}(cm^2/s)$, t=600, 1200, and 1800 sec, p=0.002(cm/pix), $x = \pm 2.5$cm.

Overall, it is evident that the EMG function lends itself quite well to the modeling of asymmetric signals. Depending on the values of the exponential parameter, τ, the distribution will vary from almost normal to almost exponential.

τ value	0.3	0.4	0.5	0.7
% $E_{Freq.}$	0.2	1.0	2.4	6.3

Table 2.1: Estimation of diffusion coefficient from EMG signals by frequency analysis; D=$1 \times 10^{-6}(cm^2/s)$,t_0=30 sec, t_i= 1 min , t=30 min , p=0.002(cm/pix), $x = \pm 2.5$cm.

Keeping all parameters constant, except the exponential decay value produces variation in the levels of asymmetry and *truncation*. In the FT method, the signal is assumed to be periodic, which means it starts from zero, rises to a maximum, and falls to zero again within a time period. In a finite sampling region, i.e. $x = \pm 2.5$ cm in Figure 2.9, at higher τ values the signal is truncated, which smears out the spectrum in the frequency domain. This smearing is spectral leakage, where a truncated periodic function in the time domain results in additional frequency components that do not exist in the original function, due to the change from end to end. Leakage can be reduced by taking more samples (wider windows of data), i.e. increasing x range (Section 2.3.3, Table 2.2).

The results in Table 2.1 show the effect of truncation error. The diffusion process is simulated for a set of different truncated asymmetric signals, and the diffusion coefficient has been estimated for the signals varying from slightly deviated from Gaussian to more exponential-like peak shape.

Boxcar (BC) Model

The Boxcar function is introduced to model non-Gaussian peak shapes such as those produced by the application of a large sample in the pre-concentration injection. Such a signal will be largely rectangular, but the boundaries will assume a sigmoidal shape due to diffusion. The Boxcar function is described by the following equation [105]:

$$C(x,t) = \frac{C_0}{2}\left|\text{erf}\left(\frac{h+x}{\sigma\sqrt{2}}\right) + \text{erf}\left(\frac{h-x}{\sigma\sqrt{2}}\right)\right| \tag{2.12}$$

In this equation, $C(x,t)$ denotes the concentration profile as a function of space and time with standard deviation of σ, and h as an experimentally determined constant. As demonstrated in Figure 2.10, the concentration profile is zero over the entire real line except for a single interval where it is equal to a constant (C_0).

The counterpart of the boxcar function in the frequency domain is defined by "sine cardinal" or $sinc(x)$ function. In digital signal processing, the normalized $sinc$ function is commonly defined by $\text{sinc}(x) = \frac{\sin(\pi x)}{\pi x}$. The value at $x = 0$ is defined to be the limiting value $sinc(0) = 1$. As time passes the rectangular shape of the signal become more Gaussian-like, and larger plug lengths lead to a delay in the transition from a Boxcar to a Gaussian profile of smearing peaks. Therefore, the signal has high frequencies even at longer times.

The larger the injection volume, the more deviation is expected from the Gaussian peak shape, whereas smaller injection volumes lead to poorer repeatability [106]. As expected, optimizing parameters such as sampling length, resolution, and initial time makes estimation more accurate. For example, narrower rectangular signals ($h = 0.01 - 0.25cm$) within the x-range=$\pm 10\sigma$ provided good estimations, while for broader h values; an increase in the sampling region was needed to avoid truncation error.

Effect of Different Concentration Distributions

Diffusion acts as a filter that cuts high frequencies. In the beginning, the steepest gradient between sample and surrounding buffer exists; thus, distinct borders create higher

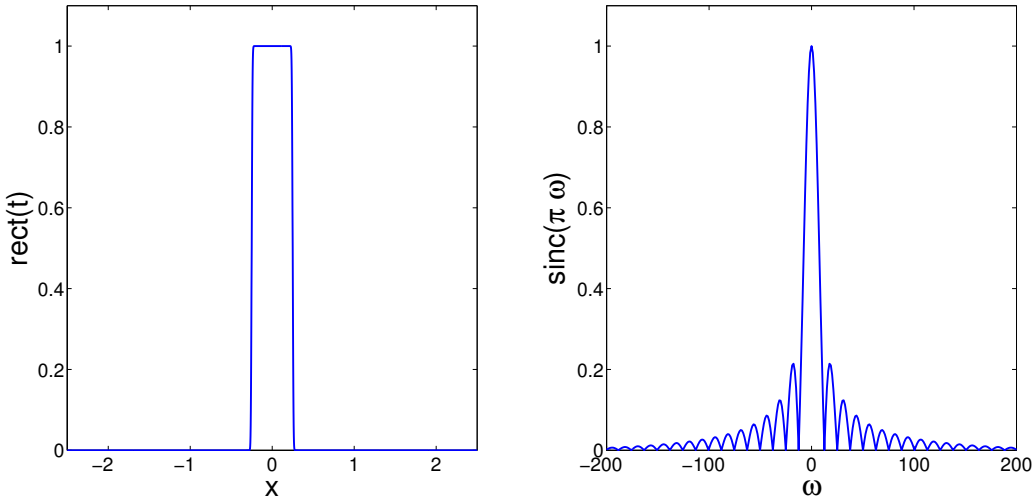

Figure 2.10: Boxcar function and its frequency domain conjugate pair; D=$1 \times 10^{-6}(cm^2/s)$, h=0.25, t=300 sec, p=0.002(cm/pix), $x = \pm 2.5$cm (scaled to appropriate display range).

frequencies. As time passes, the peak shapes become broader and lose high their frequency components.

The effect of signal shapes on the frequency domain results proves that this method is not totally independent from the shape, although it is not restricted to any peak shape assumption as it is in the time domain. Depending on the frequency content of each function, the results are varying.

2.3.2 Optimization of Spatial and Temporal Parameters

The spatial decay of the sample plug over time is considered diffusion process. Hence, the Gaussian function is used to optimize both spatial and temporal aspects of the analysis. The assigned initial values are adopted from experimental conditions (instrument iCE280):

- Diffusion coefficient, moderate molecular weight proteins D=$1 \times 10^{-6}(\frac{cm^2}{s})$.
- Resolution, the camera pixels over the column length, $p = 0.002(\frac{cm}{pix})$.
- Imaging starts at $t_0 > 0$, with an acquisition rate limited by the duration of a single scan (30 s).

2.3.3 Spatial Perspective

In addition to choosing an appropriate spatial resolution, it is crucial to select the working region properly. In terms of resolution, the number of pixels, which is determined by the camera, and the sampling length are studied.

Selected Region Monitoring

Selected region monitoring (SRM) or choosing an effective range, which brackets the desired peak, is of high importance and affects the results significantly. The whole signal is not taken into account for the analysis; instead, the effective range is limited to the main peak surrounded by a number of adjacent pixels. There are several advantages resulting from this confinement, provided it has been determined insightfully. By limiting signal detection to the desired section, much irrelevant information including noise, spikes, and the peaks caused by other components that may be present in the sample are ignored. At the same time, the baseline corrections, the noise filtering, or any other kind of signal processing can be focused on this selected region.

As Table 2.2 shows, the error percent in the frequency domain, $Error\%_{(Freq.)}$, is huge due to truncation of the signal in small detection interval such as $\pm\sigma$. Therefore, one needs to take the band width of the signal into account to specify the monitoring region, especially for broad peaks. The SRM is significantly important when there are spikes in the electropherogram. It can be corrected by choosing the proper compromise between signal preservation and spike removal. The effectiveness of this correction will depend on the distance between the main peak and the spike.

Selected Region	$\pm\sigma$	$\pm2\sigma$	$\pm5\sigma$	$\pm10\sigma$	Whole channel
X-limits (cm)	±0.035	±0.07	±0.175	±0.35	±2.5
$\%Error_{(Freq.)}$	65	27	0.6	0.6	1

Table 2.2: Effect of SRM on determination of D, (D=1×10^{-6} (cm^2/s), $t_0 = 30$ s, $t_i = 30$ s, $t_t = 30min$, p=0.002 (cm/pix), SNR=3, n=1000).

Different D values are associated with different multiples of σ. Using Einstien equation (Eq. 2.1), the σ is calculated at the final time where the peak is in its broadest shape. The error associated with $\pm(5-10)\sigma$ is lower than 0.6%, as shown in Table 2.2. An effective

sampling length that only brackets the desired peak will improve results by removing irrelevant information such as noisy baseline and spikes. The proper selection of the sampling interval can be studied by convolving the Gaussian function with a boxcar window; if the peak is not fairly preserved, the truncated signal creates false high frequencies that affect the estimation severely. Working within the $\pm 10\sigma$ range is determined as the optimum peak region in order to eliminate artifacts while preserving the peak.

Resolution

Image resolution of the camera is determined by the number of pixels in the camera, which is 2048 in the iCE280 instrument, and by the length of the column cartridge, which is 5 cm. Thus, if the whole column is imaged, a resolution of approximately 0.002 ($\frac{cm}{pix}$) will be obtained. The pixel positions map the spatial data series into the time domain, and a time-to-frequency converter transforms the temporal signal to the corresponding frequency-domain data. To find the limiting resolution, the narrowest variance of the diffusing plugs $(\sigma_0)^2$ can be calculated at the initial time. In practice, the sample plug is not an infinitely sharp zone, and in experiments, $t_0 = 0$ denotes the immediate scan after electric field removal. In the simulation, the initial time is set to the first scan interval t_0=30 s because the delta Dirac function generates a line which is smaller than the digitized pixel size.

Division (cm/pix)	0.01	0.007	0.0035	0.002	0.001	0.0002	0.0001
No. Data Points	85	120	240	420	840	4200	8400
$\%Error_{(Freq.)}$	1.7	1.3	0.8	0.6	0.4	0.2	0.1

Table 2.3: Effect of resolution on determination of D, (D=1 $\times$ 10^{-6} (cm^2/s), t_0 = 30 s, t_i = 30 s, t_t = 30 min, Selected Region=$\pm 10\sigma$, SNR=3, n=1000).

High frequency details can be enhanced by sharpening the edges through an increase in camera resolution, but random noise also has a high spatial frequency characteristic that can cause artifacts. As shown in Table 2.3, the frequency domain analysis worked efficiently even at low resolutions. Hence, simulation results suggested that the resolution of the instrument was sufficient for this purpose, and the small potential improvement in the results did not justify the expense of a higher resolution camera.

When only a selected segment of the column is monitored, for example, the $\pm 10\sigma$ region discussed above, the imaging window will increase, which will in principle result in a more

precise signal and a more accurate estimation of diffusion coefficient. When the FWHM approach is employed in the time domain, the results will not be significantly affected by the image resolution, because only four points are taken into account for the determination of $W_{1/2}$. Other techniques used in time domain, such as curve fitting, are more significantly influenced by alteration of resolution, because all data points are evaluated.

2.3.4 Temporal Perspective

It is important to investigate how long and at what frequency the diffusing signals should be recorded. Short analysis time is desirable for the sake of high sample throughput, while a longer period would allow for reducing the error by the averaging of multiple data points and provide increased precision and accuracy [107]. The nature of the diffusing analytes needs to be taken into account for optimization of diffusion coefficient calculations. For instance, amino acids and smaller peptides with fast diffusive behavior will have shorter optimum total times, while the diffusion process of big proteins with small diffusion coefficients needs to be monitored for a longer period.

Total Measurement Time

It has been always of great importance to save time to increase the analysis throughput, while at the same time preserving the precision and accuracy of the measurement. At a given noise level, the slope of the linear curve varies at different lengths of analysis time. Three time windows of 10, 30, and 60 min were studied, representing short, medium, and long periods, respectively.

As it is demonstrated in Figure 2.11 along with the results in Table 2.4, a slight difference in the slope of the curves affects the results significantly, revealing the sensitivity of the measurement toward total time. The effective diffusion time depends on the sample's diffusive behaviour, as well as the variation of the SNR with time. For example, small solutes with large diffusion coefficients need to be recorded with consecutive scans at short intervals that convey the most useful information on their diffusion. The weaker signal-to-noise ratio at longer time periods makes the collected data less reliable; therefore, the non-linearity increased by taking them into account. At higher noise levels this effect is more significant.

The linearity and goodness of the fit are two important factors which can be characterized using the R^2 and RMSE. Both in the simulation and the real data analysis, the lowest RMSE and best correlation are observed at short and medium measurement times.

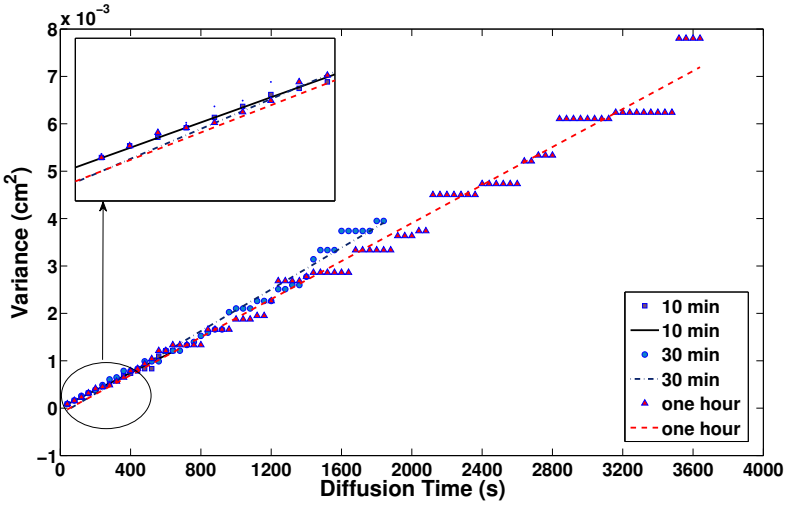

Figure 2.11: Determination of diffusion coefficient at 10, 30, and 60 min total time, (D=1 $\times$ 10^{-6} cm^2/s, t_0 = 30 s, t_i = 30 s, p=0.001 (cm/pix), SNR=15, n=1000).

However, the scattered data points collected at longer times do not affect the slope of the curve significantly because the data clusters are bouncing on either side of the linear curve (Figure 2.11).

The effect of total measurement time is further explored with an emphasis on the variation of the signal-to-noise-ratio and the diffusion rate of the analyte.

Noise level. In the diffusion process, the amplitude of the decaying signals are attenuating with time, while the noise energy remains constant. Thus, the SNR value is changing toward lower signal-to-noise ratios with time (Section 2.4.1). As more time goes by, the signal-to-noise ratio will decrease and the data points obtained at later time points are less reliable than those recorded at earlier time points. It should be considered though that the signal-to-noise ratio is expected to be high with CIEF and iPF, since both methods focus the sample and concentrate it in a narrow zone.

There is a trade-off in the determination of the total time. When choosing a longer analysis time, one can take advantage of the averaging of more scans; however, this comes at the cost of counting less reliable collected data from broader peaks with poorer SNRs. The one-hour measurements at fast scans showed greater error due to a larger number of unreliable data sets, which were collected at poor SNR values, while shorter period

Total Time	10min	30min	60min
D_{est} ($\times 10^6$)	0.97	1.02	1.11
CI_{95} ($\times 10^6$)	0.01	0.01	0.02
%Error	2.6	2.6	11.4
R^2	0.992	0.990	0.956

Table 2.4: Effect of total analysis time on determination of D, at 10, 30, and 60 min total time, (D=1 $\times$ $10^{-6} cm^2/s$, t_0 = 30 s, t_i = 30 s, p=0.001 (cm/pix), SNR=15, n=1000.

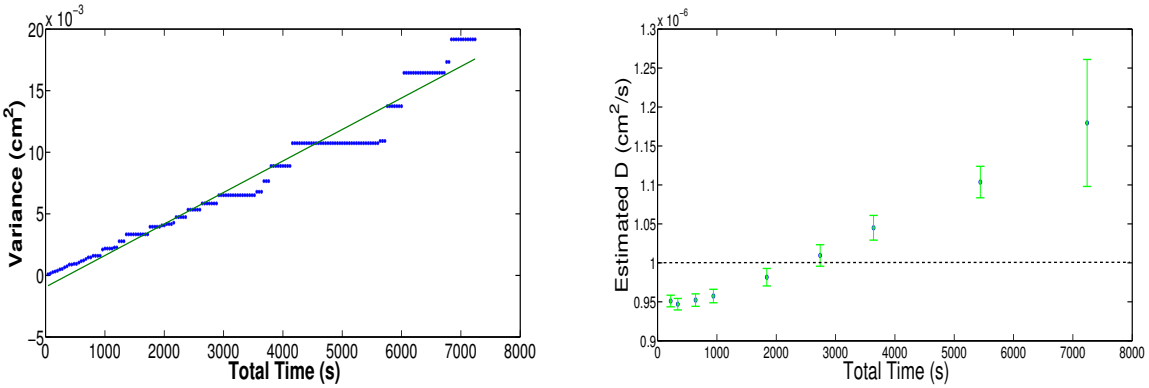

Figure 2.12: Effect of total measurement time on estimation of "D" due to attenuation of SNR at longer times; ($D = 10^{-6}$ cm^2/s, t_0 = 30 s, p=0.001 cm/pix, SNR=15, n = 1000). Dashed line determines the D true value.

measurements revealed better estimation at fast successive scans.

According to the estimation of diffusion coefficient within a wide range of 3 min to 2 hours; the graphical results in Figure 2.12 shows that the estimated values at 30-minute and 45-minute total time have the best accuracy. The 30-minute period was determined to be the best length of recording the diffusion process for the employed simulation condition, because of slightly better precision (lower confidence interval), and also saving in the run time of the programs.

Furthermore, it is worth mentioning that, between the two experimental approaches used in this study, the plug flow method can be performed within a shorter time span, since it skips the focusing step, and the sample is instead introduced into the capillary with stacking and plug flow. A short period for the defocusing process is desirable, but the time period should be chosen with circumspection in order to gain reliable diffusion

coefficient measurement.

The nature of the analyte. As discussed before, there is a direct relationship between the variance and the diffusing time, which is determined by the diffusion coefficient. The steeper the slope of σ^2 vs. t plot, the larger the D value is that determines how fast the variances change within a short period of time. Hence, the nature of diffusing analyte is an important factor in optimization of diffusion total time.

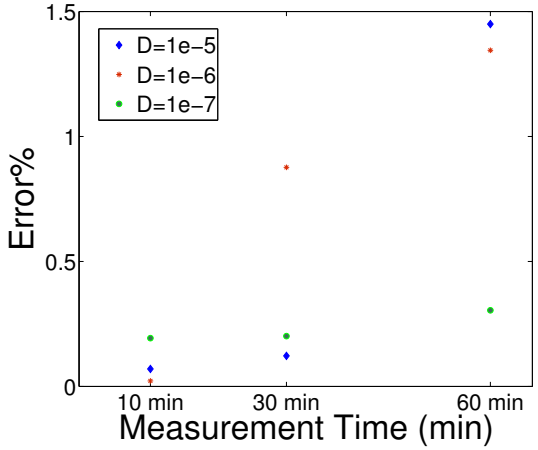

Figure 2.13: Effect of diffusive behaviour on measurement time; D=$10^{-5}, 10^{-6}$, and $10^{-7}(cm^2/s)$, t_0 = 30 s, t_i = 30 s, p=0.001 (cm/pix), SNR=15, n=1000.

In the case of fast diffusive species such as amino acids and small peptides, which have large diffusion coefficients, e.g. $10^{-5}\frac{cm^2}{s}$, the diffusion rates are high and therefore shorter total measurement time is favourable. In contrast, with larger molecules like proteins that have small diffusion coefficients, longer periods is needed for effective monitoring of the diffusion pattern. It can be also concluded from the results in Figure 2.13, by comparing three diffusion coefficient values varying one order of magnitude, as it was expected the faster species with larger diffusion coefficient exhibits better results in shorter time.

Considering the influential factors on the total measurement time, one can conclude that for example the light proteins with large D values that have fast decay rates and the signal will buried in noise soon. Hence, sampling in short time with fast scan rate is favourable.

Data Acquisition Rate

The sampling rate was investigated from two viewpoints by averaging different number of data points at a given total time and by considering the reliability of the collected data. The simulation results in the scatter plot, Figure 2.14, demonstrate that the scan intervals did not significantly affect the estimation, and the error percent remained below one percent even at low temporal resolution of 5 minutes. The slow scanning rate at short measurement time can not provide sufficient number of data points and lack the averaging advantage. On the other hand, short scanning interval at longer total measurement time will enhance the weight of more noisy signals and result in more error.

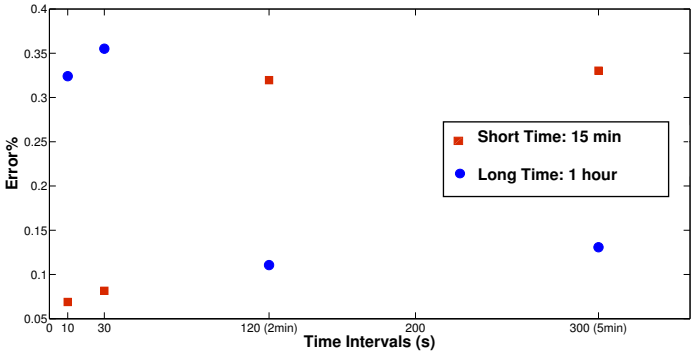

Figure 2.14: Effect of data acquisition rate on determination of diffusion coefficient (D=$1 \times 10^{-6} cm^2/s$, t_0=30s, p=0.001 (cm/pix), SNR=3, n=1000) at variable intervals; Total time 15, and 60 min.

The iCE280 instrument is capable of scanning at a 30 $\frac{sec}{scan}$ rate, which fulfils the sampling rate needed for estimation of the diffusion coefficient under the employed conditions.

2.4 Technique Robustness; *Noise tolerance*

Amongst the parameters that would affect the determination of the diffusion coefficient, noise is an inherent feature of any instrumental technique; hence, much effort has gone into increasing the signal-to-noise ratio. The noise tolerance of the models is investigated both in the time and the frequency domain. The Gaussian function is chosen to examine the robustness of the technique, because it resembles the impulse response of many natural systems. Additionally, the employed FWHM approach is specified for Gaussian shape in the time domain.

2.4.1 Random Noise Generation

The random noise generator adds white Gaussian noise to the signal, which has a uniform probability density function in the frequency domain. In the diffusion pattern, the amplitude of the decaying signals is attenuating with time, while the noise energy remains constant. Thus, the SNR value becomes poorer as time passes. The SNR is calculated from the amplitudes of the signal, A_{signal}, and the noise, A_{noise}, and is expressed in the logarithmic decibel scale:

$$\mathrm{SNR_{dB}} = 10 \log_{10} \left(\frac{A_{\mathrm{signal}}}{A_{\mathrm{noise}}} \right)^2 \tag{2.13}$$

In the present study, the A_{signal} is the undistorted average power of the signal at the initial time, which determines constant noise level according to the given SNR. By knowing the desired SNR and the signal power, appropriate noise energy can be calculated from rearranging the Equation 2.13, and produced with a random number generator. Keeping the noise level constant, shorter and broader peaks at longer diffusion times are subject to lower signal-to-noise ratios.

2.4.2 Noise Sensitivity

The results of diffusion coefficient calculations can be significantly affected by noise. In fact noise does not convey any useful information so it should be reduced by filtering the distorted signal.

SNR	1	3	5	15	50
$\%E_{(Time)}$	37	24	18	6	5
$\%E_{(Freq.)}$	0.7	0.6	0.4	0.1	0.0

Table 2.5: Technique robustness toward noise, error percent in estimation of D by FWHM and FT methods, D= $1 \times 10^{-6} (cm^2/s)$, t_0=30 s, t_i=30 s, t_t=30 min, x=$\pm$2.5 cm, n=1000.

As can be concluded from Table 2.5, the use of the FWHM approach for the determination of diffusion coefficients can be significantly affected by noise in comparison to the frequency domain, which is highly tolerant against noise. Estimation of the diffusion

coefficient from the fairly noise-free signals (SNR=50) shows relative standard deviation (RSD) equal to 2 and 0.1 for time and frequency approaches respectively. However, noisy signals in the time domain, FWHM method, more significantly lowers precision (RSD=20) compared to the frequency domain (RSD=1.9).

2.5 Summary and Conclusion

The diffusion process of proteins was simulated and different techniques were employed to estimate the diffusion coefficient in both time and frequency domains. The time domain approaches including full-width at half-height-maximum and curve-fitting are compared to the proposed frequency domain calculation. The principles of each method are explained by taking the signal shapes into account. The FT approach does not require specific assumptions about the peak shape, which contrasts with the assumption of Gaussian peak shape in the time domain. However, the frequency domain technique is not totally independent from the signal shape, as it is affected by varying the frequency responses of different peak shapes such as Boxcar and EMG functions.

The most effective conditions for estimation of the diffusion coefficient are investigated from temporal and spatial points of view. The sampling region needs to be carefully selected to avoid the truncation error, whereas the camera resolution does not significantly affect the results. The optimal length of the observation interval depends on the broadening sample plug characteristic, for example the small solutes with large diffusion coefficient need to be recorded from the very early moments and the excessive scans with short intervals that convey the most useful information on its diffusion, while the slow-diffusing analytes require longer time to reach equilibrium.

An important feature of the calculation in frequency domain was demonstrated by processing noisy signals. Noise with a wide range of signal-to-noise ratio (1-50) was added to computer generated chromatograms. In presence of high noise values, the signal information that is buried in noise can be still retrieved form the noisy signal because of their different frequencies. However, the signal and the noise still share frequencies, and the major limitation of this method is determination of the truncation point in the Fourier domain, to cut off the noise of high frequency.

In the next chapter, the proposed method is validated by CIEF-WCID experiments. Achieving more accurate diffusion coefficients by FT approach proves the effectiveness of the method. Moreover, the shape-independent characteristic of FT method is examined by retrieving the diffusion coefficient from irregular peaks that the traditional methods

cannot cope with. In addition, imaging plug flow analysis (iPF) is introduced as another fast and simple method, the results of which are also evaluated by the FT method.

Chapter 3

Application of Whole Column Imaging Detection in Diffusion Coefficient Measurement

3.1 Introduction

Capillary zone electrophoresis was employed by Bello et al. for the fast measurement of the diffusion coefficients of both small and large molecules [108]. The determination of diffusion coefficients using capillary electrophoresis is generally affected by experimental variation in injection and detection. In order to reduce the influence of such variances on the calculation of D, the "stopped migration" technique can be used [64]; however, such a technique has a lengthy run-time. In order to address this issue, Jin and Chen developed a peak-height method that succeeded in shortening the measurement time while reducing the effect of experimental variation [109]. They have classified the factors influencing the detected CE signal into two categories, namely, the constant or time-independent factors, and the time-dependent ones. Injection, detection, and voltage on-and-off switching fall into the first category, whereas molecular diffusion, Joule heating, adsorption of species, local electric field and flow profile (Fig 1.2) are categorized as time-dependent factors. A numerical correction for the unsteady-state flow caused due to the injection and pumping of solutes in capillary electrophoresis instrument has been devised by Sharma et al. via modification

The results presented in this chapter have been published in: "Accurate Determination of the Diffusion Coefficient of Proteins by Fourier Analysis with Whole Column Imaging Detection" by Zarabadi, A. S.; Pawliszyn, J. Anal. Chem. 2015, 87, 21002106.

to the Taylor analysis [110]. From an instrumental viewpoint, Cottet et al. modified a commercial capillary electrophoresis instrument based on the differential measurement of the peak dispersion using the double detection of the sample zone by superposition of two capillary windows in the same interface [111].

Amongst the employed capillary electrophoresis methods, capillary isoelectric focusing, equipped with whole column imaging detection, is a relatively new, fast, automated, and simple technique. Direct monitoring of the diffusion process in real time, which is enabled by the application of whole-column imaging detection, greatly accelerates analysis. This simple method improves the temporal resolution of diffusion coefficient measurements [45]. Although this approach is known as an effective way of providing diffusion measurements, isoelectric focusing has inherent limitations such as the risk of protein precipitation at the isoelectric point (especially in higher concentrations of the sample and in the low ionic strength media), carrier ampholyte background absorption, and interaction issues [112]. In the present research, a novel technique termed "imaging plug flow" (iPF) is introduced to take advantage of whole-column imaging detection while addressing the drawbacks associated with CIEF method.

In this chapter, two analytical approaches are investigated for determination of D and its application to study protein stability. The two methods are examined from both experimental and data analysis viewpoints. Capillary isoelectric focusing with whole column imaging detection WCID is employed as a method which often provides sharp sample zones and produces peaks of Gaussian shape. The second technique is a simple and fast experimental method for determination of diffusion coefficients. The Fourier transformation technique is employed to determine the diffusion coefficient of a number of proteins in the frequency domain, and the results are compared to the ones obtained from time domain methods.

3.2 Method and Materials

A set of protein diffusion coefficients were measured in real-time fashion by whole column imaging detection method.

3.2.1 Chemicals and Sample Preparation

Pharmalytes (pH 3-10), polyvinylpyrrolidone (PVP) and other proteins were purchased from Sigma. The electrolytes were phosphoric acid and sodium hydroxide 100 mM for the

CIEF experiment, and phosphate buffer (pH 2.4, and concentration: 25 mM, 100 mM) for the iPF experiments. The protein samples were 0.25-0.5 $\frac{mg}{mL}$, containing 2% pharmalytes and 0.5% PVP. Ultrapure water (18 M Ω) from a Barnstead/Thermolyne system (Dubuque, IA, USA) degassed by sonication for 30 minuets and used for the preparation of all samples. The samples were filtered with 0.2 μm pore-size membranes. The cartridge was conditioned with a 0.5% $\frac{w}{v}$ PVP solution.

3.2.2 Instrumentation

All experiments were conducted in a commercial iCE280 analyser (Convergent Bioscience [now Protein Simple], Toronto, Canada). The instrument was equipped with a UV whole column imaging detector that was set to 280 nm. The cartridge (Convergent Bioscience, Toronto, Canada) contains a fused silica capillary with internal fluorocarbon coating, (100 μm i.d.$\times$ 5 cm). Experiments for both methods were conducted on the same system. For the plug flow analysis, a high voltage power supply (Stanford Research Systems, INC. Model PS350) was employed.

3.2.3 Scanning Procedure

The following scanning procedure was employed to record the diffusion process. First, the sample is injected into the cartridge, and a reference image (I_0) of the filled column is scanned prior to the focusing or pre-concentration. Then, the absorption is acquired after applying the electric field. The camera automatically takes images approximately every 30 s. The voltage is switched off when focusing is complete (CIEF) or after the sample plug reaches the middle of the channel (iPF). The protein band then relaxes, resulting in band broadening. The CCD camera then manually scans the dynamic diffusion process. Each image (I_i) is scanned individually at desired intervals, which are timed by a stopwatch. The diffusion images are primarily in the form of light intensity. Therefore, absorption is calculated using these images by dividing all the images to the I_0, and taking a logarithm of the divided images.

3.3 Experimental Techniques

Two different experimental approaches are employed for sample stacking under an electric field. CIEF is based on isoelectric focusing, whereas in iPF, the sample is concentrated due

to field-amplified stacking principals. The signal-to-noise ratio is high for both methods since the sample is concentrated in a narrow zone.

The shape of the sample concentration profile is determined by the employed experimental technique, in addition to the analyte nature. For example, in CIEF, the desired analyte was focused in a narrow band, which was well represented by a Gaussian function, while in iPF, a sample plug was accumulated under the membrane by an electrokinetic injection, which typically results in a boxcar-like profile.

3.3.1 Capillary Isoelectric Focusing (CIEF) Method

The protein sample was hydrodynamically injected to fill the separation column. The initial applied voltage was set at 0.5 kV for 3 min, increased to 3 kV until the focused sample became stable, and then the voltage was turned off; this usually took 10 min overall. The diffusion process commenced as soon as the electric field was disconnected, and the diffusing protein concentration profiles were recorded at the desired time intervals.

3.3.2 Imaging Plug Flow (iPF) Method

As demonstrated in the schematic (3.1), after the stacking step, the generated sample plug is pushed to the channel by applying the electric field between two reservoirs. The sample position is monitored by the whole-column imaging detector; when it has traveled midway through the channel, the voltage is turned off and the diffusing plug is scanned frequently. In the iPF experiment, a commercial cartridge was employed, while the procedure was similar to the on-line pre-concentration method used by Yang et al. [113]. The stacking step can be preceded by an extra buffer wash to sweep sample residuals, which results in a narrower sample zone and prevents tailing.

Sample Stacking. Field-amplified sample stacking is a simple pre-concentration technique that has been developed to address the sensitivity issue in capillary electrophoresis [114, 115]. A sample in a low-conductivity matrix is slightly concentrated under the membrane prior to plug flow and diffusion. An injection voltage of 3 kV generated a current of $\approx 200\ \mu A$, and pre-concentration took 1 min to stack the sample efficiently at this voltage.

Sample Plug Moving. After the sample plug formed under the membrane, it was moved toward the cathode by a voltage of 0.5 kV, which was disconnected after the plug reached the middle of the channel. Despite the low voltage of 0.5 kV, the plug was driven to the middle of the channel within two minutes. High electrophoretic mobility of the species and the electro-osmotic flow, positively contribute in the velocity of the plug. Capillary conditioning slows down the plug movement by reducing the EOF effect.

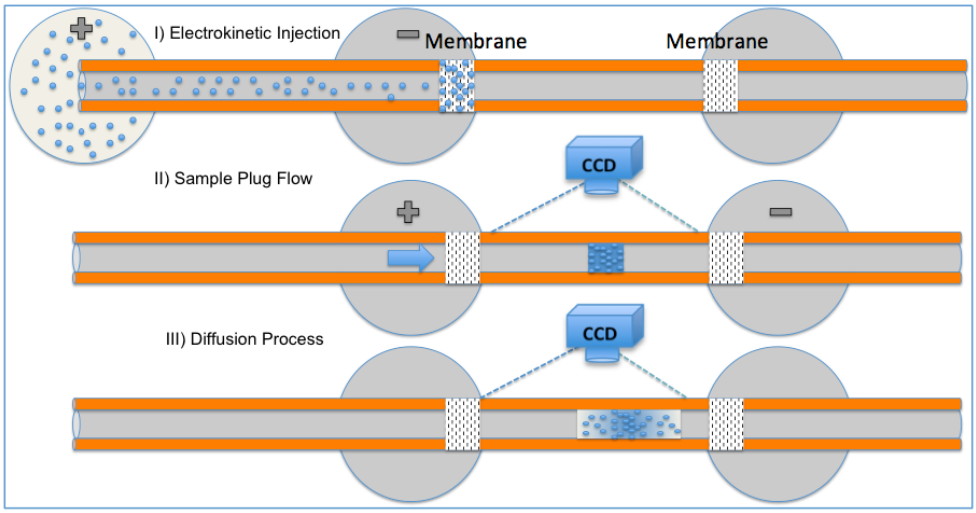

Figure 3.1: Stages of the iPF experiment. (I) Injection: protein is eletrokinetically loaded and accumulated under the membrane, and then the residuals are swept to make a narrow zone. (II) Plug Flow: conventional CE operation under electric field. (III) Imaging Diffusion Process: CCD camera captures the images of the diffusing sample plug in absence of the electric field.

Concentrated buffers will generate high currents and Joule heating and should therefore be avoided. Appropriate choice of buffer pH can reduce the wall-adsorption, which influences the determination of diffusion coefficient. For example, choosing a buffer with pH above the pI of the species, leads to a negative net charge on both the molecule and capillary wall [109]. The protein samples were dissolved in 25 mM buffer with pH=2.5, while the run buffer concentration was 100 mM. The stacking time and voltage were determined according to the generated current in order to acquire the sample plug within a short time and without precipitation.

3.4 Results and Discussion

As capillary electrophoresis peaks are not perfectly Gaussian, this creates an error in the time domain calculations. As proven by the simulations, Fourier analysis is an alternative approach that can be applied to address this drawback. This technique facilitates employment of various instrumental methods such as iPF regardless of the peak shape. In this section, a set of experiments is conducted in CIEF and iPF, followed by efficient data analysis in the Frequency domain. The shape independent feature of the frequency domain analysis is demonstrated by the analysis of proteins with different peak shapes.

3.4.1 Accurate Determination of Diffusion Coefficient

The diffusion coefficients of several proteins have been determined by CIEF, and analysed in both the time and frequency domains. The results are summarized in Table 3.1, and accuracy was investigated by comparing with literature values. However, D values are primarily dependent on the empirical measurement technique used for their determination; for example, in CIEF, they are collected at zero net charge (pI), whereas in iPF, the intermolecular electrostatic forces are present. As it is evident from the experimental results, diffusion coefficients determined using FT agree much better with literature values than those obtained with time domain methods. The precision of the collected data was also improved when using the Fourier analysis for estimation of diffusion coefficient. Reproducibility is improved by the FT approach, with the RSD below 8% for three replicates; whereas, it is up to 17% in the time domain calculations.

Protein	$^*D_{Freq.}$	$^*D_{Time}$		$^*D_{Lit.}$	$^*\lvert D_{Lit.} - D_{Est.}\rvert$			Ref.
		FWHM	Fitting		Freq.	FWHM	Fitting	
Angiotensin	25.4(±0.8)	29.6 [45]	23.7(±2.5)	25.25	0.2	4.4	1.6	[116]
β-lactoglobulin A	6.9 (±0.5)	9.3(±1.6)	9.3(±1.1)	7.38	0.5	1.9	1.9	[117]
β-lactoglobulin B	3.1 (±0.2)	4.0(±0.6)	2.6(±0.3)	3.14	0.0	0.9	0.5	[118]
Albumin (BSA)	5.1(±0.2)	7.75 [45]	2.9(±0.2)	5.90	0.8	1.85	3.0	[119]
Carbonic Anhydrase I	10.6(±0.5)	9.36 [45]	7.7 (±0.5)	10.66	0.1	1.30	3.0	[119]
Myoglobin (Horse Heart)	11.2(±0.7)	12.5(±1.1)	12.4 (±0.9)	11.30	0.1	1.2	1.1	[119]

Table 3.1: Determination of diffusion coefficient ($D_{Est.}$) by CIEF method followed by frequency ($D_{Freq.}$) and time (D_{Time}) domain analysis, $^*(\times 10^7 s/cm^2)$. Data are modelled by a single Gaussian function, in the curve fitting method.

The advantage of FT becomes more pronounced with increasing deviation of observed peak shape from the assumed Gaussian shape. In the following sections the diffusion

pattern of the concentration profiles are graphically demonstrated, in addition to discussion on how well different estimation techniques will perform in measurement of the diffusion coefficient, according to the peak shapes.

3.4.2 Gaussian and Distorted Gaussian Peaks

Due to the self-focusing mechanism of the CIEF mode, the samples are focused in a narrow zone at their iso-electric point. Hence, concentration profiles in CIEF are mostly well described by the Gaussian function. However, in practice, experimental conditions such as wall adsorption, precipitation, nature of the analyte (i.e. charge heterogeneity in antibodies) cause the peak shapes to deviate from the basic Gaussian assumption.

The concentration profiles of myoglobin (Figure 3.2a) and β-lactoglubolin A/B (Figure 3.6) conform fairly well to Gaussian shape. The diffusion path of myoglobin's second isoform was recorded for 30 min and it nearly follows the Gaussian shape assumption at all times. As this meets the assumptions made in the time domain analysis, the diffusion coefficient of myoglobin has been determined with a good agreement to the literature value; nevertheless, a further improvement is obtained through evaluation in the frequency domain. On the other hand, estimation of the diffusion coefficient of β-lactoglubolin is not as accurate as for myoglobin, due to the convolution of the peaks after a short time (Section 3.4.4).

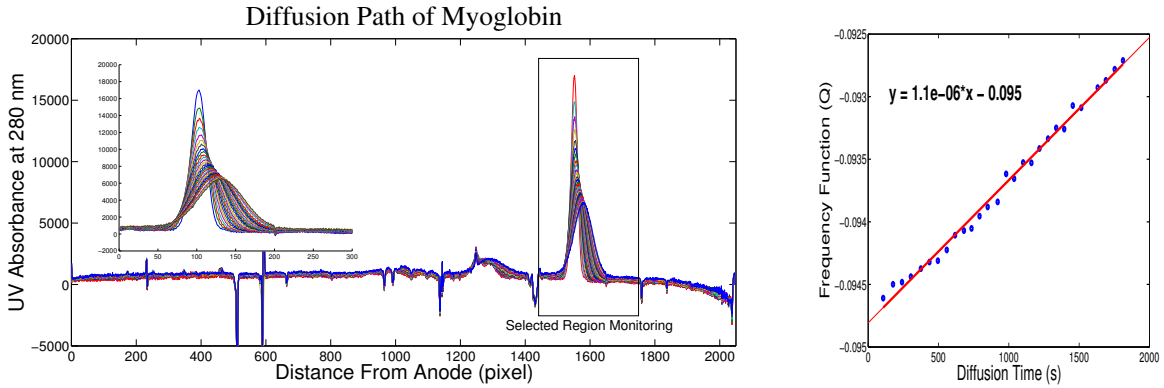

(a) Myoglobin diffusion path (b) Mb D_f

Figure 3.2: Myoglobin's diffusion profile (Gaussian) by CIEF-WCID technique. (a) dynamically monitoring the diffusion of the protein band; (b) measuring the diffusion coefficient by plotting Frequency function, Q, against the diffusion time.

Theoretically, peak broadening should proceed at equal pace in both directions from the center, but experimentally, there are slight influences from the hydrodynamic flow (open capillaries), and sample wall adsorption to be considered. However, this shift in peak positions does not affect the calculations in either the time or the frequency domains. In the frequency domain calculations, only the real part is taken into consideration; hence, the phase variation of the frequency component is ignored.

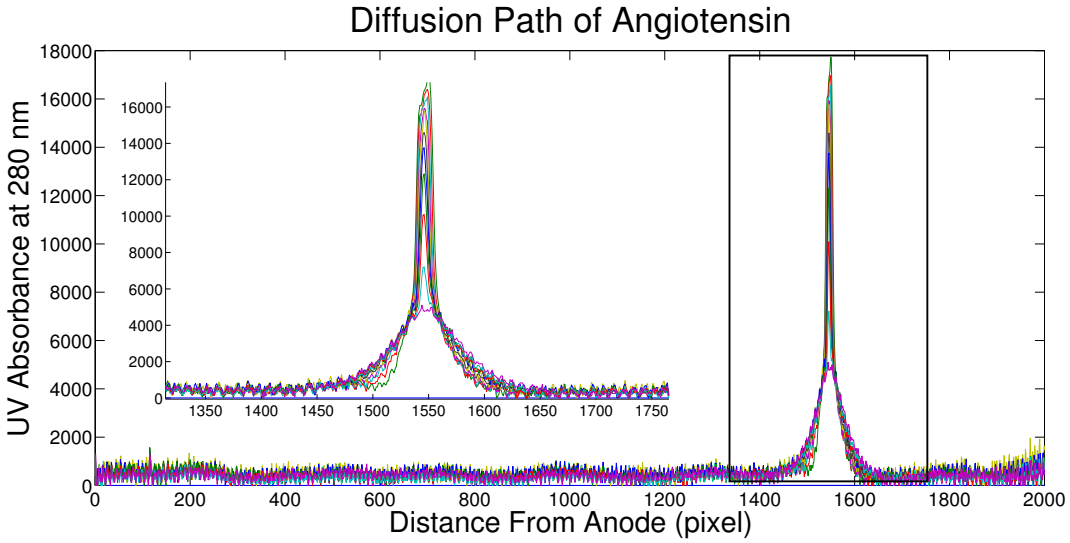

Figure 3.3: Angiotensin's diffusion profile (distorted Gaussian peak shape) by CIEF-WCID technique. The monitored selected region is zoomed in the inset.

Angiotensin's concentration profile resembles a distorted Gaussian shape. As demonstrated in Figure 3.3, the diffusion pattern of angiotensin deviates slightly from the normal distribution, which induces an error in time domain calculations based on the Gaussian shape parameters. The estimated D value with curve fitting method provides more accurate results than the FWHM approach. One of the reasons is the multiplex advantage of the curve fitting method that compensates effect of noise on the estimation, in contrast with the FWHM approach. Employing the FT analysis improves the results considerably even for the signals with Gaussian-like shapes.

3.4.3 Non-Gaussian and Irregular Peaks

The imaging CIEF is capable of characterization and quantitative analysis of recombinant protein charge heterogeneity [120], in which a jagged concentration profile is generated that

makes the estimation of D more challenging via the conventional time domain approaches. In cases such as albumin, the peak shape cannot be defined by a simple mathematical function, therefore the calculations from single Gaussian curve fitting or the full width at half maximum are not applicable any more. As graphically demonstrated in Figure 2.4, CIEF of albumin produces multiple jagged peaks, and fitting a single Gaussian term causes a large error in the calculation of D.

Carbonic anhydrase I (Figure 2.3) is another example of asymmetric irregular distribution in which the Gaussian fit or the full width at half maximum method did not succeed in estimation of the diffusion coefficient, however, the multiple-term Gaussian fit provided a relatively good estimation of D in the time domain calculations. An even better agreement with literature values was again obtained with the FT method.

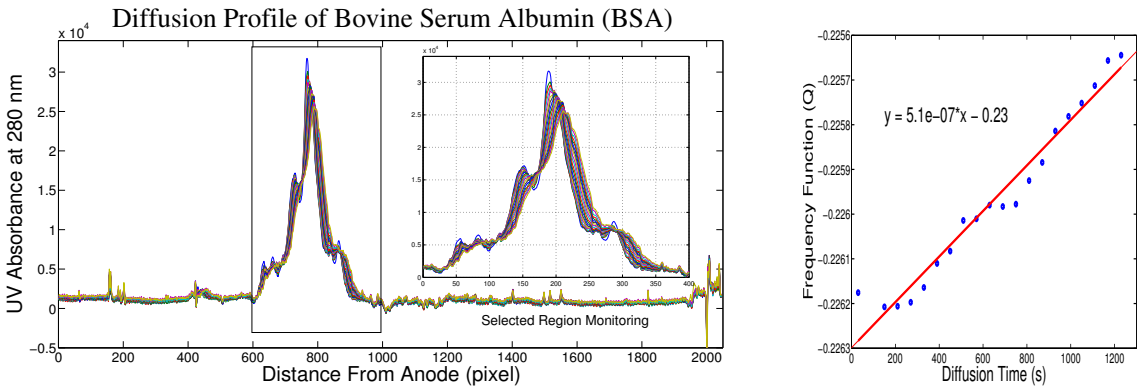

(a) Albumin diffusion path

(b) Albumin D_f

Figure 3.4: Albumin's diffusion profile (non-Gaussian / irregular) by CIEF-WCID technique. (a) dynamically monitoring the diffusion of the protein band; (b) measuring the diffusion coefficient by plotting Frequency function, Q, against the diffusion time.

When using multiple Gaussian terms, the three major coefficients of each term, namely, amplitude, center, and variance, are varied to get the best fit according to the RMSE (Equation 2.3) for peaks that deviate from normal distribution. For a MTG model with a total Gaussian terms of n, the total variance (σ^2) is calculated by:

$$\sigma^2 = \sum_{i=1}^{n} (\mu_i - \bar{\mu}^2) + \sigma_i^2 \tag{3.1}$$

where μ_i and σ_i^2 are the mean and variance of the i^{th} term respectively.

Protein	Gaussian Model		GMT Model		$D_{Lit.}$ [119]
	$D_G(cm^2/s)$	%Error	$D_{MTG}(cm^2/s)$	%Error	
Carbonic Anhydrase I	7.7×10^{-7}	28	11.6×10^{-7}	9	10.7×10^{-7}
Bovine Serum Albumin (BSA)	2.9×10^{-7}	51	7.1×10^{-7}	20	5.90×10^{-7}

Table 3.2: Comparison of the curve fitting results for carbonic anhydrase and BSA irregular peak shapes by Gaussian and multiple-term Gaussian (MTG) Models

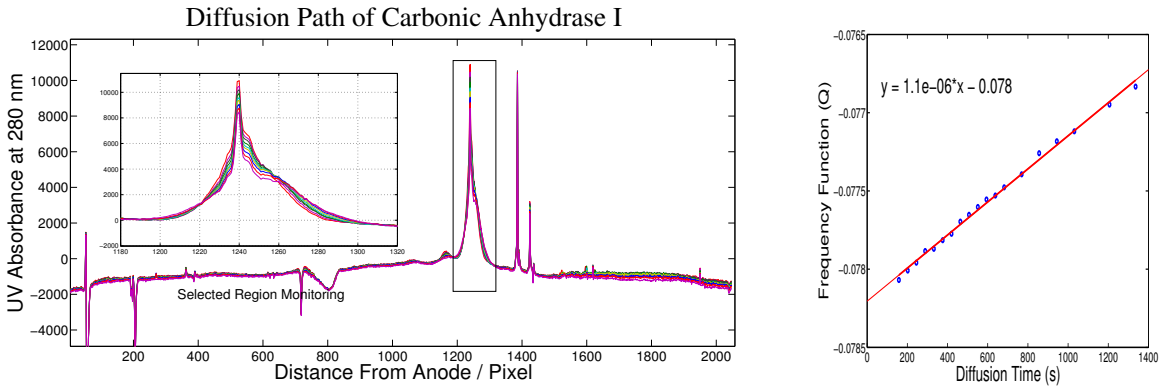

(a) Carbonic anhydrase I diffusion path

(b) CA I D_f

Figure 3.5: Carbonic anhydrase's diffusion profile (irregular peak shape) by CIEF-WCID technique. (a) dynamically monitoring the diffusion of the protein band; (b) measuring the diffusion coefficient by plotting Frequency function, Q, against the diffusion time.

As already discussed (Section 2.2.1), the diffusion coefficient of carbonic anhydrase and bovine serum albumin (Figures 2.3 and 2.4), were estimated by MTG model as examples of signals with irregular peak shapes. They both produced large errors when fitted to a single Gaussian model (Table 3.2). The curve fitting technique, with appropriate model, estimates the diffusion coefficient more precisely compared to the FWHM approach; however, one needs to do additional calculations to obtain the final variance from the Gaussian convoluted model.

In sum, multiple-term model significantly improves the acquired results for non-Gaussian peaks in the time domain. However, the estimated diffusion coefficients from FT method are still providing more accurate results.

3.4.4 Protein Mixture Analysis in Short Time

The use of a modified CE system for the simultaneous measurement of protein diffusion coefficients in mixed samples has previously been demonstrated [121]. However, the current research takes advantage of the iCE280 instrument (equipped with UV-WCID) as a fast, automated, and commercially available tool, which can also provide high resolution of 0.03 pH unit for this purpose [34].

In the capillary isoelectric focusing experiments, components of a mixture are separated and focused on the basis of their pI and form individual sample zones. This high resolving power is an advantage of the CIEF method, that can be exploited for the simultaneous measurement of the components' diffusion coefficients. Experiments on β-lactoglubolin A and B and also myoglobin isoforms (Figures 3.6 and 3.7) illustrate the capability of CIEF coupled with whole column imaging detection for protein mixture analysis.

In the case of β-lactoglubolin mixture, two adjacent peaks are resolved by a very small pI difference (ΔpI=0.2) and combine shortly after diffusion commenced, providing only a short period to record the diffusion process for each individual isoform. The two peaks were so close that they became convoluted after 10 min; therefore, recording the combined peaks for longer periods of time underestimated the D values.

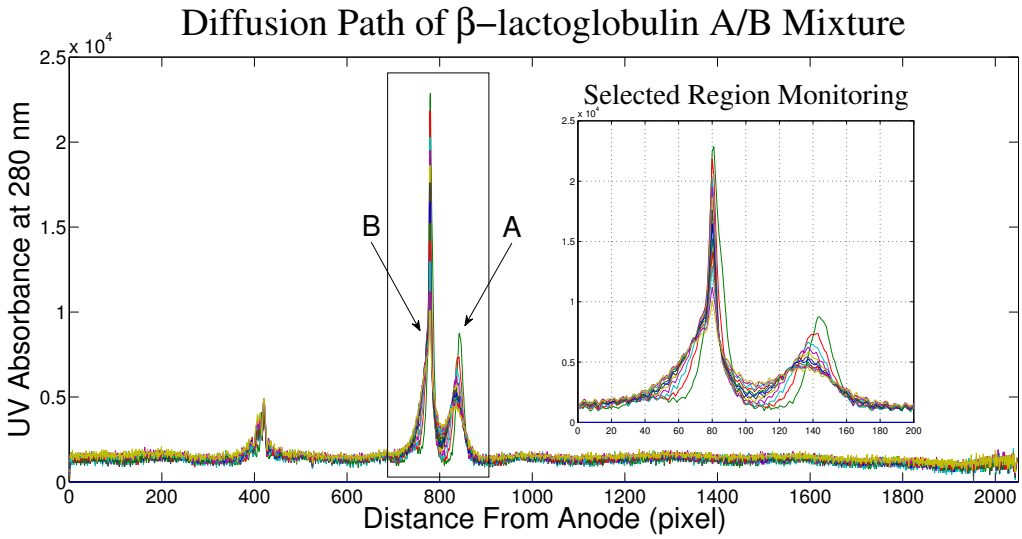

Figure 3.6: Determination of diffusion coefficients of β-lactoglobulin A/B variants from bovine milk, in the frequency domain by CIEF-WCID.

The diffusion coefficients of β-lactoglobulin A and B were determined in triplicates by the FT method in three measurement time periods and the effect of total analysis time is investigated (Table 3.3). The collected raw data became more scattered as the measurement time was increased. The drawback of analysing the closely adjacent peaks is shorter measurement time that deprives from averaging. In general, D will be more accurate as long as the peaks are evaluated separately; as they merged, the analysis became less accurate.

$D_f(\times 10^7 s/cm^2)$	5 min	10 min	25 min	$D_{lit}(\times 10^7 s/cm^2)$	Ref.
β-lactoglubolin A	6.9	7.2	6.2	7.38	[117]
β-lactoglubolin B	4.8	3.5	2.1	3.14	[118]

Table 3.3: Diffusion coefficients of β-lactoglubolin A/B at different diffusion time periods.

The Diffusion path was monitored for 25 min, and the total analysis time required for estimation of β-lactoglubolin A and B variants' D values was determined to be 10 min. Measurements were reproducible with relative standard deviations of 5% and 12%, respectively, and the mean values were accurate within of 3% and 12% of literature values.

3.4.5 Whole Column Imaging Detection of Plug Flow vs. CIEF

The sample concentration profile is influenced by both the experimental technique employed, and the nature of the analyte itself. For instance, in CIEF, the desired analyte was focused in a narrow band, which was defined by a Gaussian function, whereas in iPF, a sample plug was accumulated under the membrane by an electrokinetic injection, producing a boxcar-like profile. In the literature, the diffusion coefficient of the same compound is often reported with different values in accordance with the measuring procedure used. Table 3.4 provides results from iPF and CIEF methods on myoglobin and BSA samples. Since imaging plug flow has the same mechanism as capillary zone electrophoresis, interactions between sample ions will be taken into account for the estimation of D, unlike with CIEF, where the measurements are conducted at a zero net charge.

The change in the sample plug molecular weight reflects in the dispersion rate, and can be monitored by iPF method. In the iPF inset in Figure 3.7, the myoglobin plug contains both isoforms, and the diffusion coefficient is an overall estimation of minor and major isoforms' presence. The diffusion coefficient of the minor isoform of myoglobin was

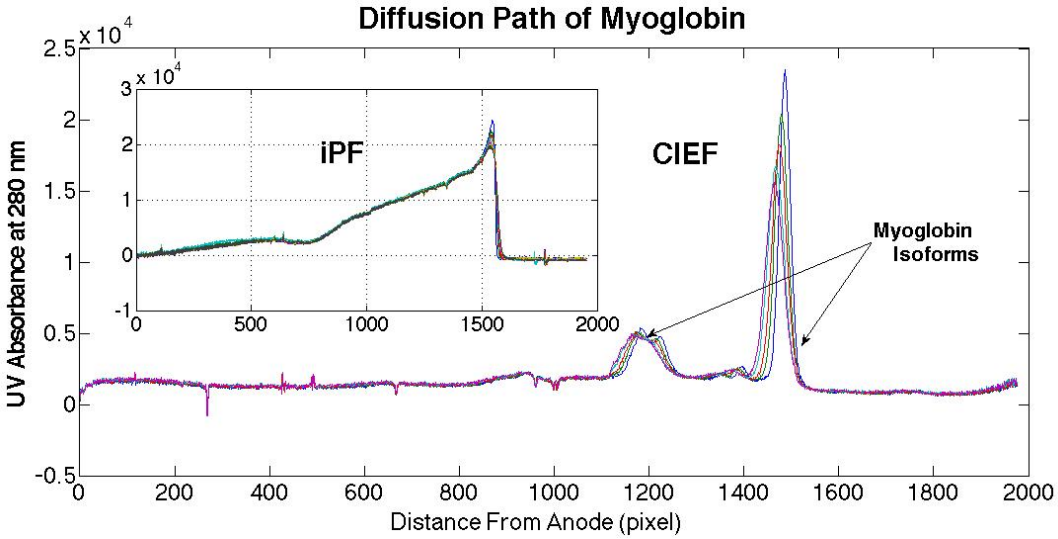

Figure 3.7: Examples of myoglobin iPF and CIEF diffusion profiles. The samples were stacked (3 mg/ml in 25mM buffer) with run buffer 100mM, pH=2.4 at 3kV for 1min, then moved the sample plug by o.5 kV, CIEF: the protein 0.35 mg/ml containing 2% pH gradient 3-10 under voltage gradient 0.5kV for 3min and 3kV for 7min. After moving/focusing step, the electric field is removed and the diffusion pattern is recorded. With passing time, the concentration profiles attenuate and slightly shift toward left.

determined to be $1.6 \times 10^{-6}(cm^2/s)$ by CIEF. The diffusion coefficients associated with the major isoform and overall are presented in Table 3.4. The results from iPF and CIEF show comparable accuracy; however, CIEF shows better precision. The plug flow method was devised for simple and fast measurement of diffusion coefficients at desired pH values. The reproducibility of the iPF results can be improved by modification of the cartridge, e.g. the T-shape injection configuration. It can also and prevent tailing problem.

From a methodological perspective, the plug flow technique has several intrinsic advantages over the CIEF method; for example, iPF eliminates problems associated with CIEF such as precipitation at the isoelectric point (pI) and carrier ampholyte background absorption. In addition, iPF is not limited by the isoelectric point of the species for the applied pH range, which facilitates the selection of a desired pH, e.g. simulating in vivo conditions. It is also considered a relatively faster analysis technique that skips the focusing period, and replaces it with shorter sample stacking and moving times.

In addition, the technique has great potential for miniaturization due to the absence of separation and focusing steps. The commercial cartridge uses a relatively long capillary

Mehod	$D_{BSA}(cm^2/s)$	$D_{Mb}(cm^2/s)$	%RSD		%Error	
			BSA (n=3)	Mb. (n=6)	BSA	Mb.
CIEF	5.1×10^{-7}	1.1×10^{-6}	4	6	13	1
iPF	6.5×10^{-7}	9.1×10^{-7}	13	14	10	–

Table 3.4: Determination of bovine serum albumin (BSA) and myoglobin (Mb.) diffusion coefficients by CIEF and iPF methods, analysed with the FT approach. Experimental conditions were the same as Figure 3.7. The literature values for BSA and myoglobin are 5.90×10^{-7} and 1.13×10^{-6} $\frac{cm^2}{s}$ respectively [119].

window of 5 cm (necessary for the separation and not the diffusion) for whole column imaging detection. However, this range is far more than what is occupied by the diffusing sample during the diffusion process. Modifications to the current cartridge design can make it more suitable for iPF experiments. For instance, further improvement can be obtained to avoid tailing issue by using T-shape valve or cross-injection.

Estimation of The Impurity Level

The imaging plug flow technique can be applied for estimation of the impurity level by resolving the diffusion profile of oligomer mixture into its constituents. In the original pure sample solution we have all the protein in the monomeric form and if it partially aggregates to dimer, trimer, and higher oligomeric states, due to the increase of the molecular weight there would be a change in the diffusion behaviour of the particulates. The final diffusion coefficient profile of such mixture is the overlapped profiles of corresponding oligomers that can be estimated and determined as the impurity level.

There is a general formula that allows acceptable estimation of diffusion coefficient from molecular weight,

$$D = A(T, \eta)M^{-1/3} \tag{3.2}$$

where A is a function of temperature, T, and the viscosity of the medium, η, and M is the molecular mass. Different parameters such as viscosity of the media, temperature, and the shape of the aggregated protein will affect the diffusion profile, however for simplicity of the model we consider all protein forms the same aggregate shape and the other parameters are kept constant. When T and η are kept constant, the linear relationship between $M^{-1/3}$ and D can be used to correlate the diffusion coefficient with the number of subunits. In this study, the polymerization is assumed to be limited to dimerization and therefore the

diffusion profile of one given protein is investigated at two oligomeric states of monomer, D_{mon}, and dimer, D_{dim}. Hence M is the same value and can be represented by number of subunits. The relationship is simplified to

$$D = \frac{K'}{n^{\frac{1}{3}}} \tag{3.3}$$

where K' is a constant and n is the number of subunits. According to Equation 3.3, the relationship between diffusion coefficients of respective oligomers can be calculated, for example $D_{mon} = 2^{\frac{1}{3}} \times D_{dim}$. The initial value for D_{mon} sets to $10^{-6}\frac{cm^2}{s}$, and the diffusion coefficient of dimer is calculated as $D_{dim} = \frac{10^{-6}}{1.26}\ \frac{cm^2}{s}$, which are correlated by the number of their constructing subunits. The diffusion coefficient of the sample plug, D_{mix}, is acquired from convolution of its constituents' diffusion values, in addition to the contribution coefficient of each oligomer that indicates the level of polymerization:

$$D_{mix} = \alpha.D_{mon} + \beta.D_{dim}$$

where α and β are the distribution coefficients of monomer and dimer respectively. Assuming all polymerized species form dimer and higher oligomeric states are negligible; the sample plug contains only monomer and dimer, hence; α+β=1.

Aggregation Level	0%	10%	20%	30%	40%	50%	60%	80%	100%
$\%Error(D_{mon})$	0.0	1.4	4.1	5.9	6.9	7.5	7.9	10.2	10.9
$\%Error(D_{dim})$	0.0	0.9	3.1	4.9	7.1	9.5	12.3	18.9	26.0

Table 3.5: Error percent in estimation of the impurity level in oligomeric solutions with different monomer to dimer ratios. Initial conditions: D_{mon}=$1e^{-6}\frac{cm^2}{s}$; h=0.02 cm; t_0 = 30 s, t_i = 30 s, t_t = 600 s, p=0.001 $\frac{cm}{pix}$, SNR=15.

Protein sample plugs with different ratios of monomer to dimer are simulated and the D_{mix} is estimated by the FT method. Then the estimated D is used to calculate the constituents diffusion coefficients at determined contribution coefficients. Results in the Table 3.5 illustrates that estimation of the diffusion coefficients is more accurate at lower level of dimerization compared to those sample plugs with higher dimeric components. And an increase in the aggregation level of the solution results in more error in estimation of the diffusion coefficient. However, the solution with upto 50% aggregation can be still estimated with error below 10%.

The simulation results reveal that the aggregation of the proteins at the level above one percent dimerization can be detected within 95% of confidence by introducing a sample in

the form of plug (Boxcar function) and less than 1% RSD noise, when the ideal condition is met and there is no truncation error. This application of iPF can be effectively used in quality control where the aggregation needs to be monitored closely.

3.4.6 Stability Study Based on Diffusion Coefficient

The proteins used in this research were mostly supplied in powder form, and they had a long lifespan as long as they were kept in the fridge under recommended storage conditions. However, they need to be prepared fresh as dissolved in the solvent. Proteins tend to aggregate under various conditions, such as high temperatures or unfavourable pH. In the CIEF mode of electrophoresis, the proteins are theoretically prone to undergo 'isoelectric precipitation' when the net protein charge is near zero. However, Majhi et al. proved that measurement at isoelectric point does not necessarily lead to precipitation [122]. They have studied the effect of pH on the aggregation of β-lactoglobulin and observed the maximum aggregation rates in the pH range 4.3-4.8, which is near but below the pI value. Hence the capillary isoelectric focusing can be an appropriate method for the purpose of stability assessment.

In the present research the stability or shelf-life of β-lactoglobulin A and B variants were successfully investigated by monitoring the changes in the diffusion rates in addition to the charge heterogeneities and shift in pI values. The high resolution of CIEF enables it to detect even small alterations of pI. The CIEF data evidenced the aggregate formation in the protein (dissolved in Ultra-pure water) with remaining at room temperature for a period of one month.

Fresh β-lactoglobulin		Old β-lactoglobulin		Ref.	
A	B	A	B	A [117]	B [118]
7.2 ($\pm$0.3)	3.5 ($\pm$0.4)	0.3 ($\pm$0.1)	1.2 ($\pm$0.1)	7.38	3.14

Table 3.6: Comparison of the diffusion coefficient ($\times 10^7 cm^2/s$) of the fresh and one month old β-lactoglobulin variants (n=3) with literature values.

The changes to the electropherogram of β-lactoglobulin are graphically shown in Figure 3.8, and the diffusion coefficients of fresh and one-month old samples were measured and compared to the literature values, presented in Table 3.6. There is a shift in the pI values of both variants, and extra peaks show up in the electropherogram. The protein is fairly stable at room temperature within the first four days, however, it deforms to gel after three weeks.

The observed charge heterogeneity and shift in the peak position can provide information on the aggregate mechanism, in addition to estimation of degradation or aggregation from changes in diffusion coefficient values.

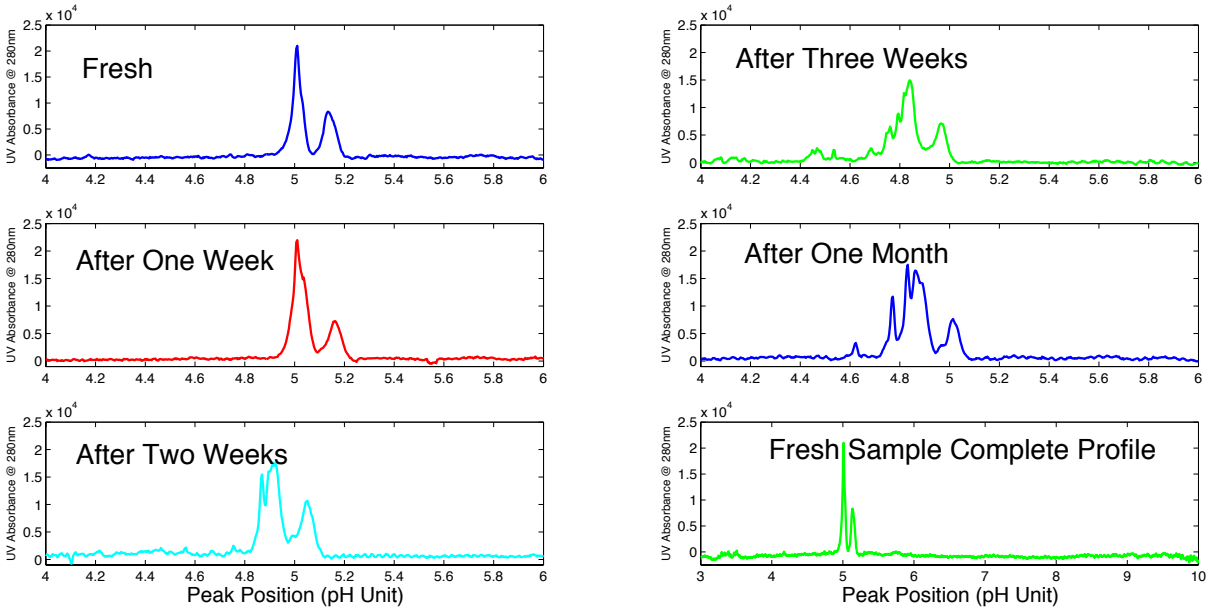

Figure 3.8: Stability assessment of β-lactoglobulin variants by CIEF-WCID during one month. β-lactoglobulin mixture was kept at room temperature

The fresh samples diffusion coefficients measured by the Fourier domain approach are in good agreement with reference values in comparison to the old samples D values, revealing that both variants has changed during time, and isomer A is more significantly altered. Further study of the aggregation can provide valuable information on the association/dissociation mechanisms. Generally due to D alteration one can decide on either aggregation or dissociation. For example the increase in D value can be interpreted as a result of the dissociation that caused the protein falls apart. In this study the old sample D value decreased that proves formation of the aggregate or particulate.

Estimation of the impurity level by resolving the diffusion profile of oligomer mixture can be a useful tool from pharmaceutical viewpoint. However, the diffusive behaviour of the mixture components needs to differ significantly, typically by factor two, in order to be discriminated efficiently. For example, study of monomer-dimer or higher oligomeric states is feasible; the original pure sample solution protein found in the monomeric form, and if it partially aggregates to dimer, trimer, and higher oligomeric states, then a change

in the diffusion coefficient value of the particulates happens due to the molecular weight increase. The diffusion coefficient profile of the mixture is overlapped by profiles of the oligomers. The impurity level can be estimated from deconvolution of the diffusion profile of a mixture of different oligomeric states of the same protein, and the contribution coefficient can be determined accordingly. Thus, the relationship between molecular weight and diffusion coefficient suggests interesting applications for determination of diffusion coefficients by CIEF-WCID in recognition of proteins aggregation, which has great potential to be employed in rapid quality control procedures.

3.5 Summary and Conclusion

Taking advantage of the dynamic imaging detection system, diffusion processes can be monitored in real time fashion and the spatial data carried to the frequency domain for determination of diffusion coefficients. The capillary electrophoresis method in general does not perfectly meet the Gaussian assumption. The concept of shape independent feature of the FT approach has been explored, and the experimental results prove that, unlike analysis that is carried out in the time domain, the FT approach is not restricted by any peak shape assumption. However, the efficiency varies according to the frequency content of each function. Analysis in the frequency domain is realised to empower the CIEF, for measuring the diffusion coefficient.

Although CIEF is known as an effective way to get the most out of the diffusion data, there are still a few obstacles, such as the risk of protein precipitation at the isoelectric point where the proteins net charge is zero and there is no electrostatic repulsion. The iPF method is introduced as an alternative method for measuring the diffusion coefficient. It is a fast simple method, which results in non-Gaussian shape signals. The fast Fourier transformation as a more general approach assists data processing of signals that deviate from Gaussian shape. Irregular peak shapes were processed by Fourier analysis where the traditional methods failed. Analysis of the CIEF and iPF results in the frequency domain compared to the time domain provides more precise and accurate determination of diffusion coefficients, which reinforced the FT method's efficiency.

Capillary isoelectric focusing with whole column imaging detection can be used in food and pharmaceutical industries as a cost-effective and fast tool for studies on protein aggregation as part of quality control. It is an automated way for recording the diffusion process and rapid recognition of protein degradation or association by monitoring the changes in their diffusion rate. The diffusion coefficient measurement can be used for molecular weight determination and stability assessment.

Chapter 4

High Throughput Chip-Based Electrophoresis with Schlieren Imaging Detection

4.1 Introduction

Schlieren optics provides a powerful technique for visualizing changes or non-uniformities in the refractive index of transparent media. It has been used for over two centuries, since the early 1800s. Schlieren systems have been typically implemented for a wide variety of real-time fluid dynamics studies [123]. Widespread availability of digital imaging systems allows Schlieren optics to be applied to the study of transparent media in novel ways. Application of Schlieren detection in analytical chemistry has been reviewed in Reference [23], and previous papers on all modes of capillary electrophoresis coupled with Schlieren detection are summarized in Table 1.1.

The whole channel imaging detection technique empowers the capillary electrophoresis in many aspects. However, a remaining limitation is that only one sample can be processed at a time. The sample throughput is improved by extending the technology to a multi-channel system, using a prototype linear multi-channel chip. The properties of the chip, such as good optical transparency, chemical resistance, and high temperature stability, make it a suitable choice for robust, sensitive, and reproducible electrophoresis analysis with both UV-absorbance and universal concentration gradient detection.

To the best of our knowledge, all previous studies on capillary electrophoresis with

Schlieren detection have been performed inside round or square capillaries [39]. This research provides analysis in a chip-based device containing multiple-channels with different dimensions, including a discussion on the effects of geometry and the dimension of the channel as the detection cell on the measurements. Two principal modes of capillary electrophoresis, CIEF and MBE, were employed to evaluate the chip performance and demonstrate the use of the Schlieren detection in high-throughput analysis.

This chapter presents background of the technique, describes the methodology behind the system, offers a mathematical exposition of the principles of Schlieren optics along with the design of a basic Schlieren system, and its application to the diffusion coefficient measurement. The application of concentration gradient detection to the determination of diffusion coefficients has been already performed; however, its quantitative analysis is not that robust, and depends on conventional peak height measurements [26]. The present study explores the data analysis of Schlieren images, by calculating the diffusion coefficient in the frequency domain. The Fourier transformation approach is the same as what has been employed for analysis of the diffusion data from capillary isoelectric focusing with whole column imaging detection [87].

4.2 Theory

Snell's law can describe the physical basis for Schlieren imaging, in which light rays undergo refraction and deflection from their continuous path, when disturbed by inhomogeneous media, such as the concentration gradient in the fluid. The law states that light slows down as a result of interaction with matter. In homogeneous media, such as vacuum, light travels uniformly at a constant velocity. Schlieren flow visualization is based on the deflection of light due to a refractive index gradient. As shown in Figure 4.1, the un-deflected light is focused at the focal point of the lens where a black spot, *Stop*, blocks the incoming rays. The index gradient causes the light deflection toward higher refractive index, which produces an image depending upon the deflection angle. This approach is called dark-field technique, when all non-deflected light is blocked by the Stop and only deflected light reaches the image plane. The light intensity recorded by the camera is proportional to the non-uniformity of the medium, that is, to the gradient of the refractive index.

The design of a Schlieren system requires a compromise between sensitivity, image resolution, and the size of the field-of-view. The required sensitivity should thus be estimated at the outset by considering the possible range of refractions of the Schlieren objects to be examined [124]. With larger capillaries, detection by absorbance tends to be more sensi-

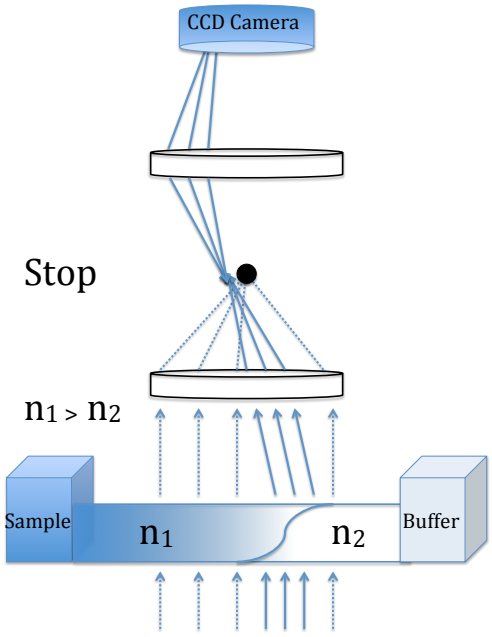

Figure 4.1: Principle of the Schlieren technique through ray-tracing diagram.

tive than Schlieren detection. However, with narrow capillaries, Schlieren detection can be more sensitive, particularly when combined with a laser light source [125].

4.2.1 Light Propagation

The light-material interaction within transparent media is governed by the refractive index. The non-uniform distribution of analytes for a concentration gradient provides a corresponding refractive index gradient. Figure 4.2 illustrates the physical principle of light propagation. The light propagates along z-direction. Assuming a negative vertical refractive-index gradient solely in the y-direction ($\frac{\partial n}{\partial y} < 0$); after propagating through a Schlieren object, the vertical planar light wave-front becomes displaced, and each section experiences different refractive indexes.

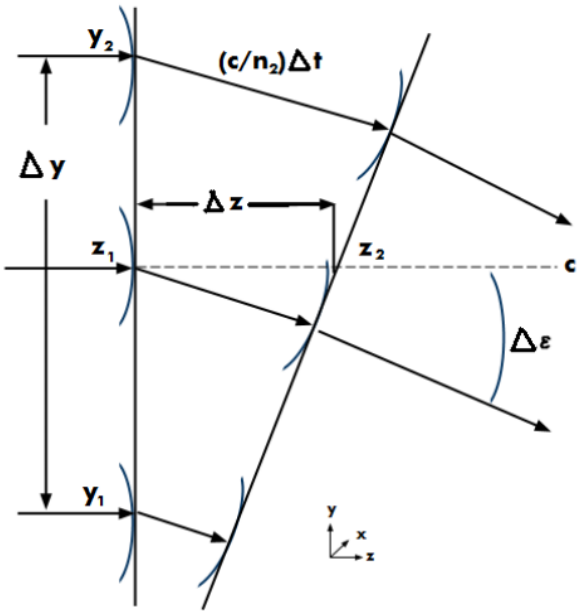

Figure 4.2: Diagram of light propagation due to the refractive-index gradient [126].

If a ray of light covers a distance Δz in a time interval Δt, it is refracted by an angle $\Delta\varepsilon$. Δt is governed by the refractive index n, defined by $n = \frac{c}{v}$, where c is the speed of light in a vacuum, and v is the local speed of light. The differential time can be expressed by $\Delta t = \Delta z \frac{n}{c}$; then one can write:

$$\Delta\varepsilon = \frac{(\frac{c}{n_2} - \frac{c}{n_1})}{\partial y}\partial t = \frac{n}{n_1 n_2}\frac{(n_1 - n_2)}{\partial y}\partial z \tag{4.1}$$

This can be simplified by letting all finite differences approaching zero and simplifying $\frac{n}{n_1 n_2}$, which gives

$$\frac{d\varepsilon}{dz} = \frac{1}{n}\frac{dn}{dy} \tag{4.2}$$

If we use small angle approximation to postulate $d\varepsilon$ is equal to $\frac{dy}{dz}$, we obtain

$$\frac{\partial^2 y}{\partial^2 z} = \frac{1}{n}\frac{\partial n}{\partial y} \tag{4.3}$$

The refractive index n does not cause ray deflection, but the gradient of this refractive index $\frac{\partial n}{\partial y}$, as declared by Equation 4.3. Schlieren images can be found by integrating the ray curvature of light rays in optical inhomogeneities in the appropriate directions, and relating the curvature of a refracted ray to the magnitude of the refractive-index gradient:

$$\Delta\varepsilon_y = \frac{1}{n}\int \frac{\partial n}{\partial y}\,\partial z. \tag{4.4}$$

Equations 4.3 and 4.4 show the direction of the light ray deflections, which bend towards regions of higher refractive indexes.

Deflection Angle and Column Dimension Relationship

Fermat's principle states that light takes the path by which it traverses the medium in the shortest possible time. A quantitative relationship between the total deflection angle (ε) and the separation column dimension (L), can be derived on the basis of this principle. In most practical analytical cases, where L and ε are small; ε can be approximated by:

$$\Delta\varepsilon = \frac{\Delta l}{n}\frac{dn}{dx} = \frac{\Delta l}{n}\frac{dn}{dC}\times\frac{dC}{dx} \tag{4.5}$$

hence,

$$\varepsilon = \int_0^L \frac{1}{n}\frac{dn}{dC}\frac{\partial C(l,x)}{\partial x}\,\mathrm{d}l. \tag{4.6}$$

The exact relationship between the concentration of the analyte in the medium and the refractive index ($\frac{dn}{dC}$) can be experimentally measured. The integral along L should be calculated, if the concentration gradient along the path is not constant.

4.2.2 Sensitivity of Detection Method

As discussed in Section 1.2.1, the analytical signals can represent either the average or the gradient of the analytes' concentration in the detection volume.

Sensitivity of Concentration Average vs. Gradient

The signals of moving boundary electrophoresis and isoelectric focusing resemble sigmoid and Gaussian functions, respectively, when the average concentration (C) detection method is used; however, Schlieren detector produces a signal that corresponds to the derivative of the signal ($\frac{dC}{dx}$) produced by e.g. an absorbance detector. Calculating the maximum value of the signal for either method, the ratio of the C_{max} to $(\frac{dC}{dx})_{max}$ provides a constant B_0, which is inversely proportional to the standard deviation [23].

$$(\frac{dC}{dx})_{max} = \frac{e^{-1/2}}{\sigma^2(2\pi)^{1/2}Fv}M = \frac{e^{-1/2}}{\sigma v}C_{max} = B_0 C_{max} \tag{4.7}$$

where v is the linear flow rate, M is the total mass injected, F is the flow rate, and σ is the standard deviation of the distribution. Consequently, a detector with a linear response to the concentration will yield a signal proportional to the mass of all sample constituents. An improvement in sensitivity is anticipated with an efficiency improvement. Gradient detection becomes more efficient with decrease σ, that is, with smaller dispersion of the sample plug.

The sensitivity is also affected by the employed optical system; it is proportional to the focal length of the collecting lens and inversely proportional to the Stop size. Thus, high sensitivity needs a small blocking Stop and lens with large focal length [127].

4.2.3 Lens Effect in Capillaries

As its name reveals, capillary electrophoresis is primarily performed inside capillary tubes. In detection methods that depend on light path-length, e.g. UV absorbance and Schlieren imaging detection, the lens effect is an important issue associated with round capillaries. The curvature of the round capillaries acts as a thick cylindrical lens with a short focal length, which bends the collimated incoming beams. Thus, the outgoing beam becomes strongly uncollimated, which can ruin light collection, unless extra light focusing elements are employed. This drawback can be addressed by using microchips with a rectangular channel. Liu et al. experimentally confirmed a higher intensity of the light beam after passing a micro-chip channel compared to a round capillary [128].

4.3 Experimental Implementation

A laser Schlieren system was constructed (Figure 4.3) for monitoring the protein moving boundary electrophoresis experiments in the multi-channel chip.

4.3.1 Schlieren Set-up

The system was mounted on a vibration isolation table. All optical elements and posts were bought from ThorLabs, USA. The components were arranged as outlined in Figure 4.3, and fine adjustments were precisely performed. The light was accurately focused so as to avoid aberrations (Section 4.5.3) and misalignment of the optical components, and each of the components was carefully aligned to pass the light without interferences or distortion. After optimization of the positions and appropriate alignment, the system was rotated to the vertical configuration (Figure 4.3).

The system implemented a beam-expander lens to expand the green laser (532 nm, power $\leq$5 mW) beam to a 5cm-diameter light spot, and was equipped with filters and a pinhole to adjust to a desired spot diameter and lower the power. The collimated light traversed another lens (L_1) to reach the test area, where the chip was located. Depending on the experiment, the light was deflected by or straightly passed through the Schlieren lens (L_2); those rays that were not deflected would focus at the Stop and were blocked there, while the rays that were deflected by the sample inside the channel changed their path and reached the camera. The deflected beams were focused and hit the sensor via the image transfer lens (L_3).

Light Source and Optical Elements

Images were captured by a CCD camera. Lenses 1 and 2 were 5-cm-diameter, with 7.5-cm and 2.5-cm focal lengths, respectively. The third lens was a 2.5-cm-diameter planoconvex lens that converged the beams passing through the Stop plate on the CCD sensor. The specific characteristics of laser, such as its monochromaticity, intensity, and coherence, make it a proper choice for this study. However, the light intensity of the laser beam is at its maximum in the middle, and decreasing as it gets further from the center, which results in a Gaussian distribution. This inhomogeneity in the beam spot profile was corrected by putting a mechanical aperture in front of the light source, in order to selectively pick from the center of the beam spot. Additionally, a graded neutral density filter was used to minimize inhomogeneity, and the intensity was attenuated by using filters to avoid camera

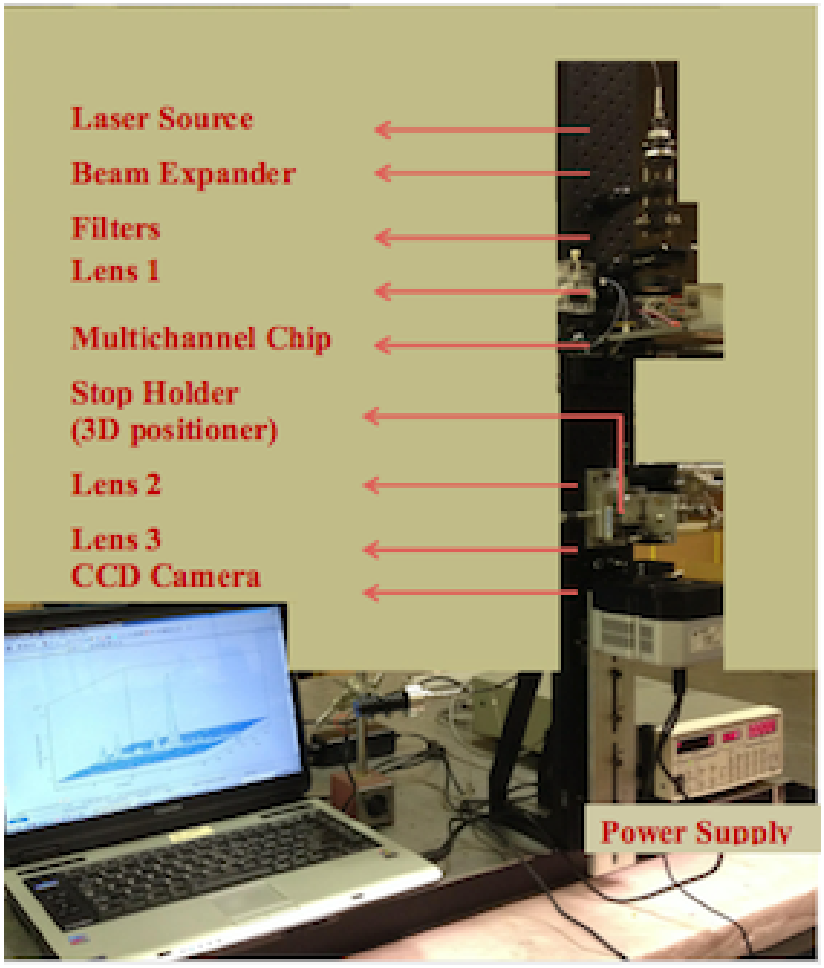

(a) Schlieren Set-up

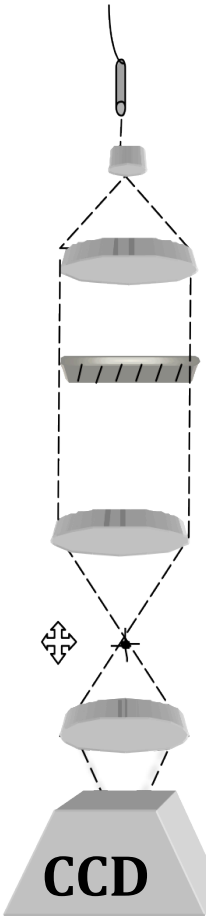

(b) Ray Path

Figure 4.3: The Schlieren set-up, and the ray traverse path: The laser beams were expanded and illuminated on the multi-channel chip in the test area, then blocked by the Stop from reaching the camera. As the light deflected from its focal point by changes in the concentration, the beams hit the CCD sensor.

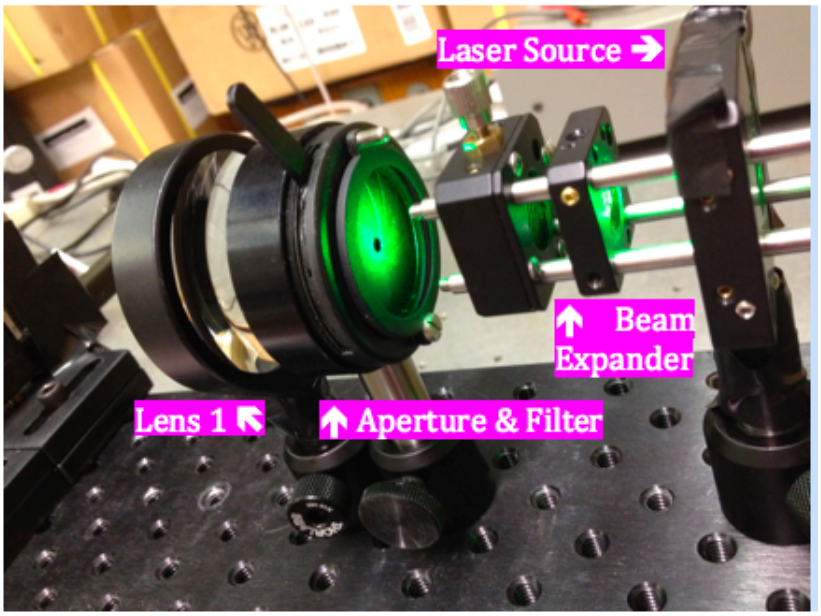

Figure 4.4: Laser source and the modifying elements: beam expander, aperture, and filter

saturation (Figure 4.4). The laser beam was first expanded to a 5-cm-diameter spot; this allowed covering the view field of the camera, which is illumination of the laser to five channels at the time. As shown in Figure 4.5, the channels experienced different light intensities, according to their position in the laser beam spot.

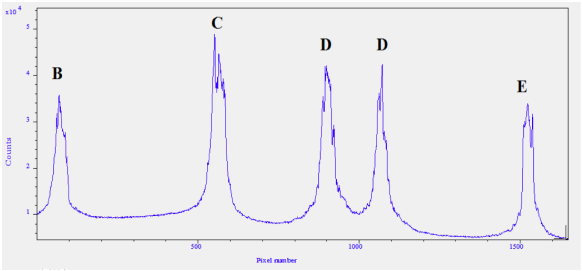

(a) Full vertical binned (FVB) readout of the channels

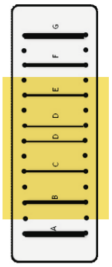

(b) Laser beam spot

Figure 4.5: Field of view for the current Schlieren set-up

For example, in channel B, despite having largest width and depth compared to the other 4 channels (Figure 4.8), lower peak heights and widths were observed. In order to minimize the inconsistencies caused by this situation, the experimental region was limited

to the center of the light spot. The mechanical aperture provides illumination to the desired channel/channels by adjusting the pin hole size.

Test Area

The test region was delimited by the space between L_1 and L_2, where the multi-channel chip was loaded on a 2D-stage (Figure 4.6). The chip was held firmly in place after putting the desired channels in the center of the light beam by tilting the slide in xy-direction.

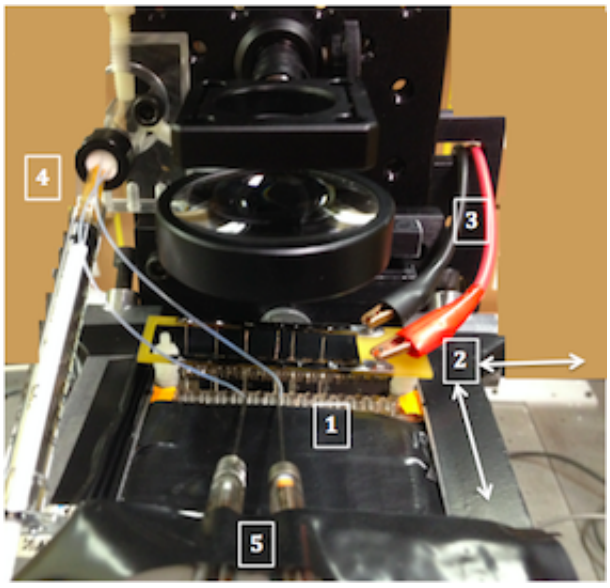

Figure 4.6: Multi-channel chip in Schlieren test area: (1) the chip with electrode comb (2) x,y-axis 2D adjustment (3) connectors to the high power supply (4) plastic tube to remove the electrolyte by vacuum (5) micro-syringes for sample introduction.

After adjusting the chip into the right position, the electrode comb was mounted on its top, and the electrodes were connected to the high power supply through alligator connectors. Plastic tubing was inserted into the sample reservoir to remove electrolyte by a vacuum generated inside the vial, which was accomplished by withdrawing the syringe plunger. The micro-syringe for sample introduction was already filled with a known volume of the sample (15-20μL), and were used to refill the reservoir after the electrolyte was evacuated.

4.3.2 Chip Specifications and Configurations

In the current study, a prototype multi-channel chip in a miniaturized cyclic olefin copolymer (COC) microfluidic device (thinXXS Micro-technology, Germany) was employed for protein analysis. The short channels, 18 mm, of the introduced chip were embedded in a slide with a footprint of 7.5×2.5 (cm^2). The cyclo-olefin copolymer combines excellent optical properties with bio-compatibility and good chemical resistance to most acids and bases. The linear channel slide features 5 straight channels of different cross sectional areas (Figure 4.8). Basically the chip comprises three layers, and an additional photo-mask layer was attached at the bottom:

- Top layer: a rigid polymer containing electrolyte reservoir and through holes between the electrolyte reservoirs and separation channel, with slide standard ports
- Middle & bottom layers: parallel separation channels, and a rigid polymer foundation
- Photo-mask layer: black glass sheet with slits aligned with the channels

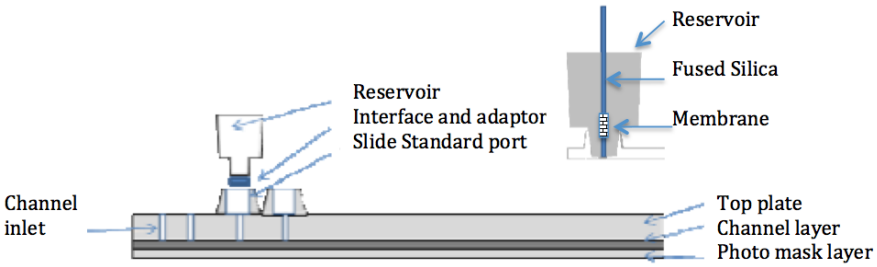

Figure 4.7: The prototype COC slide layout, and modifications for CE experiments

In contrast to the conventional metal slit that is used in commercial capillary cartridges to avoid stray light, which is expensive and tedious to align in the case of multiple capillaries, the photo-mask layer boasts the inherent advantage of aligning the slit layer to parallel channels in one step. The pattern of the slide is plotted by AutoCAD software and printed as a photo-mask by the Front Range Photo Mask Company in USA. This layer was aligned with channels and attached to the bottom of the slide, using epoxy glue, under the microscope. The ease of this one-step multiple alignment, together with the lower cost of purchase in comparison to the metal slit for UV-detection method, are worthy of note.

As shown in the general schematic of the slide in Figure 4.7, two different configurations were used for the MBE and CIEF experiments. The standard ports with a capacity of 25

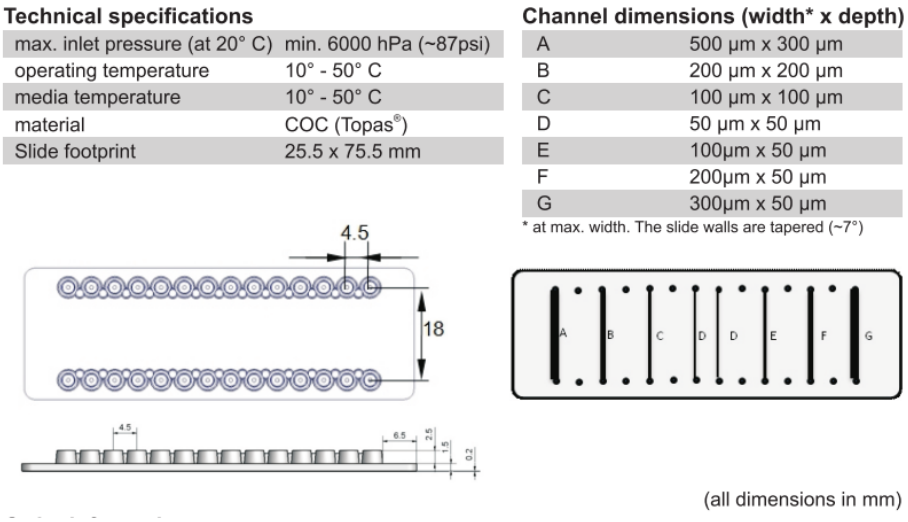

Figure 4.8: Technical specifications and configuration of the linear channel slide provided by the manufacturer (thinXXS Micro-technology, Germany)

μL were used as reservoirs in the MBE experiment, while micro-pipette tips were cut and mounted on top of the standard port by means of an interface and adaptor, functioning as 200μL-capacity reservoirs in the CIEF experiment. The different configurations of the chip for each mode of electrophoresis are explained in detail in the following sections.

Single Channel Setup for CIEF Experiments

The single channel experiments ran in channel C, which has comparable dimensions and surface-to-volume ratio to the capillary in the commercial cartridge (Table 4.2). To perform the CIEF experiment, larger reservoirs, injection capillaries, and membranes were incorporated into the prototyped chip. The slide was coupled with UV-WCID in the commercial iCE280 instrument, and cut in a way that allowed the channel to align to the center of the detector, with the position becoming fixed by screwing the two drilled holes on the slide. The metal slit surrounded the channel to adapt the chip for UV detection. The Pt electrodes of the instrument were also replaced with longer ones to reach the newly designed reservoirs.

A membrane was needed to facilitate the electrolyte ion passage. The membrane was provided in the form of a nitrocellulose hollow fiber, which was inserted between two pieces of fused silica capillary. The shorter capillary piece, in contact with the channel port, was 6

mm long that comprised the connector fused silica capillaries on either side of the channel to the 18 mm long channel, making a separation column 3 cm long in total, with a 1.8 cm effective length of channel as the detection window. Using a standard thinXXS Adaptor that was drilled by the machine shop at University of Waterloo to accommodate a fused silica capillary, this adapter was mechanically joined with the COC slide. As shown in Figure 4.9, a micropipette tip of 100μL capacity was glued on top of the standard port. A metal slit of 100μm-wide was aligned to channel C to stop stray light.

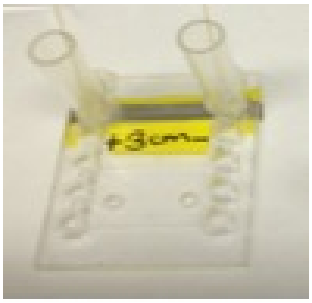

Figure 4.9: The chip configuration used for CIEF experiment

The capillary-to-chip interface was important from the viewpoint of the dead volume, which affected the reproducibility and proper formation of the pH gradient. Using the connector directly to the inlet result in an empty space, which was modified in order to avoid dead-volume- associated issues. The interface was a connector, which was manipulated utilizing an attached micro-pipette tapered tip, providing a modified sealed connection to minimize dead volume issues.

Multi-channel Set-up for MBE High Throughput Analysis

The COC-chip design, with its short channels and integrated reservoirs, suggests a simple configuration for robust analysis, with moving boundary electrophoresis, replacing the photo-mask sheet with the metal slit to avoid individual alignment of the slit to the channels. The COC-slide was made of transparent plastic, with holes drilled on top to make the fluidic connection, and a standard port with a capacity of 25 μL to accommodate the reservoirs. This configuration of the slide was appropriate for moving boundary electrophoresis and did not need further modifications. However, additional components were needed for the multi-channel set-up.

For the multi-channel to function, an electric field needs to be generated through each channel. This was achieved using an electrode comb, which distributes the voltage to

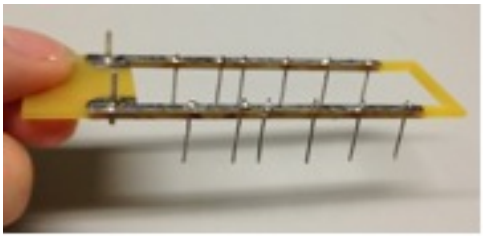

(a) Electrode comb

(b) Multi-channel Set-up

Figure 4.10: The multi-channel set-up for CIEF experiment

each channel through a separate electrode pair. The electrodes were connected to the high power supply through terminal pins (Figure 4.10a). The electrode holder resembled a frame around the slide and did not cover the detection region. There were two pins at the end of each electrode row to connect to the power supply. The photo-mask sheet was aligned to the channels and faced the laser source.

4.4 Methods And Materials

The microfluidic chip was employed for quantitative analysis of the proteins by capillary isoelectric focusing and moving boundary electrophoresis, coupled with UV and Schlieren imaging detection, respectively. In addition, corrections to the Schlieren image improved the quantitative analysis.

All chemicals were of analytical-reagent grade, and purchased from Sigma Aldrich, except where other suppliers are mentioned. The solutions were prepared using sonicated Utrapure water (18MΩ) from a Barnstead/Thermolyne system. The samples were filtered with a 0.2μm pore-size membrane.

4.4.1 CE Techniques

The multi-channel chip was primarily tested with capillary isoelectric focusing for separation of myoglobin isoforms with UV-WCID detection inside a single channel. Further experiments were performed by moving boundary electrophoresis mode, and the signal was detected by Schlieren optics inside multiple channels. With both separation techniques, diffusion coefficients were estimated in two modes that can be described as static and dynamic, respectively, depending on the fluid motion at the time of diffusion measurement.

Capillary Isoelectric Focusing; Static Mode

Imaged capillary isoelectric focusing was performed on an iCE280 Analyzer (Convergent Bioscience [now Protein Simple], Toronto, Canada), inside a commercial separation cartridge. The effective separation path length was 5 cm in the capillary, and 3 cm in the channel. The capillary dimension was 100 μm ID, and 200 μm OD with fluorocarbon internal coating. Channel C was a square duct with a 100 μm width.

Sodium hydroxide (100 mM) and phosphoric acid (100 mM) were used as the catholyte and anolyte, respectively. The sample mixture contains a 0.5 $\frac{mg}{ml}$ myoglobin, 0.35% $\frac{w}{v}$ methyl-cellulose, 2% $\frac{v}{v}$ Pharmalyte 3-10 and 6-8. The focusing was performed at 1.5 kV for 2 min , followed by 3 kV until it reached a stable focusing, which often took less than 10 min in total.

In this mode, the sample components are separated based on their isoelectric points and the diffusion process is recorded statically, that is, in the absence of an electric field or any other driving force.

Moving Boundary Electrophoresis; Dynamic Mode

The sample was introduced by emptying and then filling the reservoir at the anodic end with a sample solution. This step was accomplished using injection syringes and a small-diameter plastic tube to evacuate the anodic reservoir. The sample boundary was driven by applying a 500 V potential difference from a high-voltage d.c. power supply (Stanford Research Systems, INC. Model PS350). The empty/fill mechanism is depicted in Figure 4.6. The whole system was mounted in the testing region of the Schlieren set-up. All samples were dissolved in buffers before use. Tryptophan 1 $\frac{mg}{ml}$ in borate buffer (50 mM , pH 10), and BSA 1 $\frac{mg}{ml}$ in phosphate buffer (40 mM , pH 2.5), were used as samples.

Basically, no separation happens in this mode and the dispersion of the moving front is dynamically recorded to estimate the molecular diffusion coefficient. First, each reservoir and the desired channels were filled with buffer. The channels were inspected under the microscope to ensure they were completely filled with the buffer and that no air bubbles were present prior to mounting the chip onto the testing region of the Schlieren system. It is important to note that this is an essential step; if an air bubble exists in the system, the electric field will disconnect, and a shiny fixed point will be observed during the run time.

Internal Coating Techniques. The capillary cartridge was conditioned with 0.5% $\frac{w}{v}$ methyl-cellulose solution to minimize the EOF, whereas the polymeric channels on the chip

were merely flushed with water between runs. Protein adsorption to the channel walls was investigated with this chip, showing negligible wall interaction. Due to their hydrophobic nature, plastic microchips, especially COC chips, have very low EOF rates. Since the COC linear channel is resistant to a wide range of polar solvents and molecules, it is almost inert, avoiding electroosmotic flow. However, the EOF is not necessarily zero. Having negligible wall interaction, the polymeric chip is suitable for performing IEF without conditioning the column. In addition, the methyl-cellulose in the sample solution also acts as a dynamic coating.

4.4.2 Analysis of The Schlieren Images

The employed CCD camera (Model: DR32400-FI, Andor, USA) is a silicon-based semiconductor chip bearing a two-dimensional matrix of photo-sensors, or pixels. This matrix has a pixel array of 1650 $\times$ 200, for an imaging area of 26.4 mm $\times$ 3.2 mm, and a pixel size of 16 $\times$ 16 μm^2. The pixels are arranged in perpendicular rows and columns. Fast-scan CCDs are used in video cameras to capture moving images. Solis proprietary software was used to control the camera and analyze the time-resolved imaging efficient data acquisition and processing. AndorBasic, as a built-in programming language, was used to manipulate data.

Full resolution image readout mode provided a 3D-image of 1650 $\times$ 200 pixels, and the z-direction showed the amplitude of the signal, which was determined by the intensity of the deflected light that reached the camera sensor. With the selected optical elements, the CCD could monitor the effective length of 3.5 cm that covered 5 channels (Figure 4.5). According to the sensor's dimensions, the view field of the camera can cover the whole 18 mm of channel length. However to minimize the effect of uneven distribution of the laser light, it was restricted to partial channel imaging detection by the width of the sensor at the center of the beam spot for simultaneous monitoring of two channels.

Data Acquisition

The chip was introduced to the system, and the camera was moved in the z-direction (up and down) to focus its lens on the chip. Test photos were taken to ensure proper exposure of the channels prior to introducing the Stop. The next step involved putting the collecting lens in focus, where all outgoing rays from the testing area focused at the camera. Then, the Stop was adjusted in order to block the whole background light. The Stop was mounted onto a 3D-translation block that allowed fine adjustments along three axes so as to align it precisely with the focal point of the Schlieren lens.

The CCD camera can acquire a complete scan in microseconds, which allows for rapid kinetic measurements. The kinetic cycle time determines the frame rate at which the camera is operating. Depending on the acquisition parameters, such as vertical shift speed, binning or sub-image patterns, cycle time, and trigger mode, the frequency of the acquired data is determined. In the present study, full resolution image readout mode was used with an internal trigger. The kinetics acquisition mode was employed to record the dynamic process; this mode is particularly well suited to recording the temporal evolution of a process such as diffusion.

Exposure Time. The contrast between the background light and the empty channels is enhanced as the exposure time is increased; on the other hand, exposure must be limited to ensure that none of the pixels in the CCD camera become saturated. Under our conditions, this was achieved using sub-second exposure times (Figure 4.11). However, one should ensure that saturation is avoided in the intensity profiles by varying the exposure time. Short exposure time, in the case of high power light sources with appropriate filters, can decrease the scanning probe problem, which is discussed in the data treatment section. The amplitude of the photons detected in an image was obtained by subtracting the total photon count of the background image from each image frame in the kinetic series, and displayed as background corrected count unit.

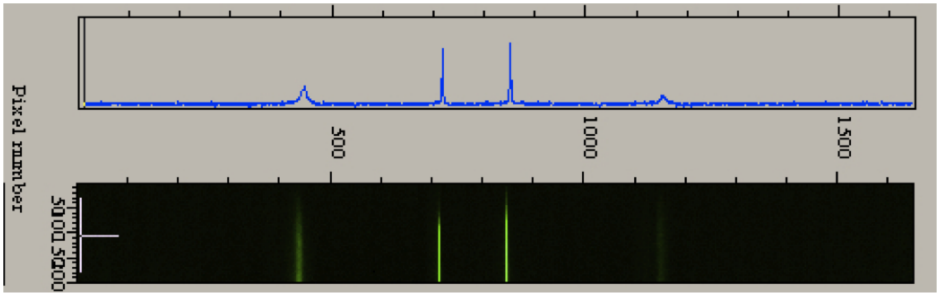

Figure 4.11: The intensity profile; laser source power $\leq 5mW$, exposure time: 0.1 sec.

Movies were obtained by sequential display of the frames recorded at specific intervals. The minimum time required for an acquisition depends on a number of factors, including the exposure time, number of accumulations, kinetic series length, and the kinetic cycle time. These parameters were defined and set to the following values for all MBE/Schlieren experiments in this section:

- Exposure time: the time interval during which the camera collects light for a single scan (Set to 0.1 sec).

- Number of accumulation: the number of scans that are added (or averaged) to produce a single frame of the processed data series (Set to 3).
- Kinetic series length: the number of frames in the entire data series (Set to 100-150).
- Kinetic cycle time: the time interval between the frames (Equal to 1 sec.).

Several scans were involved in a complete data acquisition. The data was collected in a kinetic series with 100 scans; each scan consisted of three accumulations with 0.3 sec cycle, hence the frequency of 0.98 Hz was obtained, which equals to 1 frame per second.

Data Treatment

To enhance the quality of the images, signals were processed through background correction, normalization, and noise reduction. Without these corrections, the images included additional noise and baseline fluctuations, which would have made the quantitative analysis difficult.

Ambient Light and Beam Intensity Fluctuations. Ideally, measurements should be performed in a dark room, where no other source of light except the laser source is present; however this condition cannot often be met, and ambient light leakage needs to be corrected. On the other hand, fluctuations in the illumination source can lead to fluctuations in signal levels. Thus, it is necessary to normalize the data so that its value remains stable from frame to frame.

Manipulation of the data was performed using the Andor BASIC programming language included with SOLIS. The default data type is Counts. Background is a data acquisition made in darkness. It is made up of fixed pattern noise, and any signal due to dark current. Correction for the background Count, also improves the signal-to-noise ratio of the image.

The calculations for the various data types assume the following definitions:

- **Signal:** uncorrected raw data in Counts.
- **Background:** data in uncorrected Counts, acquired in darkness.
- **Reference:** background-corrected data for a buffer sample.

These modifications must follow a particular set of steps. First, the background image is recorded when the room is dark and the laser source is off. To ensure that the background is acquired in darkness, the input slit of the camera needs to be covered. Second, the laser source is turned on and the reference image is captured. Once these two steps are completed, the experiment can proceed. Finally, at the data processing stage, these images are subtracted from each frame to make modifications. Provided that the acquisition parameters remain unchanged, the background and reference scans are automatically used for subsequent data acquisitions whenever capturing Signals.

Binning. After correction of the images for background and normalization to adjust for spatial non-uniformities, peak width and relative positions were characterized by binning all CCD images in a direction perpendicular to the separation axis. The two main variants of the binning process are vertical binning and horizontal binning. The binning factor represents the number of adjacent pixels whose charge will be summed and digitized as a single pixel in either direction. In full vertical binning (FVB) mode, on a 1650 by 200 chip, the resulting image would be 1650×1. Binning increases the charge and light intensity of the resulting pixel at the expense of spatial resolution.

Progress Scanning Problem. The difference in light intensity between rows is due to the fact that the camera uses a full frame CCD sensor, which utilises a "progress scan" readout. The progress scan readout used in the CCD sensor means that the CCD is photosensitive during the readout phase. Therefore any photons impacting on the CCD during the readout period will result in charge accumulating in the pixels. As the back row pixels are the last to be processed by the readout register, they will be exposed to light for a longer period of time than the rows at the front of the CCD sensor. Therefore the rows at the back of the CCD chip will accumulate more charge and thus display a higher light intensity (Figure 4.12). Further information on full frame CCDs and progress scanning can be found in Reference [129].

Eliminating this effect requires the use of a shutter or pulsed light source, so as to prevent light from impinging on the camera during the readout period. In the current study, an internal trigger mode was employed with a pixel readout time of 0.67 μs and vertical shift speed of 13 μs, and exposure time of 0.1 s. On the other hand, all the frames in a kinetic series experience similar progress scanning, and it is normalized for the applications wherein frames are used relatively, e.g. those measuring diffusion coefficients at different time periods.

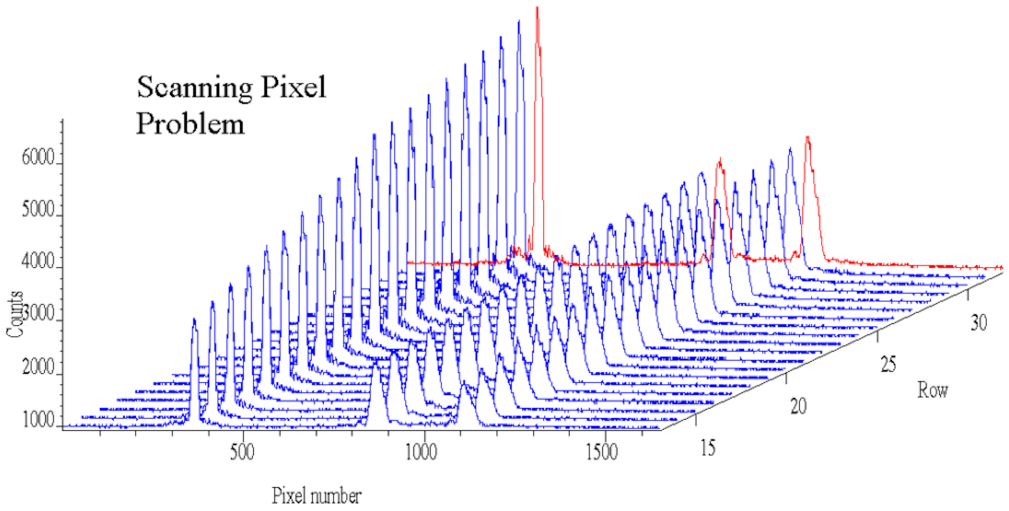

Figure 4.12: Scan probe problem increased at higher exposure time and slow readout speed.

Noise reduction. Noise cannot be avoided in Schlieren imaging, especially from digital camera sensors. In Schlieren applications for which high sensitivity is needed, visual and quantitative analysis can be affected by the poor quality of the image as a result of noise [130]. In order to address this issue, the signal-to-noise ratio was improved by increasing the number of accumulations, in which data from several scans of the same image were recorded and averaged by the fast scanning CCD sensor to reduce noise. This results in improved SNR, at the cost of temporal resolution loss. However, the required temporal resolution is obtained after accumulation by the fast scanning rate offered by the camera.

The derivative nature of the concentration gradient allows effective removal of the refractive index drifts produced by temperature fluctuation. Pawliszyn [131, 132] proposed a simple differential refractive index gradient detector based on Schlieren optics which is rather insensitive to thermal fluctuations inside the capillary. This method eliminates low-frequency noise associated with refractive Index drifts produced by temperature instabilities. Regardless of the drift removal feature of this method, according to the low current during the experiment, the generated heat does not produce considerable temperature gradient inside channels or capillary. The camera temperature was set to zero centigrade and maintained at this temperature during the experiment to minimize the shot noise.

4.5 Results and discussion

In this section, the results from the set of CIEF and MBE experiments are discussed to illustrate the COC-chip performance in conjunction with two detection approaches, namely, UV absorbance and concentration gradient detectors. The primary tests ran in a single channel by adjusting the chip to the commercial UV-WCID instrument. Results from these experiments were validated through a comparison with the capillary cartridge.

The effects of channel's geometry and dimension were investigated by conducting the experiments in channels with different dimensions. The round cross-section of the capillary versus the rectangular or square form of the channels' cross-section was also taken into account to investigate the influence of the separation column's geometry on detection sensitivity. Studies with multiple channels were performed to demonstrate the improved sample throughput, along with intra-channel experiments to show run-to-run reproducibility.

As mentioned before, fast kinetic data acquisition of the CCD camera facilitated recording of a time sequence of optical images, demonstrating the potential of the CCD camera as a powerful tool for studying dynamic processes such as diffusion. Furthermore, the explained data treatments (Section 4.4.2) were employed to improve the Schlieren images for quantitative analysis of the diffusion coefficient measurement.

4.5.1 CIEF with UV-WCID

The COC multi-channel chip was examined by CIEF-UV-WCID; different parameters such as reproducibility, resolution, and wall-interaction were compared to those of the commercial capillary cartridge (Table 4.1). And properties of the multi-channel slide for chip-based electrophoresis analysis have been investigated by UV whole column imaging detection. Short channels or capillaries are required in order to image the whole separation column. In conventional single point detection, long capillaries are used, and shallow pH gradients are generated as a result. The concern about decrease in resolution due to using short capillary was theoretically addressed by Mao and Pawliszyn [133]. They have considered concentration of a sample zone focused in a capillary by the isoelectric focusing process as a Gaussian distribution with a variance of σ, and relate it to the resolution, using the criterion of three times the variance for resolved adjacent peaks. Hence, the resolving power (ΔpI) can be expressed as [134]:

$$\Delta pI = 3\sqrt{\frac{D}{E}\frac{d(pH)}{-d\mu}\frac{d(pH)}{dx}} \tag{4.8}$$

Equation 4.8 shows that good resolution (small ΔpI) is obtained by a high field strength, a low diffusion coefficient, a high mobility slope, $\frac{d\mu}{d(pH)}$, and a narrow pH gradient. Improving the resolution is possible through variation of the field strength and pH gradient, because the diffusion coefficient and the mobility slope are intrinsic properties of the analytes. Efficient heat dissipation is necessary for applying high filed strengths, which is acquired by employing narrow-bore fused silica capillaries. Therefore, the resolution is independent of the length of the separation column, however considering the Joule heating issue, it is related to the surface-to-volume-ratio of the separation column.

Evaluation of the Multi-channel Chip

As discussed in Section 4.3.2, the chip was cut into a short piece holding channel C (Figure 4.9), and aligned with the UV detector. The commercial cartridge has a capillary with 100 μm diameter and a corresponding surface to volume ratio of 0.04 μM^{-1}. The most similar channel was C, which was used for the comparison. The channel and two small capillary segments (6 mm each) made a total separation column of 3 cm. Selection of a proper model protein and carrier ampholyte is important, since the obtained peaks need to appear in the detection window (18 mm). Ensuring equal volumes in both reservoirs is beneficial in preventing hydrodynamic flow that alters the results.

In order to investigate the resolving capability of the chip, a mixture of two myoglobin pI markers (pI 6.8 and 7.2, 0.5 $\frac{mg}{ml}$) with a carrier ampholyte at pH gradient range from 6 to 8 was introduced into the separation channel that generates the pH gradient of $\frac{d(pH)}{dx} \simeq 0.7$ ($\frac{pHunit}{cm}$). In the capillary cartridge, a longer column (5 cm) and a wider pH range (3-10) create a pH gradient of 1.4 ($\frac{pHunit}{cm}$), which is two-fold greater than that of the COC-chip gradient. The choice of carrier ampholyte range influences the generated pH gradient and the resolution. For example, a high resolution of $\simeq$ 0.03 pH units can be achieved in a 5-cm-long capillary performed with imaged CIEF, when a narrow pH gradient of 6 to 8 with a high voltage of 3 kV is used [35]. In this experiment, focusing was performed at 1.5 kV for 2 min, followed by 3 kV for 7 more minutes. Under the employed conditions, shallower pH gradient was formed in the multi-channel chip that has positively contributed in the resolving power of the separation experiment.

A comparison of the separation experiments in the COC-chip and the commercial chip, as demonstrated in Figure 4.13, showed that the two myoglobin isoforms were fairly well-resolved in both devices. However, the corresponding peaks were broader for the COC chip, thus suggesting analyte wall adsorption. Due to the inert surface of the plastic chip, its channel-preconditioning for EOF suppression was not as important, compared to the fused

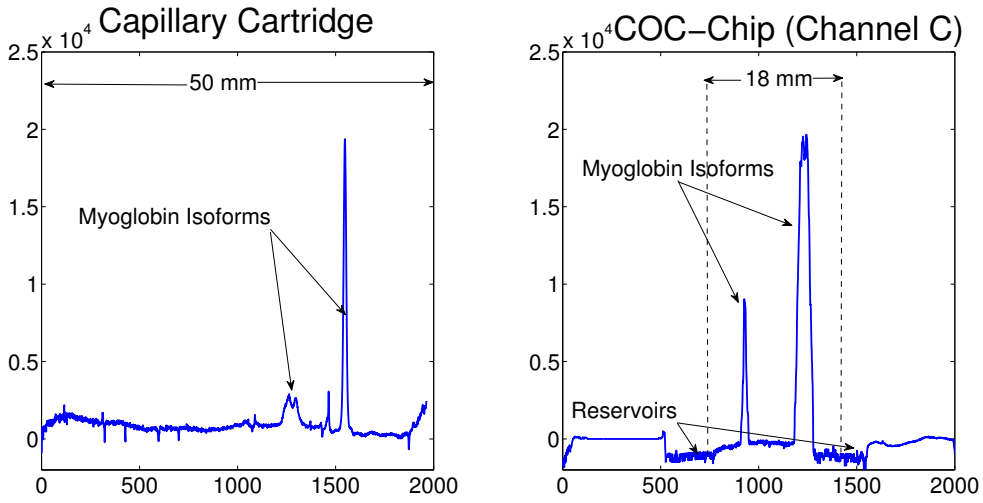

Figure 4.13: Evaluation of the multi-channel chip (D_H=100μm, Length=3 cm (1.8 cm detection window)) in comparison with commercial capillary cartridge (ID=100μm, Length=5 cm), through CIEF experiment of myoglobin isoforms with UV-WCID. Myoglobin pI markers (pI 6.8 and 7.2, 0.5 $\frac{mg}{ml}$) with a carrier ampholyte at pH gradient 3-10 and 6-8 for the chip and capillary respectively. Applied voltage; 1.5 kV for 2 min, and 3 kV for 7 min.

silica in the commercial cartridge. Hence, flushing with water between runs was adequate to get reproducible data. A relative standard deviation of 1.8% for determination of the peak positions in three trials showed lower but comparable reproducibility to the similar experiment in the commercial channel (Table 4.1).

Lens Effect; Geometry of the Column

One of the apparent limitations of using round capillaries for path-length-dependent detection techniques such as UV absorbance is called lens effect, where the curvature of the capillary acts as a thick cylindrical lens with a short focal length and bends the incoming beam. Hence, the lens effect causes the collimated incoming light beam to become strongly uncollimated, and as a result, the stray light makes the light collection inefficient. This drawback can be addressed by using microchips with a rectangular channel. The reduction of beam scattering and distortion by means of the flat channel walls is very important for path-length-dependent optical detection schemes. Tsuda et al. reported increase in the

sensitivity of UV-vis absorbance detection method by running capillary zone electrophoresis inside a rectangular silica capillary, although at the expense of peak broadening [135].

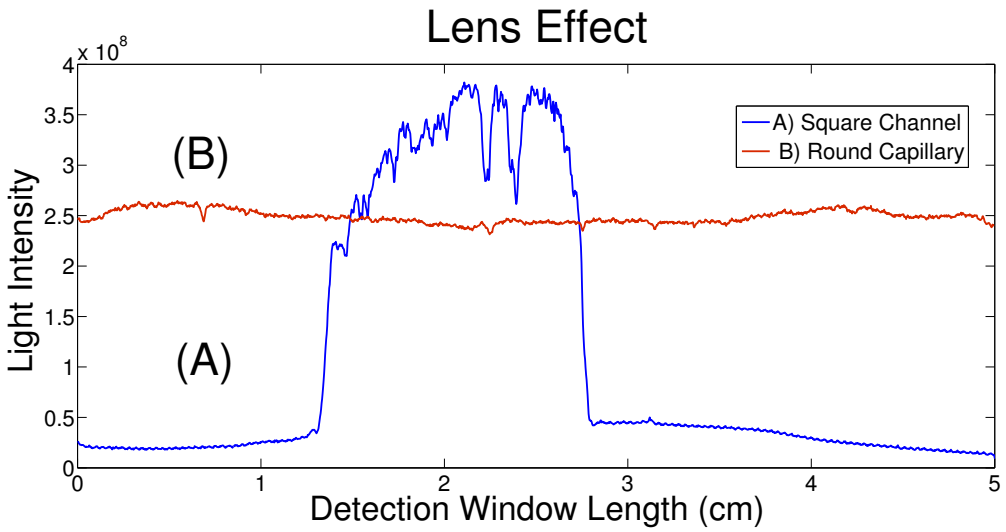

Figure 4.14: Comparison of the intensity of the incident light after passing through a round and square separation column: (A) 100 μm × 100 μm × 1.8 cm; (B) 100 μm ID × 5 cm. The separation columns were filled with water. Exposure time, 250 μs.

As shown in Figure 4.14, the light intensity profiles of a water-filled round capillary and a rectangular channel with identical diameters (100 μm), experimentally confirmed that the light beam passing a microchip have higher intensity than a capillary. The intensity of an incident light passing through a capillary of 100 μm ID was decreased to nearly one third of that passing through micro-channel of 100 μm × 100 μm. Moreover, in the case of narrow-bore circular capillaries, the available path length limits the detection sensitivity, especially when using the very common technique of UV-vis absorbance.

The Capillary Cartridge vs. The Multi-channel Chip

The capillary isoelectric focusing experiments were performed by UV-vis whole column imaging detection in channel C of the microchip as an identical separation column to the capillary. The results provide insight about the chip performance compared to the capillary cartridge. The specifications of the COC-chip have been reviewed in Section 4.3.2. Here, some of the key features of the multi-channel chip are summarized and compared to the commercial capillary cartridge (Table 4.1). A straightforward advantage of using

microchip in CIEF-WCID is the absence of lens effect, which contributes to better detection sensitivity.

The COC-chips are provided by their manufacturer as disposable products, however, according to the non-destructive nature of the employed chemicals, each chip can be used for 15 runs on average within three days, with narrower channels being subjected to blocking faster. The photo-mask layer's cost ($80 per sheet) has to be added up to the price of the multi-channel chip setup. This layer can be reused by detaching from the ruined chip. Hence, it is not included in the price comparison.

Feature	Multi-channel Chip	Capillary Cartridge
Material	Plastic (COC)	Fused Silica
EOF	Negligible	Need Suppression [a]
Lens Effect [b]	NA	Present
Durability	15 runs [c]	100 runs [128]
Cost	$ 60 [d]	$ 250
RSD (n=3)	$< 2\%$	$< 0.5\%$
Throughput	8 Channels	Single Capillary

Table 4.1: Comparison of the multi-channel chip with the commercial capillary cartridge.
a) Especially at pH values greater than three.
b) Created by the round shape of the separation column.
c) Within three consecutive days.
d) The photo mask layer price is not included.

One major source of band broadening is Joule heating, which arises from the electric current passing through the capillary, causing many undesired effects in CE. Taking the plastic slide material into account, the heat dissipation in the capillary is more efficient than in the chip. However, the use of narrow-bore capillaries and channels with larger surface-to-volume ratios increases the heat dissipation rate and helps decreasing the Joule heating effect. In the set of experiments run by MBE, the effect of Joule heating is negligible due to the low electric field strength. Additionally, the measurements by Schlieren detection have a derivative nature and inherently eliminate the drifts in temperature.

The channels on the chip are 18 mm long, while the commercial cartridge holds a capillary that is 50 mm long. The resolution does not have direct relation to the length of separation column (Equation 4.8). Therefore, miniaturizing the column can happen without sacrificing resolution in capillary isoelectric focusing. A number of advantages is associated with using a short column; for example, the capillary isoelectric focusing

experiment will perform faster in a short column. The whole separation column can be imaged by a charge-coupled device camera detector, which facilitates the study of dynamic processes. Sample consumption will be reduced in a short column, because the mixture of sample and carrier ampholytes usually fills the whole column, and requires a lager amount of the sample in a long column.

4.5.2 MBE with Schlieren Detection

Concentration gradient detection method is based on the refractive index gradient, which can be a function of changes in temperature and/or species concentration. Here, the inhomogeneity of the sample concentration causes a refractive index gradient that is recorded with the Schlieren detector. In moving boundary electrophoresis as a principal mode of CE, the samples are introduced through the frontal injection method into the capillary without discrimination. It provides higher sensitivity compared to the zone technique because no further dilution happen during the separation process. This approach, in combination with the Schlieren system has been already utilized for separation and detection of amino acids and carbohydrates [20]. However, the aim of this research is determination of the diffusion coefficient of proteins, and as such, the separation is not of main concern. Effect of channel dimension, as the detection cell, on detection sensitivity were examined by passing green laser light through different channels of the COC-chip and detecting by Schlieren imaging system.

Individual Channels: Effect of Dimension

Specification of the separation column is particularly important in optical detection technologies, as it does not only affect the separation efficiency but also influences the sensitivity of the method, as a detection cell. The employed COC chip consists of multiple channels with different cross-sections in square and rectangular forms. Pressure-driven flows in the channels can lead to large dispersion, which is because of lower convective velocity of the solute near the walls than it is in the center. Accordingly, among the eight channels (Figure 4.8) on the chip, four are too wide for the purpose of the experiment, and have very fast hydrodynamic flow rates. Thus, to investigate the effect of channel geometry and dimension, the experiments were conducted in the other four channels, with specifications shown in Table 4.2. Two of the channels, labelled D, have exactly the same dimensions, hence they are employed in simultaneous measurements and verifying reproducibility of the experiments. The diameter of the non-circular channels are defined as hydraulic diameter,

D_H, which is reciprocal to the diameter of a round tube or capillary, making for an easier comparison.

Channel	C	D	E	Capillary
width × depth (μm^2)	100 × 100	50 × 50	100 × 50	round
SVR (μM^{-1})	0.04	0.08	0.06	0.04
Hydraulic diameter,$D_H(\mu m)$	100	50	67	100
Duct Geometry	Square	Square	Rectangular	Circular

Table 4.2: Employed channels' specifications. SVR: Surface Area to Volume Ratio

Channel D and C have a square form, while Channel E is rectangularly shaped. Channel C is the deepest, hence providing the longest light path. The width of channel D is half of others hence considered the narrowest channel. Channel E is rather planar, with a shallow depth and wide breadth. Different dimensions make different surface-area-to-volume ratios (SVR) for each channel. The higher the SVR, the more efficient the heat dissipation.

Detection cell: The channels were examined individually, by measuring the light intensity that passed through these channels with different dimensions. Each water-filled channel was placed on the platform in the testing region, so that the center of the laser beam spot was illuminated on one specific channel at a time. This particular location was chosen to compensate for the uneven distribution of the laser source. The light intensity profiles of the three channels were obtained in the same way and overlaid in a graph in Figure 4.15 for comparison. As expected, the wider channels, C and E, provided broader profiles, exhibiting broader pixel distributions. However, the sensitivity of the detection in Schlieren method is not influenced by the depth of the channel considerably, and the shallower channel shows only a little higher light intensity.

An essential problem associated with conventional circular capillaries is the optical distortion caused by the arc of the capillary walls, which can negatively affect refractive index or photon deflection measurements. It may also provide undesirable scatter light. Furthermore, when direct counting mode is used, the curvature of the capillary walls can cause mistaken counts [135].

As demonstrated in Figure 4.15, the Gaussian distribution of the light intensity shows maximum Counts in the middle of the channels, while attenuating as it got closer to the channel walls. There are two ways to plot the sample profile obtained from a channel; namely, mid-row and binning approaches. In the binning method, the diffusion in both axial and radial directions was taken into account by averaging the region of interest

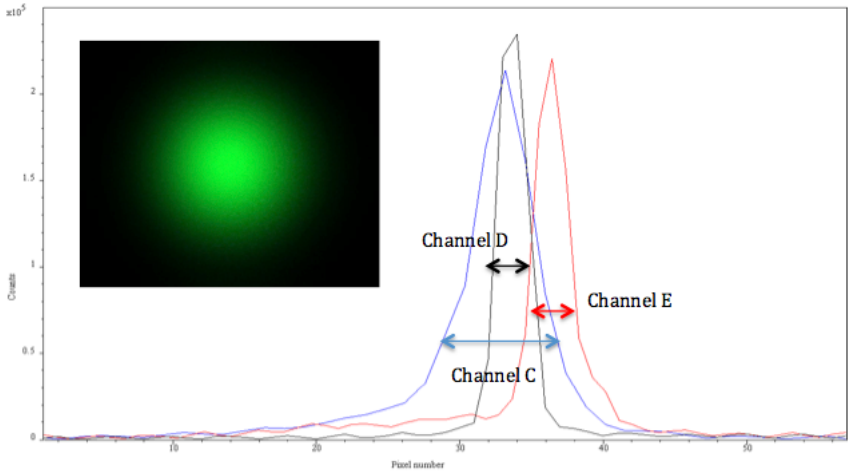

Figure 4.15: Effect of the channel dimension on the light intensity profile.

through binning the pixels of the channel rows. In the mid-row method, on the other hand, the sample profile was approximated by considering the sole middle row in the channel, which has the highest intensity. The middle row displayed the highest intensity profile, with the signal attenuating as it moved away from the channel center. Despite the fact that the binning method reflected a more realistic measurement of the fluid flow, it might impose extra error in the case of analytes with low concentration (poor SNR). The lowest signal-to-noise ratio can be found in the vicinity of the channel walls. In general, binning method had better accuracy, whereas the mid-row approximation can be adapted for simplicity, in the analysis of the signals with high SNR values.

Electrophoresis column: Dispersion of tryptophan was monitored at a specific point of the separation column (close to the sample reservoir) to investigate the effects of C, D, and E channel dimensions on the peak broadening in moving boundary electrophoresis measurement. The amplitude of the tryptophan (1 $\frac{mg}{ml}$) signal in the background corrected Count unit was recorded in each channel for three replicates. Besides the solutes, the migration of the buffer components in the bulk flow was also visualized; this effect was more drastic at lower concentrations of analytes, yielding poor signal-to-noise ratios.

The fluid flow under the given electric field and with regard to the channel dimension was determined, and the signal amplitude was calculated through vertical binning method. The length of the channel is determined by the columns (200 pixels), while the width of the channel is depicted by the rows. For example, channel C was 100 μm wide and each

pixel was 16 μm^2, covering almost 6 pixel-rows.

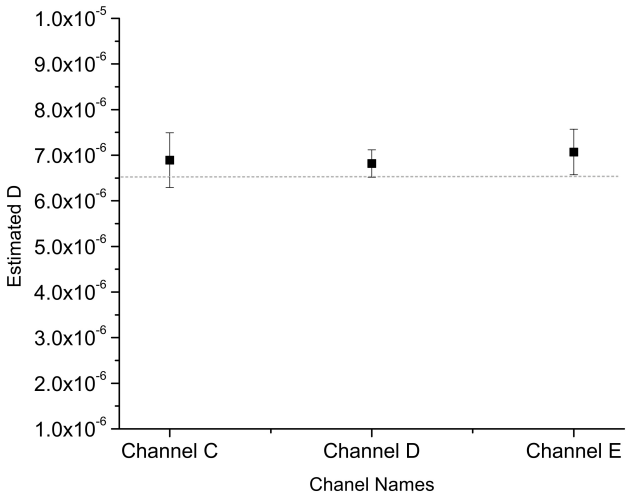

Figure 4.16: Diffusion coefficient measurement of tryptophan (1 $\frac{mg}{ml}$) by moving boundary electrophoresis coupled with Schlieren imaging detection within different channels.

The results in Table 4.3, are graphically demonstrated in the scattered plot, Figure 4.16. The line in the graph represents the diffusion coefficient value reported in the literature for tryptophan. The experiments conducted in each channel at least for three trials and the error in determined diffusion coefficients shows reproducibility of the measurements.

Channel	C	D	E
$D_{tryp.} \times 10^6 \frac{s}{cm^2}$	6.9($\pm$0.6)	6.8($\pm$0.3)	7.0($\pm$0.5)
%Error	5.3	3.8	6.8
RSD (n=3)	8.6	4.4	7.1

Table 4.3: Diffusion coefficient measurement of tryptophan (1 $\frac{mg}{ml}$) by moving boundary electrophoresis coupled with Schlieren imaging detection within different channels.

Channel C showed the least precision in measurements due to the higher influence of the hydrodynamic flow in the presence of a subtle differences in the electrolyte levels. The experiment in channels C and E showed a higher error margin compared to channel D. The diffusion coefficient estimation in channel E with binning method deviated the most from the true value, as the number of rows with poor SNR are doubled compared to

channel D. In general, all channels have acceptable results and the effect of dimension is not very considerable. The dimension factors that slightly influenced the measurement are the shallower depth of the channels that resulted in higher sensitivity due to lower stray light, and the breadth of the channels, which inversely affected the precision and accuracy of the measurements because of increasing the dispersion and lowering the SNR.

Channel D with square cross-section, $D_H = 50\ \mu m$, and highest surface-to-volume-ratio ($0.08\ \mu M^{-1}$) proved to have the most suitable dimensions for this experiment. In the following section, the high-throughput experiments for determination of diffusion coefficient were performed simultaneously in two D channels.

Multiple Channels: High-throughput Analysis

Of date, the high-throughput CE analysis has been drawing more attention from the scientific community. The multiplexed devices are mostly in the format of chip-based multi-capillary electrophoresis with a signal detection system based on using charge coupled device cameras for the fluorescent detection [136, 137], or UV absorption imaging detection [38], where two-dimensional CCD sensor records the light beam passes through a capillary array.

In the present study, the multi-channel chip is employed, which eliminates the lens effect drawback associated with round capillaries. The effective compatibility of the Schlieren imaging system with chip-based electrophoresis makes it an appropriate choice for high-throughput analysis. Using a multiple channels for MBE experiment can greatly increase the sample throughput, making it comparable with gel slab electrophoresis, with much faster analysis speed in a channel. In order to perform multi-channel detection, two problems were solved; the illumination system for multiple channels, and the simultaneous measurement of light intensity passing through the channels. A photo-mask layer holding slits fixed above the channels, and cut-off all stray light rays from incoming collimated light. Each channel on the chip is independent, the distance between channels eliminates any signal cross-talking problem. And finally, using a two-dimensional CCD camera enabled measuring the intensity of a light beam passing through all the channels concurrently.

Throughput: The employed Schlieren optics provide a view field of maximum 5 channels (Figure 4.5). However, the experiments were conducted in two channel Ds simultaneously for two reasons. Firstly, this allowed minimizing the effect of uneven distribution of the light source intensity. In addition to normalizing images by light intensity, recorded simultaneously with the images, that compensate for intensity fluctuation of the light

source. Secondly, the identical channel runs allowed for reproducibility considerations with regards to the run-to-run inter-channel measurements. Moving boundary electrophoresis and detection of two samples can be completed in about 3 min, and the sample front flow and diffusion in both channels can be observed simultaneously by the real-time, on-line imaging detector.

Reproducibility: The relative standard deviation from run to run for three trials in channels D 4.4%, indicating acceptable reproducibility. However, the COC chip precision in the CIEF experiment (1.8%) was much better than that of MBE, due to different sample introduction and experimental procedures. Reproducibility in CE methodologies can be compromised by different factors including buffers, capillary, modes of injections, and applied voltage [138]. The major source of experimental variation in moving boundary electrophoresis was the non-automated injection system; the empty/fill step was the most vulnerable stage of the experiment, in which there might be inconsistencies due to incomplete withdrawal of the electrolyte. The reproducibility of the experiment can be improved by replacing the manual sample introduction with an automated one. Although the samples were injected parallel into the channels, the image (Figure 4.17a) shows that they are not moving together, this might be due to same reasons arise irreproducibility.

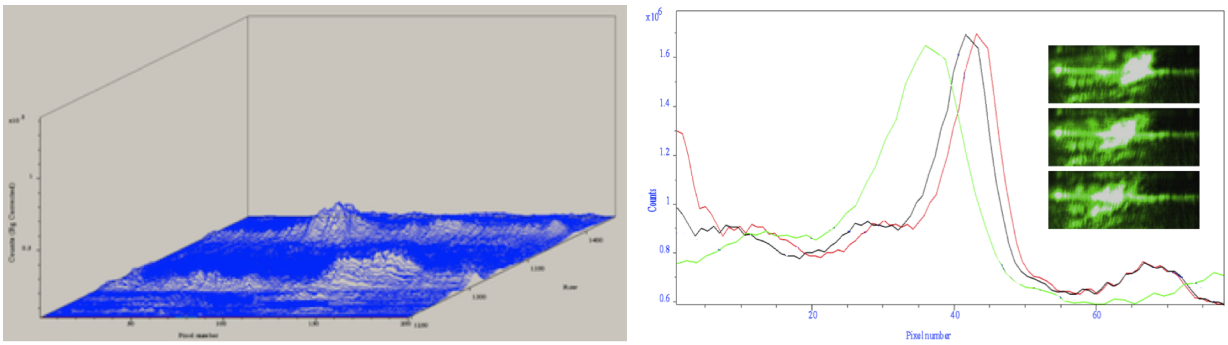

(a) Multi-channel Run

(b) Diffusion Coefficient Estimation

Figure 4.17: Estimation of the tryptophan diffusion coefficient by MBE experiment simultaneously in two D channels; (a) the Schlieren 3D-image of tryptophan inside two channels, (b) The concentration profile (binned) of tryptophan diffusion at three diffusion times.

Figure 4.17a illustrates the MBE of tryptophan in two D channels, and the subset 4.17b demonstrates the corresponding binned profile at three time frames. Measurement of the tryptophan diffusion coefficient at the same time can be expanded to a higher number of channels with improvements in the optical elements.

Determination of Diffusion Coefficient

Microfluidic devices can be used in a variety of interesting applications including molecular diffusion coefficient measurement [139, 140]. In this section, diffusion coefficient measurements by dynamic method of MBE with imaging Schlieren detection is compared with static imaging method of CIEF with UV-WCID inside channel C of the micro-fabricated multi-channel device. These comparisons were made using tryptophan and BSA samples. The evaluation of the precision and accuracy of the measurements (Table 4.4) proved better performance of static mode. However, either of the methods had its own advantages and shortcomings; the static (CIEF) diffusion coefficient measurement method was more accurate, and robust, whereas the on-the-fly (MBE) method was simpler and faster with acceptable results within experimental error range.

In the literature, estimation of diffusion coefficients has been suggested based on signal peak height for the CIEF with a concentration gradient Schlieren imaging detector [26]. As shown by experimental results (Chapter 3), the calculation in the time domain, especially based on peak height and width, is not as effective as the frequency domain. An average concentration detector would visualize the moving boundary signal as a sigmoid peak, which is not easy to deal with in the FT approach, however, using the concentration gradient detection (Schlieren); the output signal would have a derivative form that looks like a Gaussian-wise shape. Hence, in the current research, the diffusion coefficient measurements were calculated by Fourier transformation method.

Amino Acid / Protein	$D_{Stc.}$ (cm^2/s)	$D_{Dyn.}$ (cm^2/s)	$D_{Lit.}$ (cm^2/s)	$\%Er_{Stc.}$	$\%Er_{Dyn.}$
Tryptophan	6.2×10^{-6}	6.9×10^{-6}	6.55×10^{-6} [106]	5.3	7.0
Bovine Serum Albumin	5.3×10^{-7}	6.7×10^{-7}	5.90×10^{-7} [45]	10.1	14.1

Table 4.4: Diffusion coefficient measurement by two approaches; Dynamic method, $D_{Dyn.}$, through MBE with Schlieren imaging detection, and Static method, $D_{Stc.}$, through CIEF experiment followed by UV-WCID in channel C.

After binning the channel rows in the image at different dispersion time intervals, the obtained profiles were used for determination of diffusion coefficient through FT approach. The Fourier analysis was applied directly to the signal, as discussed before (Chapter 3). Tryptophan and BSA diffusion coefficients were determined in channel C with error percent 14.1% and 7.0% respectively. The diffusion coefficient was measured in a static fashion in the CIEF experiment, where the focused protein band started to diffuse after the voltage was disconnected and the sample plug moves due to the concentration gradient with its

vicinity media. However, in the MBE with Schlieren detection, the measurements were performed in dynamic mode, in which the diffusion of the sample front was monitored in presence of the electric field, an on-the-fly-electrophoresis. The former mode is inherently more appropriate for measuring the diffusion coefficient. Thus, the comparison of the obtained values (Table 4.4) by either of these two methods reinforced the higher efficiency of the static mode for this purpose.

4.5.3 Limitations of The Technique

Beside advantages offered by concentration gradient Schlieren imaging detection, there are some drawbacks associated with both the concentration gradient technique and the operational Schlieren optics, which affect the efficiency of the method.

Methodological Drawbacks

Refractive index gradient measurement is a universal technique . The main advantage of this inherent feature of the refractive index gradient detector is that a wide variety of compounds can be detected by this method. However, this universal feature, results in the contribution of other existing compounds, such as carrier ampholytes in CIEF experiments, to the signal and make it noisy and inappropriate for quantitative analysis. On the other hand, increasing the solute concentration to enhance the difference between the refractive index of the analyte and that of the solvent is not suitable for determination of diffusion coefficient, which is more accurately estimated in dilute solutions.

The output of this method is in derivative form. This can be considered a disadvantage in CIEF mode, in which the signal appears in the Gaussian first-derivative shape and need to be integrated to go back to the Gaussian-like peak shape. However, it is an apparent advantage in the MBE mode, in which the sigmoid shape signal (due to frontal injection) is converted to the more convenient Gaussian shape signal.

Operational Drawbacks

The most obvious instrumental limitation of the studied Schlieren system is the size and portability. The size of the system depends on the size and focal-length of the employed lenses. All the systems elements are fixed on a vibration isolation table in a dark room to avoid any additional ambient noise. Hence, the system itself is neither flexible nor portable. Automation is another critical issue in CE experiments since manual injection

and optimization of the optical elements and Stop for each trial are tedious tasks, which also affect the repeatability of the operation that is necessary for precise quantitative analysis.

Spherical Aberration. The quality of the employed optical elements plays an important role in the sensitivity and resolution of the method. There is a problem associated with using spherical lenses, in that the curvature of the lens surface, especially at the edges, makes the image of the channels bend at the far ends. This effect is also known as *spherical aberration*, and the exterior part of the image is not flat in the presence of this effect. This can be eliminated by either using the center of the spherical lens, or by replacing the spherical lens with a cylindrical one where the image is transferred through the lens axis to produce a sharp image of all observed channels.

Disposable Multi-channel Chip. Despite outstanding characteristics of the prototyped COC-slide for the purpose of the experiment, due to high cost of the material it is not financially justified. Each slide costs $60, with an average durability of 15 runs compared with the commercial capillary chip that costs $250 with 100 runs performance.

4.6 Summary and Conclusion

The miniaturized multi-channel chip was successfully coupled with concentration gradient detection based on Schlieren optics and demonstrated a great potential for universal, sensitive, and high-throughput measurements of diffusion coefficients of proteins. The effect of channel geometry and dimension on the separation and detection was explored with respect to the light path as well as wall-interaction and dispersion of the solute.

Preliminary characterizations of the micro-fluidic device were examined in a conventional iCE280 instrument with UV-WCID, through a side-by-side comparison with commercial capillary-based chip. This evaluation proves that the proposed multi-channel chip is a viable choice for electrophoresis experiments. The square or rectangular micro-channel reduces the lens effects associated with the capillary format.

The analysis throughput was improved by taking advantage of the Schlieren microscopy with a two-dimensional CCD. The speed and high resolution of the CCD camera make it an attractive choice for exploring dynamic and kinetic processes. Further enhancement of the imaging system is still possible, by improving the optical elements.

In summary, the proposed experimental method can be employed for simple, fast, and high-throughput analysis of proteins to determine their diffusion coefficient value. In

spite of the great advantages of the employed micro-fluidic device in compatibility for electerophoresis analysis, it is not economic due to its low durability.

Chapter 5

Contributions and Conclusions

The main objective obtained by the research detailed here is improvements in determination of diffusion coefficient of proteins, which fall into two broad categories: data analysis, called the software aspect, and instrumental developments, called the hardware aspect. This dissertation makes the following major contributions to the literature.

5.1 Major Contributions

A real time monitoring system was designed and implemented to monitor the diffusion process and the spatial data carried to the frequency domain for fast and accurate determination of diffusion coefficients. A miniaturized multi-channel chip was successfully employed as a high-throughput micro-fluidic device for capillary electrophoresis analysis of proteins with concentration gradient detection based on Schlieren optics.

Software Aspects A computer program was generated to model the diffusion process, on the basis of the Fourier transformation solution to the Ficks law equation to estimate the diffusion coefficient. The employed FT model was validated experimentally through CIEF, iPF, and MBE techniques, by applying the model to a electropherograms of the diffusion path of a set of proteins. It is shown that FT enables the capillary electrophoresis technique equipped with dynamic imaging detection as a unique and powerful method, among different methodologies proposed in the literature, for measuring diffusion coefficients. Experimental results have confirmed that the FT procedure enhances the accuracy of the determined values compared to those obtained in the time domain.

One of the most restrictive limitations, for time domain analysis, is the required assumption of Gaussian distribution for the signal. In contrast, the FT method renders the calculations largely independent of peak shape, and it thus retrieves more accurate results from complex or convoluted signals. The robustness of the FT method toward variations of peak shape has been explored, and the results prove that this method is not restricted by any peak shape assumption as it is in the time domain. The frequency domain analysis facilitated the processing of irregular shape experimental data.

Hardware Aspects A comprehensive introduction of protein diffusion coefficient estimation by capillary electrophoresis method has been provided along with demonstration of various mechanisms and detection modes. The diffusion coefficients of a number of proteins were measured by different detection techniques; UV and concentration gradient Schlieren detectors illustrated the whole column static mode and the partial column dynamic detection modes, respectively. The prototyped plastic multi-channel chip coupled with concentration gradient imaging detection based on Schlieren optics has been successfully examined by simultaneous analysis of the proteins in parallel channels.

5.2 Conclusions

This dissertation is a paper-based one. Therefore, conclusions with additional details are presented at the end of each chapter.

APPENDICES

Time Domain Algorithm

```
clc;clear all;close all;
%------------------------------Initial value-----------------------
D=1e-6;Ts=0.0002;x=-0.35:Ts:0.35;

t_vector=[30:30:630];

Desired_SNR_dB=[1 3 5 15 50];

gs0=(1/(sqrt(2*pi*2*D*t_vector(1))))*exp(-x.^2/(2*2*D*t_vector(1)));
maximm0=max(gs0);
gs0=gs0./maximm0;

for i=1:length(Desired_SNR_dB)
for j=1:1000

    N=length(gs0);
    sigp = 10*log10(norm(gs0,2)^2/size(gs0,2));
    snr = sigp-Desired_SNR_dB(i);
    noisep = 10^(snr/10);
    noise = sqrt(noisep)*randn(size(gs0));

D_estimated_vector_gs=[];
w1_2_gs=[];

for t =1:length(t_vector)

    sigma= 2*D*t_vector(t);
    gs=(1/(sqrt(2*pi*sigma)))*exp(-x.^2/(2*sigma));

```

```
    maximm=max(gs);

 gs=gs./maximm;
 gs_noise=gs+noise;

    peak_height= max(gs_noise);
    w1_2_height= (peak_height)/2;
    ind_v=(gs_noise<=w1_2_height);
    a= diff(ind_v);
    L1= find(a==-1);L1= L1(1);
    L2= find(a==1); L2= L2(end);
    w1_2_gs(t,1)= x(L2)-x(L1);
end

%------------Estimated D from Guassian signal-----------------

sigma_vector= (w1_2_gs)./2.3;
sigma_vector=sigma_vector.^2;
dt_vector= t_vector(1:end)-t_vector(1);
coeff = polyfit(t_vector,sigma_vector',1);
D_estimated_gsn1(1,j)=[D_estimated_vector_gs coeff(1)/2];
D_std1(1,j)=std(D_estimated_gsn1);
error_gsn1(1,j)=abs((abs(D-(D_estimated_gsn1(1,j)))/D)*100);
end

D_estimated_gsn(1,i)=mean(abs(D_estimated_gsn1));
D_std(1,i)= mean(abs(D_std1));

RSD(1,i)=100*((D_std(1,i))./D_estimated_gsn(1,i));

error_gsn(1,i)=mean(error_gsn1);

end

results=zeros(4,length(Desired_SNR_dB));
results(1,:)=Desired_SNR_dB;
results(2,:)=D_estimated_gsn;
results(3,:)=D_std;
results(4,:)=error_gsn;
results
RSD
```

Frequency Domain Algorithm

```
clc;clear all;close all;format('shortg');

%% Initial value
D=1e-6;Ts=0.002;v=0.35;x=-v:Ts:v;
t_vector=[30:30:630];

Desired_SNR_dB=[1 3 5 15 50];

%% Generate Initial Signal

G0=(1/(sqrt(2*pi*(2*D*t_vector(1)))))*exp(-x.^2/(2*(2*D*t_vector(1))));

%% Noise Loop

for i=1:length(Desired_SNR_dB)

for j=1:1000

    N=length(G0);
    sigp = 10*log10(norm(G0,2)^2/size(G0,2));
    nosp = sigp-Desired_SNR_dB(i);
    nosa = 10^(nosp/10);
    noise = sqrt(nosa)*randn(size(G0));

         G0=G0+noise;
         maximm0=max(G0);
         G0=G0./maximm0;

  nf0= length(G0);f0= fft(G0,nf0);f_abs0 ...
      =abs(f0);f_abs0=fftshift(f_abs0);

output=[];
for t =1:length( t_vector)

     sigma= 2*D*t_vector(t);
     gs=(1/(sqrt(2*pi*sigma)))*exp(-x.^2/(2*sigma));

     gs_noise=gs+noise;

if t==1
    maximm=max(gs_noise);
```

```
41 end
42 gs_noise=gs_noise./maximm;
43
44              nf= length( gs_noise);
45              f = fft( gs_noise,nf);
46              f_abs = abs(f);
47              f_abs = fftshift(f_abs);
48              w=f_abs./f_abs0;
49              logratio = -log(f_abs./f_abs0);
50              m=(length( gs_noise)-1)/2;
51              Omega = (-m:m)* 2*pi/(Ts*nf);
52              Omega2= Omega.^2;
53              c =logratio./Omega2;
54              output=[output c(m)];
55 end
56
57 %% Estimated D from Guassian signal in the frequency domain
58
59 slope_at_each_point= diff(output)./diff(t_vector);
60 D_estimated_gsn1(1,j)=(mean(slope_at_each_point));
61 D_std1(1,j)=std(D_estimated_gsn1);
62 error_gsn1(1,j)=((abs(D-(D_estimated_gsn1(1,j))))/D)*100);
63
64 end
65
66 D_estimated_gsn(1,i)=mean(abs(D_estimated_gsn1));
67 D_std(1,i)= mean(abs(D_std1));
68
69 RSD(1,i)=100*((D_std(1,i))./D_estimated_gsn(1,i));
70
71 error_gsn(1,i)=mean(error_gsn1);
72
73 end
74
75 results=zeros(4,length(Desired_SNR_dB));
76 results(1,:)=Desired_SNR_dB;
77 results(2,:)=D_estimated_gsn;
78 results(3,:)=D_std;
79 results(4,:)=error_gsn;
80
81 results
82 RSD
```

References

[1] Douglas A. Skoog, F. James Holler, and TimothyA. Nieman. Capillary Electrophoresis and Capillary Electrochromatography. In *Principales of Instrumnetal Analysis*, chapter 30. Sunders Golden Sunburst Series, Philadelphia, 5th edition, 1998.

[2] Pier Giorgio Righetti. Capillary Electrophoretic Analysis of Proteins and Peptides of Biomedical and Pharmacological Interest. *Biopharm. Drug Dispos.*, 22:337–351, 2001.

[3] Xiaohua Huang, William F Wf Coleman, and Richard N Zare. Analysis of factors causing peak broadening in capillary zone electrophoresis. *Journal of Chromatography A*, 480:95–110, 1989.

[4] James Jorgenson. Overview of Electrophoresis. In *New Directions in Electrophoretic Methods*, chapter 1. American Chemical Society, Washington, DC, acs sympos edition, 1987.

[5] A. Tiselius. *The moving boundary method of studying the electrophoreses of proteins*. Nova acta Regiae Societatis Scientiarum Upsaliensis. Almquist & Wilksells boktryckeri, 1930.

[6] F M Everaerts and P E M Verheggen. Isotachophoresis : Electrophoretic analysis in capillaries. *Journal of Chromatography A*, 53:315–328, 1970.

[7] James W Jorgenson and Krynn Dearman Lukacs. Zone Electrophoresis in Open-Tubular Glass Capillaries. *Anal. Chem.*, 53(1):1298–1302, 1981.

[8] Shafaati A., Capillary Electrophoresis, 2005. http://www.docstoc.com/docs/108040687/CAPILLARY-ELECTROPHORESIS.

[9] Tim Wehr, M Zhu, and Roberto Rodriguez-Diaz. Capillary isoelectric focusing. *Electrophoresis*, 18(12-13):2134–2144, 1997.

[10] Tiemin Huang, Xing-zheng Wu, and Janusz Pawliszyn. Capillary Isoelectric Focusing without Carrier. *Anal. Chem.*, 72(19):4758–4761, 2000.

[11] X Liu, Z Sosic, and I S Krull. Capillary isoelectric focusing as a tool in the examination of antibodies, peptides and proteins of pharmaceutical interest. *Journal of chromatography. A*, 735:165–90, May 1996.

[12] L H H Silvertand, J Sastre Toraño, W P van Bennekom, and G J De Jong. Recent developments in capillary isoelectric focusing. *Journal of chromatography. A*, 1204(2):157–70, September 2008.

[13] G. S. Settles. *Schlieren and Shadowgraph Techniques: Visualizing Phenomena in Transparent Media.* Springer, 2 ed., 2006.

[14] Jiaqi Wu, Peter Frank, and Janusz Pawliszyn. Diode Laser-Based Concentration Gradient Detector for Detection of Capillary Isoelectric Focusing. *Applied Spectroscopy*, 46(12):1837–40, 1992.

[15] J Wu and J Pawliszyn. Application of capillary isoelectric focusing with universal concentration gradient detector to the analysis of protein samples. *Journal of chromatography*, 608(1-2):121–30, 1992.

[16] Jiaqi Wu and Janusz Pawliszyn. Dual Detection for Capillary Isoelectric Focusing with Refractive Index Gradient and Absorption Imaging Detectors. *Anal. Chem.*, (6):867–873, 1994.

[17] T McDonnell and J. Pawliszyn. Capillary isotachophoresis with concentration-gradient detection An application to the separation of synthetic peptides. *Journal of chromatography*, 559:489–97, 1991.

[18] T McDonnell and J Pawliszyn. Capillary isotachophoresis with concentration gradient detection. *Analytical chemistry*, 63(17):1884–9, 1991.

[19] Janusz Pawliszyn. Concentration Gradient Detector in Capillary Separation Technology. *Journal of Liquid Chromatography*, 10(15):3377–3392, 1987.

[20] J Pawliszyn and J Wu. Moving boundary capillary electrophoresis with concentration gradient detection. *Journal of chromatography*, 559:111–118, 1991.

[21] Janusz Pawliszyn. Multi-Purpose Capillary Electrophoresis System With Concentration Gradient Detection. *Talanta*, 39(10):1281–1288, 1992.

[22] L Vonguyen, J Wu, and J Pawliszyn. Peptide mapping of bovine and chicken cytochrome c by capillary isoelectric focusing with universal concentration gradient imaging. *Journal of chromatography. B, Biomedical applications*, 657(2):333–8, July 1994.

[23] Janusz Pawliszyn. Concentration Gradient Detection Based on Sclieren Optics. *Spectrochimica Acta Rev.*, 13(4):311–354, 1990.

[24] S. Hjerten. High Performance Electrophoresis Elimination of Electroendosmosis and Solute Adsorption. *Journal of chromatography*, 347:191–198, 1985.

[25] Xing-zheng Wu, Jiaqi Wu, and Janusz Pawliszyn. Whole-Column-Imaging Detection for Capillary Isoelectric Focusing and Capillary Electrophoresis. *LC GC North America*, 19(5):526–545, 2001.

[26] Jiaqi. Wu and Janusz. Pawliszyn. Capillary isoelectric focusing with a universal concentration gradient imaging system using a charge-coupled photodiode array. *Analytical Chemistry*, 64(23):219–224, December 1992.

[27] Xing-Zheng Wu, Tiemin Huang, Zhen Liu, and Janusz Pawliszyn. Whole-column imaging-detection techniques and their analytical applications. *TrAC Trends in Analytical Chemistry*, 24(5):369–382, May 2005.

[28] CIEF-WCID instrument. http://www.proteinsimple.com/ice_technology.html.

[29] Tao Bo and Janusz Pawliszyn. Characterization of phospholipid-protein interactions by capillary isoelectric focusing with whole-column imaging detection. *Analytical biochemistry*, 350(1):91–8, 2006.

[30] Zhen Liu, Andrei P Drabovich, Sergey N Krylov, and Janusz Pawliszyn. Dynamic kinetic capillary isoelectric focusing: a powerful tool for studying protein-DNA interactions. *Analytical chemistry*, 79(3):1097–100, February 2007.

[31] Tibebe Lemma, Rupasri Mandal, Xing-Fang Li, and Janusz Pawliszyn. Investigation of interaction between human hemoglobin A0 and platinum anticancer drugs by capillary isoelectric focusing with whole column imaging detection. *Journal of separation science*, 31(10):1803–9, 2008.

[32] Tibebe Lemma Mukria. *Investigation of Protein-drug Interaction using Capillary Isoelectric Focusing with Whole Column Imaging Detection and Spectroscopic Techniques*. PhD thesis, University of Waterloo, 2009.

[33] Zhen Liu and Janusz Pawliszyn. Capillary Isoelectric Focusing with Laser-Induced Fluorescence Whole Column Imaging Detection as a Tool To Monitor Reactions of Proteins research articles. *Journal of Proteome Research*, 3:567–571, 2004.

[34] X Fang, C Tragas, J Wu, Q Mao, and J Pawliszyn. Recent developments in capillary isoelectric focusing with whole-column imaging detection. *Electrophoresis*, 19(13):2290–5, 1998.

[35] Jiaqi Wu, Charalambos Tragas, Arthur Watson, and Janusz Pawliszyn. Capillary isoelectric focusing with whole column detection and a membrane sample preparation system. *Analytica Chimica Acta*, 383(1-2):67–78, March 1999.

[36] a Palm, C Lindh, S Hjertén, and J Pawliszyn. Capillary-zone electrophoresis in agarose gels using absorption imaging detection. *Electrophoresis*, 17(4):766–70, April 1996.

[37] X Gong and E S Yeung. An absorption detection approach for multiplexed capillary electrophoresis using a linear photodiode array. *Analytical chemistry*, 71(21):4989–96, November 1999.

[38] Jiaqi Wu and Janusz Pawliszyn. Absorption Spectra and Multicapillary Imaging Detection for Capillary lsoelectric Focusing Using a Charge Coupled Device Camera. *Analyst*, 120(May):1567–1571, 1995.

[39] J Wu and J Pawliszyn. Fast analysis of proteins by isoelectric focusing performed in capillary array detected with concentration gradient imaging system. *Electrophoresis*, 14(5-6):469–74, 1993.

[40] Jiaqi Wu and Janusz Pawliszyn. Protein analysis by isoelectric focusing in a capillary array with an absorption imaging detector. *Journal of Chromatography B: Biomedical Sciences and Applications*, 669(1):39–43, July 1995.

[41] H Pang, V Pavski, and E S Yeung. DNA sequencing using 96-capillary array electrophoresis. *Journal of biochemical and biophysical methods*, 41(2-3):121–32, December 1999.

[42] Matías Calcerrada, Philippe Roy, Carmen García-Ruiz, and Miguel González-Herráez. Photonic crystal fibres as efficient separation component in capillary electrophoresis. *Sensors and Actuators B: Chemical*, 191:264–269, February 2014.

[43] Shuqin Su, Graham T T Gibson, Samuel M Mugo, Dale M Marecak, and Richard D Oleschuk. Microstructured photonic fibers as multichannel electrospray emitters. *Analytical chemistry*, 81(17):7281–7, September 2009.

[44] S B Cheng, C D Skinner, J Taylor, S Attiya, W E Lee, G Picelli, and D J Harrison. Development of a multichannel microfluidic analysis system employing affinity capillary electrophoresis for immunoassay. *Analytical chemistry*, 73(7):1472–9, 2001.

[45] Zhen Liu, Tibebe Lemma, and Janusz Pawliszyn. Capillary Isoelectric Focusing Coupled with Dynamic Imaging Detection : A One-Dimensional Separation for Two-Dimensional Protein Characterization research articles. *J. Proteome Res.*, pages 1246–1251, 2006.

[46] William F Weiss Iv, Teresa M Young, and Christopher J Roberts. Principles , Approaches , and Challenges for Predicting Protein Aggregation Rates and Shelf Life. *Journal of Pharmaceutical Sciences*, 98(4):1246–1277, 2009.

[47] G. Taylor. Dispersion of Soluble Matter in Solvent Flowing Slowly through a Tube. *Proc. R. Soc. A*, 219(1137):186–203, 1953.

[48] G. Taylor. Conditions under Which Dispersion of a Solute in a Stream of Solvent can be Used to Measure Molecular Diffusion. *Proc. R. Soc. A*, 225(1163):473–477, 1954.

[49] G. Taylor. The Dispersion of Matter in Turbulent Flow through a Pipe. *Proc. R. Soc. A*, 223(1155):446–468, 1954.

[50] R. Aris. On the dispersion of a solute in a fluid flowing through a tube. *Proc. R. Soc. A*, 235(1200):67–77, 1956.

[51] ME Young, PA Carroad, and RL Bell. Estimation of diffusion coefficients of proteins. *Biotechnology and Bioengineering*, 22(5):947–955, 1980.

[52] Onofrio Annunziata, Daniela Buzatu, and John G Albright. Protein diffusion coefficients determined by macroscopic-gradient Rayleigh interferometry and dynamic light scattering. *Langmuir : the ACS journal of surfaces and colloids*, 21(26):12085–9, December 2005.

[53] Shenggen Yao, Daniel K. Weber, Frances Separovic, and David W. Keizer. Measuring translational diffusion coefficients of peptides and proteins by PFG-NMR using band-selective RF pulses. *European Biophysics Journal*, 43:331–339, 2014.

[54] Patrick Masson and Jacques Anguille. Determination of the free electrophoretic mobility of proteins by poly-acrylamide gradient gel electrophoresis: A new approach. *Journal of chromatography*, 192:402–407, 1980.

[55] BJ Berne and Rina Giniger. Electrophoretic light scattering as a probe of reaction kinetics. *Biopolymers*, 12(5):1161–1169, 1973.

[56] Funda Tihminlioglu, Rahul K. Surana, Ronald P. Danner, and J. L. Duda. Finite concentration inverse gas chromatography: Diffusion and partition measurements. *Journal of Polymer Science Part B: Polymer Physics*, 35(8):1279–1290, 1997.

[57] Pim G Muijselaar, Marion A van Straten, Henk A Claessens, and Carel A Cramers. Determination of diffusion coefficients and separation numbers in micellar electrokinetic chromatography. *Journal of Chromatography A*, 766(1-2):187–195, April 1997.

[58] K.A. Rezaei and F. Temelli. Using supercritical fluid chromatography to determine diffusion coefficients of lipids in supercritical CO2. *The Journal of Supercritical Fluids*, 17(1):35–44, February 2000.

[59] C. R. Wilke and Pin Chang. Correlation of diffusion coefficients in dilute solutions. *AIChE Journal*, 1(2):264–270, June 1955.

[60] D. C. Harris. *Quantitative Chemical Analysis*. W.H. Freeman: New York, 1999.

[61] J. C. Sternberg. *Advances in Chromatography*, volume 2. Giddings, J. C., Keller, R. A., Eds.; Marcel Dekker: New York, 2006.

[62] Kathryn R Williams, Bhavin Adhyaru, Igor German, and Thomas Russell. Determination of a Diffusion Coefficient by Capillary Electrophoresis. An Experiment for the Physical and Biophysical Chemistry Laboratories. *Journal of Chemical Education*, 79(12):1475, 2002.

[63] Christopher T Culbertson, Stephen C Jacobson, and J Michael Ramsey. Diffusion coefficient measurements in microfluidic devices. *Talanta*, 56(2):365–73, 2002.

[64] Yvonne Walbroehl and James W. Jorgenson. Capillary zone electrophoresis for the determination of electrophoretic mobilities and diffusion coefficients of proteins. *J. Microcolumn Sep.*, 1(1):41–45, 1989.

[65] Y.J. Yao and S.F.Y. Li. Determination of diffusion coefficients by capillary zone electrophoresis. *Journal of Chromatographic Science*, 32(4):117–120, 1994.

[66] Michael U. Musheev, Sahar Javaherian, Victor Okhonin, and Sergey N. Krylov. Diffusion as a tool of measuring temperature inside a capillary. *Analytical Chemistry*, 80(17):6752–6757, 2008.

[67] C.T. Culbertson. *Ph.D. Dissertation thesis*. University of North Carolina, Chapel Hill, 1996.

[68] Carlo S Effenhauser and Gerard J M Bruin. Review Integrated chip-based capillary electrophoresis. *Electrophoresis*, 18:2203–2213, 1997.

[69] Seyed Mostafa Shameli, Caglar Elbuken, Junjie Ou, Carolyn L Ren, and Janusz Pawliszyn. Fully integrated PDMS/SU-8/quartz microfluidic chip with a novel macroporous poly dimethylsiloxane (PDMS) membrane for isoelectric focusing of proteins using whole-channel imaging detection. *Electrophoresis*, 32(3-4):333–9, February 2011.

[70] Vladislav Dolník. Capillary electrophoresis on microchip CE and CEC. *Electrophoresis*, 21:41–54, 2000.

[71] Xing-Zheng Wu and Janusz Pawliszyn. Whole-column imaging capillary electrophoresis of proteins with a short capillary. *Electrophoresis*, 23(4):542–9, February 2002.

[72] X Z Wu, S K Sze, and J Pawliszyn. Miniaturization of capillary isoelectric focusing. *Electrophoresis*, 22(18):3968–3971, 2001.

[73] František Opekar and Karel Stulík. Some important combinations of detection techniques for electrophoresis in capillaries and on chips with emphasis on electrochemical principles. *Electrophoresis*, 32(8):795–810, April 2011.

[74] Woei Tan, Z Hugh Fan, Charmaine X Qiu, Antonio J Ricco, and Ian Gibbons. Miniaturized capillary isoelectric focusing in plastic microfluidic devices. *Electrophoresis*, 23(20):3638–45, October 2002.

[75] Alexander Muck and Ales Svatos. Chemical modification of polymeric microchip devices. *Talanta*, 74(3):333–41, December 2007.

[76] Detlev Belder and Martin Ludwig. Surface modification in microchip electrophoresis. *Electrophoresis*, 24(21):3595–606, November 2003.

[77] Vladislav Dolník. Wall coating for capillary electrophoresis on microchips. *Electrophoresis*, 25(21-22):3589–601, November 2004.

[78] Wen Jiang, Justina Ngum Awasum, and Knut Irgum. Control of electroosmotic flow and wall interactions in capillary electrophoresis capillaries by photografted zwitterionic polymer surface layers. *Analytical chemistry*, 75(11):2768–74, June 2003.

[79] Vladislav Dolník. Capillary electrophoresis of proteins 2003-2005. *Electrophoresis*, 27(1):126–41, January 2006.

[80] Colin D Costin, Roy K Olund, Bethany a Staggemeier, Ana Kristine Torgerson, and Robert E Synovec. Diffusion coefficient measurement in a microfluidic analyzer using dual-beam microscale-refractive index gradient detection. Application to on-chip molecular size determination. *Journal of chromatography. A*, 1013(1-2):77–91, September 2003.

[81] Hongling Han, Eliza Livingston, and Xiaoyu Chen. High throughput profiling of charge heterogeneity in antibodies by microchip electrophoresis. *Analytical chemistry*, 83(21):8184–91, 2011.

[82] Attila Felinger, Tamás L. Pap, and János Inczédy. Improvement of the signal-to-noise ratio of chromatographic peaks by Fourier transform. *Analytica Chimica Acta*, 248(2):441–446, August 1991.

[83] T T Tsay and K. A. Jacobson. Spatial Fourier analysis of video photobleaching measurements. Principles and optimization. *Biophys. J.*, 60(2):360–8, 1991.

[84] D. A. Berk, F Yuan, M Leunig, and R K Jain. Fluorescence photobleaching with spatial Fourier analysis: measurement of diffusion in light-scattering media. *Biophys. J.*, 65(6):2428–36, 1993.

[85] C Gosse, T Le Saux, J Allemand, V Croquette, and H Berthoumieux. Fourier Analysis To Measure Diffusion Coefficients and Resolve Mixtures on a Continuous Electrophoresis Chip. *Anal. Chem.*, 79(21):8222–31, 2007.

[86] a. M. Bianchi, L. T. Mainardi, and S. Cerutti. Time-frequency analysis of biomedical signals. *Transactions of the Institute of Measurement and Control*, 22(3):215–230, 2000.

[87] Atefeh S. Zarabadi and Janusz Pawliszyn. Accurate Determination of the Diffusion Coefficient of Proteins by Fourier Analysis with Whole Column Imaging Detection. *Analytical Chemistry*, 87:2100–2106, 2015.

[88] R.W. Ramirez. *The FFT Fundamentals and Concepts*. prentic-Hall, INC. Englewood Cliffs, N. J., 1985.

[89] James W. Cooley, Peter a. W. Lewis, and Peter D. Welch. The Fast Fourier Transform and Its Applications. *IEEE Transactions on Education*, 12(1):27–34, 1969.

[90] Naol Tufa Negero. Fourier Transform Methods for Partial Differential Equations. *International Journal of Partial Differential Equations and Applications*, 2(3):44–57, 2014.

[91] Yuri Kalambet, Yuri Kozmin, Ksenia Mikhailova, Igor Nagaev, and Pavel Tikhonov. Reconstruction of chromatographic peaks using the exponentially modified Gaussian function. *Journal of Chemometrics*, 25(7):352–356, July 2011.

[92] Kevin Lan and James W Jorgenson. A hybrid of exponential and gaussian functions as a simple model of asymmetric chromatographic peaks. *Journal of chromatography. A*, 915(1-2):1–13, 2001.

[93] Maria C. Garca-Alvarez-Coque, Ernesto F. Sim-Alfonso, Jos M. Sanchis-Mallols, and Juan J. Baeza-Baeza. A new mathematical function for describing electrophoretic peaks. *Electrophoresis*, 26(11):2076–2085, 2005.

[94] Robert Stewart, Iftah Gideoni, and Yonggang Zhu. Signal Processing Methods for Capillary Electrophoresis. *Signal Processing Methods for Capillary Electrophoresis*, 2008.

[95] B Gas, M Stedry, a Rizzi, and E Kenndler. Dynamics of peak dispersion in capillary zone electrophoresis including wall adsorption I. Theoretical model and results of simulation. *Electrophoresis*, 16(6):958–67, 1995.

[96] Bi-Feng Liu, Yoichi Sera, Norio Matsubara, Koji Otsuka, and Shigeru Terabe. Signal denoising and baseline correction by discrete wavelet transform for microchip capillary electrophoresis. *Electrophoresis*, 24(18):3260–5, 2003.

[97] Weisstein, Eric W. "Fourier Transform–Gaussian." From MathWorld–A Wolfram Web Resource. http://mathworld.wolfram.com/FourierTransformGaussian.html.

[98] Petr Gebauer and Petr Boc. Predicting Peak Symmetry in Capillary Zone Electrophoresis : The Concept of the Peak Shape Diagram. *Anal. Chem.*, I(8):3246–52, 1998.

[99] Zs Pápai and T L Pap. Analysis of peak asymmetry in chromatography. *Journal of chromatography. A*, 953(1-2):31–8, April 2002.

[100] Min Zou, YanLi Han, Li Qi, and Yi Chen. Fast and accurate measurement of diffusion coefficient by Taylors dispersion analysis. *Chin. Sci. Bull.*, 52(24):3325–32, 2007.

[101] L.C. Andrews. *Special Functions of Mathematics for Engineers*. Oxford science publications. SPIE Optical Engineering Press, 1992.

[102] Mark S. Jeansonne and Joe P. Foley. Improved equations for the calculation of chromatographic figures of merit for ideal and skewed chromatographic peaks. *Journal of Chromatography A*, 594(1-2):1–8, March 1992.

[103] Mark S. Jeansonne and Joe P. Foley. Measurement of Statical Moments of Resolved and Overlapping Chromatographic peaks. *Journal of chromatography*, 461:149–163, 1989.

[104] A Felinger, T Pap, and J Inczédy. Curve fitting to asymmetrical chromatograms by the extended Kalman filter in frequency domain. *Talanta*, 41(7):1119–26, 1994.

[105] Weisstein, Eric W. "Boxcar Function." From MathWorld–A Wolfram Web Resource. http://mathworld.wolfram.com/RectangleFunction.html.

[106] Fengbin Ye, Henrik Jensen, Susan W Larsen, Anan Yaghmur, Claus Larsen, and Jesper Ø stergaard. Measurement of drug diffusivities in pharmaceutical solvents using Taylor dispersion analysis. *J. Pharm. Biomed. Anal.*, 61:176–83, 2012.

[107] Christine Marie Thetford. *Ph.D. Thesis*. University of North Carolina, 2003.

[108] M S Bello, R Rezzonico, and P G Righetti. Use of taylor-aris dispersion for measurement of a solute diffusion coefficient in thin capillaries. *Science (N.Y.)*, 266(5186):773–6, 1994.

[109] Wenrui Jin and Haifeng Chen. A New Method of Determination of Diffusion Coefficients Using Capillary Zone Electrophoresis (Peak-Height Method). *Chromatographia*, 52(1-2):17–21, 2000.

[110] Upma Sharma, Nathaniel J Gleason, and Jeffrey D Carbeck. Diffusivity of Solutes Measured in Glass Capillaries Using Taylor s Analysis of Dispersion and a Commercial CE Instrument. *Anal. Chem.*, 77(3):806–813, 2005.

[111] Joseph Chamieh, Farid Oukacine, and Hervé Cottet. Taylor dispersion analysis with two detection points on a commercial capillary electrophoresis apparatus. *J. Chromatogr. A*, 1235:174–7, 2012.

[112] Pier Giorgio Righetti. Determination of the isoelectric point of proteins by capillary isoelectric focusing. *J. Chromatogr. A*, 1037(1-2):491–499, 2004.

[113] Bingcheng Yang, Feifang Zhang, Hongzhe Tian, and Yafeng Guan. On-line preconcentration of protein in capillary electrophoresis with an end-column cellulose acetate-based porous membrane. *J. Chromatogr. A*, 1117(2):214–8, 2006.

[114] Damon M Osbourn, David J Weiss, and Craig E Lunte. On-line preconcentration methods for capillary electrophoresis. *Electrophoresis*, 21(14):2768–2779, 2008.

[115] Braden C Giordano, Dean S Burgi, Sean J Hart, and Alex Terray. On-line sample pre-concentration in microfluidic devices: a review. *Anal. Chim. Acta*, 718:11–24, 2012.

[116] J. Behlke and O. Ristau. Soc. *Biochem. Soc. Trans.*, 26:758–61, 1998.

[117] B Chu, A Yeh, F C Chen, and B Weiner. Self-Association of 0-Lactoglobulin A in Acid Solution . I . Translational Diffusion Coefficients Preparation of Protein Solutions. *Biopolymers*, 14:93–109, 1975.

[118] B. Chen, C. Andreas, and R. David. Continuous Optical Scanning in Polyacrylamide Gel Electrophoresis: Estimation of the Apparent Diffusion Coefficient of b-Lactoglobulin. *Anal. Biochem.*, 130:120–130, 1979.

[119] M. H. Smith. *Handbook of Biochemistry.* Sober,H. A., Ed, Chemical Rubber Company, Cleveland, 2nd edition, 1970.

[120] Zoran Sosic, Damian Houde, Andy Blum, Tyler Carlage, and Yelena Lyubarskaya. Application of imaging capillary IEF for characterization and quantitative analysis of recombinant protein charge heterogeneity. *Electrophoresis*, 29(21):4368–76, November 2008.

[121] Suhua Yang, Yiming Zhang, Tao Liao, Zhenpeng Guo, and Yi Chen. Electromigration diffusivity spectrometry: a way for simultaneous determination of diffusion coefficients from mixed samples. *Electrophoresis*, 31(17):2949–56, 2010.

[122] Pinaki R Majhi, Reddy R Ganta, Ram P Vanam, Emek Seyrek, Katie Giger, and Paul L Dubin. Electrostatically Driven Protein Aggregation: b-Lactoglobulin at Low Ionic Strength. *Langmuir : the ACS journal of surfaces and colloids*, 22(6):9150–9159, 2006.

[123] G. S. Settles. Schlieren and Shadowgraph Techniques. In *Schlieren and Shadowgraph Techniques*, chapter 1 Historical Background. Springer-Verlag Berlin Heidelberg, January 2001.

[124] G. S. Settles. Schlieren and Shadowgraph Techniques. In *Schlieren and Shadowgraph Techniques: Visualizing Phenomena in Transparent Media.*, chapter 4. Springer-Verlag Berlin Heidelberg, 2001.

[125] Jiaqi Wu, Janusz Pawliszyn, and Publisher Taylor. Capillary Isoelectric Focusing with Imaging Detection. *Journal of Liquid Chromatography*, 16(9-10):1891–1902, July 1993.

[126] Amrita Mazumdar. Principles And Techniques of Schlieren Imaging. Technical report, Columbia University Computer Science Technical Reports, New York, NY, 2013.

[127] Alfred Vogel, Ingo Apitz, Sebastian Freidank, and Rory Dijkink. Sensitive high-resolution white-light Schlieren technique with a large dynamic range for the investigation of ablation dynamics. *Optics letters*, 31(12):1812–1814, 2006.

[128] Zhen Liu, Junjie Ou, Razim Samy, Tomasz Glawdel, Tiemin Huang, Carolyn L Ren, and Janusz Pawliszyn. Side-by-side comparison of disposable microchips with commercial capillary cartridges for application in capillary isoelectric focusing with whole column imaging detection. *Lab on a chip*, 8(10):1738–41, October 2008.

[129] CCD Sensor Architectures. http://www.andor.com/learning-academy.

[130] Chihyung Huang, James W Gregory, and John P Sullivan. A modified schlieren technique for micro flow visualization. *Measurement Science and Technology*, 18(5):N32, 2007.

[131] Janusz Pawliszyn. Nanoliter Volume Sequential Differential Concentration Gradient Detector. *Analytical Chemistry*, 2801(12):2796–2801, 1988.

[132] Janusz Pawliszyn. Detection of Flowing Samples with a Selective Concentration. *Anal. Chem.*, 60:766–773, 1988.

[133] Q Mao and J Pawliszyn. Capillary isoelectric focusing with whole column imaging detection for analysis of proteins and peptides. *Journal of biochemical and biophysical methods*, 39(1-2):93–110, February 1999.

[134] H. Rilbe. Historical and theoretical aspects of isoelectric focusing. *N.Y. Acad. Sci.*, 209:11–22, 1973.

[135] Takao. Tsuda, Jonathan V. Sweedler, and Richard N. Zare. Rectangular capillaries for capillary zone electrophoresis. *Analytical Chemistry*, 62(19):2149–2152, October 1990.

[136] H. Lv, W. Yan, X. Yang, J. Li, and J. Zhu. Signal Detection of Multi-Channel Capillary Electrophoresis Chip Based on CCD. *Measurement Science Review*, 12(6):272–276, 2012.

[137] Oluwatosin O Dada, Lauren M Ramsay, Jane a Dickerson, Nathan Cermak, Rong Jiang, Cuiru Zhu, and Norman J Dovichi. Capillary array isoelectric focusing with laser-induced fluorescence detection: milli-pH unit resolution and yoctomole mass detection limits in a 32-channel system. *Analytical and bioanalytical chemistry*, 397(8):3305–10, August 2010.

[138] Imran Ali, Hassan Y. AboulEnein, and V. K. Gupta. Precision in Capillary Electrophoresis. *Analytical Letters*, 39(11):2345–2357, August 2006.

[139] a E Kamholz, E a Schilling, and P Yager. Optical measurement of transverse molecular diffusion in a microchannel. *Biophysical journal*, 80(April):1967–1972, 2001.

[140] Andrew Evan Kamholz, Bernhard H. Weigl, Bruce A. Finlayson, and Paul Yager. Quantitative analysis of molecular interaction in a microfluidic channel: The T-sensor. *Analytical Chemistry*, 71(23):5340–5347, 1999.